

CZECH TECHNICAL UNIVERSITY IN PRAGUE
Faculty of Nuclear Sciences and Physical Engineering

DISSERTATION THESIS
Heavy quarks in proton

Bibliografický záznam

Autor	Ing. Michal Svatoš, České vysoké učení technické v Praze, Fakulta jaderná a fyzikálně inženýrská, Katedra fyziky
Název práce	Těžké kvarky v protonu
Studijní program	Aplikace přírodních věd
Studijní obor	Jaderné inženýrství
Školitel	RNDr. Pavel Staroba, CSc., Fyzikální ústav AV ČR, v. v. i.,
Akademický rok	2014/2015
Počet stran	101
Klíčová slova	foton, b jet, účinný průřez

Bibliographic Entry

Author	Ing. Michal Svatoš, Czech Technical University in Prague, Faculty of Nuclear Sciences and Physical Engineering, Department of physics
Title of Dissertation	Heavy quarks in proton
Degree Programme	Applications of Natural Sciences
Field of Study	Nuclear engineering
Supervisor	RNDr. Pavel Staroba, CSc., Institute of Physics of the Academy of Sciences of the Czech Republic, Prague, v.v.i.
Academic Year	2014/2015
Number of Pages	101
Keywords	photon, b jet, cross-section

Abstrakt

Měření fotonů vznikajících současně s kvarkem b v proton-protonových interakcích nám může poskytnout přesnější informaci o vnitřní struktuře protonu. Je tomu tak proto, že přesnost určení partonových distribučních funkcí b kvarku a gluonu může být takovým měřením zvýšena.

V práci je prezentováno měření účinného průřezu fotonů vznikajících současně s b kvarkem (proces $pp \rightarrow \gamma + b + X$) při $\sqrt{s} = 8$ TeV v experimentu ATLAS. Byl použit celý soubor dat získaný detektorem ATLAS v roce 2012 při energii 8 TeV. Odpovídající integrovaná luminosita je 20.3 fb^{-1} . Z dat byl získán diferenciální účinný průřez jako funkce příčné hybnosti fotonu a srovnán s předpovědí generátoru PYTHIA 8 v nejnižším řádu poruchové teorie. Účinný průřez získaný z dat byl normalizován pomocí změřené integrované luminosity, tedy nezávisle na předpovědi generátoru. Hodnoty rozdělení pro data leží nad hodnotami předpovězenými generátorem. Pravděpodobnou příčinou rozdílu je přítomnost efektů vyšších řádů poruchové teorie, které nejsou zahrnuty v použitém generátoru. Hodnoty integrovaného účinného průřezu jsou $(750 \pm 24(\text{stat}))$ pb pro data a $(668 \pm 10(\text{stat}))$ pb pro Monte Carlo. Dosud byla zahrnuta pouze statistická chyba. Fázový prostor měření je: $p_T^\gamma \in \langle 25, 1000 \rangle$ GeV, $|\eta^\gamma| < 1.37$ nebo $1.56 < |\eta^\gamma| < 2.37$, $p_T^{\text{jet}} > 20$ GeV, $|\eta^{\text{jet}}| < 2.4$, $\Delta R(\gamma - \text{jet}) > 1$. Získané výsledky byly srovnány s výsledky experimentů zkoumajících stejný nebo podobné procesy.

Abstract

The measurement of prompt photon associated with a b jet in proton-proton interactions can provide us insight into the inner structure of proton. This is because precision of determination of parton distribution functions of b quark and gluon can be increased by such a measurement.

The measurement of cross-section of prompt photon associated with a b jet (process $pp \rightarrow \gamma + b + X$) at $\sqrt{s} = 8$ TeV with the ATLAS detector is presented. Full 8 TeV dataset collected by ATLAS during the year 2012 was used in this analysis. Corresponding integrated luminosity is 20.3 fb^{-1} . Fiducial differential cross-section as a function of photon transverse momentum at particle level was extracted from data and compared with the prediction of leading order event generator PYTHIA 8. Cross-section extracted from data is normalised independently on the Monte Carlo prediction. Values of data distribution lie above Monte Carlo values. The difference can be explained by presence of higher order effects not included in the leading order event generator. The resulting integrated fiducial cross section is $(750 \pm 24(\text{stat}))$ pb for data and $(668 \pm 10(\text{stat}))$ pb for Monte Carlo. Statistical uncertainties only are taken into account. Fiducial region of the measurement is: $p_T^\gamma \in \langle 25, 1000 \rangle$ GeV, $|\eta^\gamma| < 1.37$ or $1.56 < |\eta^\gamma| < 2.37$, $p_T^{\text{jet}} > 20$ GeV, $|\eta^{\text{jet}}| < 2.4$, and $\Delta R(\gamma - \text{jet}) > 1$. This measurement is compared with results of previous experiments measuring the same or similar processes.

Contents

1	Introduction	13
1.1	The Standard Model	14
1.1.1	The fundamental fermions	14
1.1.2	The fundamental interactions	14
1.2	Quantum Chromodynamics	15
1.3	The parton model	16
1.3.1	The parton distribution functions	17
1.4	Prompt photon and b jet processes	19
1.4.1	Previous results	20
2	The LHC	28
2.1	History	28
2.2	Basic characteristics	29
3	The ATLAS experiment	30
3.1	The Inner Detector	30
3.2	Calorimeters	31
3.3	The Muon Spectrometer	33
3.4	Magnets	35
3.5	Forward detectors	35
3.6	Trigger and data acquisition	36
3.7	ATLAS Distributed Computing	37
4	Properties of basic objects	39
4.1	Photon	39
4.1.1	Photon trigger	39
4.1.2	Photon reconstruction	39
4.1.3	Photon calibration	39
4.1.4	Cuts for photon identification	40
4.1.5	Photon isolation	41
4.2	Jet	41
4.2.1	anti- k_t clustering algorithm	41
4.2.2	Jet calibration	42
4.2.3	Jet background	42
4.2.4	Removal of non-collision background	43
4.2.5	Jet quality selection	43
4.3	b-tagging in the ATLAS experiment	44
4.3.1	Introduction	44
4.3.2	Reconstruction of the key objects	45
4.3.3	b-tagging algorithms	46
4.3.4	MultiVariate tagging algorithm	47
5	Data and MC samples	49
5.1	Data samples	49
5.2	Monte Carlo generator level samples	49
5.3	Monte Carlo reconstruction level samples	51

6	Cross-section measurement	53
6.1	Monte Carlo	53
6.2	Data	53
6.3	Binning	53
7	Analysis of events at the generator level	54
7.1	PYTHIA 8 processes	54
7.1.1	$Qg \rightarrow \gamma Q$	56
7.1.2	$q\bar{q} \rightarrow \gamma g, g \rightarrow Q\bar{Q}$	56
7.1.3	$qq, gg \rightarrow Qq, q \rightarrow \gamma + X$	56
7.1.4	$qg \rightarrow qg, q \rightarrow \gamma + X, g \rightarrow Q\bar{Q}$	56
8	The event selection	62
8.1	Good Run List	62
8.2	Incomplete events	62
8.3	LAr calorimeter noise bursts and data integrity errors	62
8.4	Tile calorimeter event corruption	62
8.5	Tile calorimeter trips	62
8.6	Primary vertex	63
8.7	Jet acceptance	63
8.8	Jet cleaning	63
8.9	Jet hot cell cleaning	63
8.10	Jet BCH cleaning	63
8.11	Photon trigger	63
8.11.1	Trigger matching	64
8.11.2	Trigger prescales	64
8.12	Photon acceptance	64
8.13	Photon object quality	64
8.14	Photon cleaning	64
8.15	Ambiguity resolver	65
8.16	Jet b-tagging	65
8.17	Distance of photon and jet	65
8.18	Duplicate events	65
8.19	The event selection overview	67
8.20	Pile-up reweighting	67
9	Background subtraction	70
9.1	Photon isolation	70
9.2	Two-dimensional sideband method	71
9.2.1	Derivation of the method	71
9.2.2	Results	76
9.3	Template fitting	78
10	Results of the measurement	83
11	Summary and Conclusions	85
	Appendices	86

A	Data and MC samples details	87
A.1	Data samples	87
A.2	Monte Carlo generator level samples	87
A.3	Monte Carlo reconstruction level samples	88
B	$\gamma + c$ events at $\sqrt{s}=8$ TeV at generator level	89
B.1	PYTHIA 8 processes	89
B.1.1	$Qg \rightarrow \gamma Q$	89
B.1.2	$q\bar{q} \rightarrow \gamma g, g \rightarrow Q\bar{Q}$	89
B.1.3	$qq, gg \rightarrow Qq, q \rightarrow \gamma + X$	91
B.1.4	$qg \rightarrow qg, q \rightarrow \gamma + X, g \rightarrow Q\bar{Q}$	91
C	Previous reports	97
C.1	About the analysis	97
C.1.1	Talks	97
C.1.2	Working groups meetings	97
C.2	General	97
	References	98

List of Tables

1	The fundamental fermions	14
2	The fundamental interactions ($Mc^2 = 1 \text{ GeV}$)	15
3	Major cooling systems operating in the ATLAS	30
4	Number of readout channels in the ATLAS subdetectors	35
5	Transverse momentum range of photon used for analysis for particular Monte Carlo generator level sample	50
6	Transverse momentum range of photon used for analysis for particular Monte Carlo reconstruction level sample	52
7	PDG IDs of relevant particles	54
8	Single photon trigger chains	63
9	MV1 algorithm operating points	65
10	Number of b, c, and light jets in Monte Carlo samples for each MV1 efficiency	65
11	Number of events per event selection level	67

List of Figures

1	Diagrammatic structure of a generic hard scattering process [11]	16
2	Feynman diagrams for Compton-QCD	17
3	Feynman diagrams for quark-antiquark annihilation	17
4	PDFs and their error bands (c and b quarks and gluon)	18
5	Feynman diagrams for fragmentation photon created with quark-antiquark pair	19
6	Feynman diagrams for fragmentation photon created with single quark	20
7	NNPDF 2.1 uncertainties without and with addition of photon+jet data. Result of analysis of ATLAS data	21
8	NNPDF 2.1 uncertainties without and with addition of photon+jet data. Result of analysis of toy Monte Carlo samples	21
9	Cross-section measurement at CDF	22
10	Cross-section measurement at D0	23
11	Measured and expected inclusive isolated prompt photon cross-section as a function of transverse energy of the photon at the ATLAS experiment	24
12	Measured differential cross-section $d\sigma/dp_T^{\text{b-jet}}$ using 4.8 pb^{-1} of data at the ATLAS experiment	25
13	Differential b-jet cross-section using 34 pb^{-1} of data at the ATLAS experiment	26
14	Measured cross-section for isolated-photon plus jet at the ATLAS experiment.	27
15	CERN and LHC	28
16	Cut-away view of the ATLAS detector	31
17	Cut-away view of the Inner Detector	32
18	Cut-away view of calorimeter system	33
19	Cut-away view of the muon spectrometer	34
20	Location of forward detectors with respect to the interaction point (IP)	36
21	The meaning of the transverse and the longitudinal impact parameter	44
22	Light jet rejection efficiency as a function of b-tagging efficiency	48
23	Delivered and recorded luminosity [43]	49
24	Stitching of Monte Carlo generator level samples	50
25	Stitching of Monte Carlo reconstructed level samples	51
26	Cross-section of Compton-QCD for b flavoured quarks	54
27	Cross-section of quark-antiquark annihilation for b flavoured quarks	55
28	Cross-section of event where fragmentation photon is created with b flavoured quark	55
29	Cross-section of event where fragmentation photon is created with $b\bar{b}$ pair	56
30	Combined cross-section of direct and fragmentation processes	57
31	Event structure of the Compton-QCD	58
32	Event structure of the quark-antiquark annihilation	59
33	Event structure of event where fragmentation photon is created with b flavoured quark	60
34	Event structure of event where fragmentation photon is created with $b\bar{b}$ pair	61
35	Isolation efficiency as a function of distance of leading photon and leading jet for three isolation energies - 3,5, and 7 GeV	66
36	Comparison of p_T^γ distribution in data and Monte Carlo after event selection.	66
37	p_T^γ distribution in data and Monte Carlo after event selection with statistical uncertainty distributions	68
38	NPV distribution in data and Monte Carlo before and after pile-up reweighting	68
39	Isolation efficiency for energies 3, 5, and 7 GeV	70
40	Isolation efficiency for p_T^γ -dependent isolation	71
41	Illustration of 2D sideband method	72

42	Distribution of p_T^γ in regions A, B, C, and D in data	73
43	Distribution of p_T^γ of reconstructed photons in regions A, B, C, and D in Monte Carlo . .	74
44	Distribution of p_T^γ of truth photons in regions B, C, and D in Monte Carlo	75
45	Distribution of 2D sideband method correction factors	76
46	Distribution of p_T^γ in data and Monte Carlo after 2D sideband method	77
47	Search for useful variables for template fitting in MV1 and JetFitterCombNN	78
48	Fraction of b jets and c+light jets obtained by template fitting	79
49	The p_T^γ distribution after background subtraction	79
50	Distributions of $\log(pb^2/(pc \times pu))$ in data and in Monte Carlo	81
51	Distributions of $\log(pb^2/(pc \times pu))$ in data and in Monte Carlo	82
52	Cross-section correction factor	83
53	Comparison of final cross-section in data and cross-section extracted from generation level samples	84
54	Cross-section of Compton-QCD for c flavoured quarks	89
55	Cross-section of quark-antiquark annihilation for c flavoured quarks	90
56	Cross-section of event where fragmentation photon is created with c flavoured quark . .	90
57	Cross-section of event where fragmentation photon is created with $c\bar{c}$ pair	91
58	Combined cross-section of direct and fragmentation processes	92
59	Event structure of the Compton-QCD	93
60	Event structure of the quark-antiquark annihilation	94
61	Event structure of event where fragmentation photon is created with c flavoured quark . .	95
62	Event structure of event where fragmentation photon is created with $c\bar{c}$ pair	96

I declare hereby that this thesis was written by myself solely and I have cited all the used sources.

Prague, 2015

Michal Svatoš

Acknowledgements

Here, I would like to express my gratitude to all who helped and supported me during my work on this thesis, especially Pavel Staroba and Josu Cantero Garcia for their valuable advices.

1 Introduction

The parton distribution functions can provide us insight into the inner structure of proton. Precision of parton distribution function determination can be increased using a suitable measurement. For b quark and gluon parton distribution functions, it is measurement of prompt photon associated with a b jet.

In general, uncertainties of parton distribution functions have impact on precision of measurement for many important Standard Model processes [1]. First example can be production of W^\pm and Z^0 in quark-antiquark interactions. The parton distribution function uncertainty does not come from light quarks (as they are constrained by DIS and Drell-Yan data) but from heavy quark (s, c, b) interactions. Another example is top quark pair production. At leading order, $t\bar{t}$ pairs are produced via quark-antiquark and gluon-gluon interactions. Measurement of $t\bar{t}$ rates can provide constraints on gluon and heavy flavour parton distribution functions if associated theoretical and experimental uncertainties are each reduced below 3-5 %.

In the Higgs boson searches [2], there are four main mechanisms: associated production with W/Z ($q\bar{q} \rightarrow VH$), massive vector boson fusion ($qq \rightarrow Hqq$), the gluon-gluon fusion mechanism ($gg \rightarrow H$), and associated production with top quarks ($gg, q\bar{q} \rightarrow t\bar{t}H$). The uncertainties caused by the parton distribution functions are usually $\mathcal{O}(5\%)$ but for the gluon-gluon fusion process for large enough Higgs boson masses it can reach the level of 10 %. This is valid within given PDF set. Difference between cross-section evaluated using different PDF sets can be larger. For example, normalizing to the values obtained with the CTEQ6M set, for instance, the cross sections can be different by up to 15 % for the four production mechanisms. There is also interesting phenomenon related to structure of proton - intrinsic heavy flavours in proton. This phenomenon can also contribute to the Higgs boson production via inclusive production ($pp \rightarrow HX$), semidiffractive production ($pp \rightarrow HpX$), and exclusive diffractive production ($pp \rightarrow pHp$) [3]. In the intrinsic heavy flavour model, the parton distribution functions $f_a(x, \mu)$ are describing proton's quark and gluon content at scale μ . When μ is small (it corresponds to long distance scales), the parton distribution functions express nonperturbative physics. In practice, the parton distribution functions are parametrized at a scale μ_0 which is large enough to allow perturbative calculation for $\mu > \mu_0$. The unknown functions $f_a(x, \mu)$ are then determined empirically in QCD global fit. In global analyses, it is assumed that charm content of proton is negligible at $\mu \sim m_c$ and bottom content is negligible at $\mu \sim m_b$. It means that heavy flavour components arise only perturbatively through gluon splitting. But there is also possibility to expect nonperturbative "intrinsic" heavy quark component in proton [4]. Data from the SELEX experiment (Fermilab) [5] are providing strong support for the presence of intrinsic charm in hadrons in amount less than 1 %.

Uncertainties of heavy quarks and gluon parton distribution functions can also affect beyond Standard Model processes [1]. There are several examples of MSSM processes which strongly depend on them - production of Higgs boson via bottom quark annihilation ($b\bar{b} \rightarrow h$ where $h = h^0, H^0, A^0$), charged Higgs boson production via s,c,b interactions ($c\bar{s} + c\bar{b} \rightarrow h^\pm$), or associated production of CP-odd (A) and charged Higgs bosons ($q\bar{q}' \rightarrow W \rightarrow Ah^\pm$). Supersymmetric neutral Higgs production is sensitive mostly to b quark and gluon parton distribution function, while charged Higgs production probes combination of s, c, and b quark parton distribution functions.

This thesis describes my contribution to the measurement of cross-section of processes with prompt photon and b jet at $\sqrt{s} = 8$ TeV at the ATLAS experiment. The thesis is arranged as follows. This section outlines physics motivation and context of the cross-section measurement. Basic overview of structure of the LHC accelerator and the ATLAS experiment is provided in Sections 2 and 3, respectively. Section 4 provides information about basic objects of this thesis - photon and jet (normal jets as well as b tagged jets). Section 5 gives overview of data used for the analysis (with some more details in Appendix A). Section 6 contains formulas and binning used to get cross-section distributions. Section 7 summarizes results of analysis of generator level events for $\gamma + b$ processes (and Appendix B shows results of identical

analysis for $\gamma + c$ events). Section 8 describes details of event selection. Section 9 describes subtraction of background from selected events. Section 10 contains resulting cross-section measured in data and its comparison with Monte Carlo predictions. And finally, Section 11 gives summary of results and conclusions.

The analysis was performed using ROOT [6][7], versions 5.34/14 and 5.34/15.

1.1 The Standard Model

The Standard Model [8],[9] provides compact and successful description of the properties of its fundamental constituents (see Section 1.1.1) and their interactions (see Section 1.1.2). It contains 17 arbitrary parameters (masses, mixing angles, coupling constants, etc.)

1.1.1 The fundamental fermions

In the Standard Model, matter is build from spin $1/2$ particles, fermions - six quarks and six leptons (see Table 1) and their antiparticles.

	Flavour			Charge
leptons	e (electron)	μ (muon)	τ (tau lepton)	-1
	ν_e (electron neutrino)	ν_μ (muon neutrino)	ν_τ (tau neutrino)	0
quarks	u(up)	c(charm)	t(top)	+2/3
	d(down)	s(strange)	b(bottom)	-1/3

Table 1: The fundamental fermions

The leptons carry integral electric charge. Each flavour of lepton has one charged lepton and neutrino associated to it. Muon and tau lepton are both unstable and decay spontaneously to electron, neutrinos, and other particles. Leptons exist as free particles. In the Standard Model, neutrinos are considered massless even though there are evidences that they have finite mass.

The quarks carry fractional electric charge. They are grouped into pairs differing by one unit of electric charge. Quarks do not exist as free particles. They can be found only in combinations because of quark confinement.

For consistency of the Standard model, the Higgs boson (explaining why some fundamental particles have mass) is necessary. It was discovered recently [10].

1.1.2 The fundamental interactions

The particles can interact in several different ways. The interactions are described in terms of the exchange of bosons (see Table 2) between fermion constituents.

Electromagnetic interaction affects extra-nuclear physics. It is responsible, for example, for bound states of electron with nuclei (atoms and molecules). It is mediated by photon.

Strong interaction is responsible for binding quarks in the neutron and proton and for binding neutrons and protons within nuclei. It is mediated by gluon. In the theory of strong interaction, quantum chromodynamics (see Section 1.2), there are six types of strong charge - colour charges. A quark can carry one of three colour charges (red, green, or blue) and antiquark can carry one of three anticolour charges. A gluon carries one colour and one anticolour charge. Both baryons and mesons are colourless.

Weak interaction is responsible for, e.g., nuclear β -decay involving emission of electron and neutrino. It is mediated by W^\pm and Z^0 bosons. These bosons are very massive and hence give rise to interaction of very short range. Processes with exchange of W^\pm are called charged-current weak interactions. Processes with exchange of Z^0 are called neutral-current weak interactions. Weak interaction takes place between

all quarks and leptons.

Gravitational interaction acts between all types of particles. It is much weaker than other fundamental interactions; it is dominant on the astronomical scale. It is mediated by hypothetical graviton. It is negligible in particle physics at accelerator energies. It is also cumulative (there is only one sign of gravitational charge) which means that gravitational potential experienced by a particle is sum of potentials created by all other particles.

Weak and electromagnetic interactions are unified and have the same strength at very high energies. Gravitational interaction is not included in the Standard Model. The properties of interactions are summarized in Table 2

	Gravitational	Electromagnetic	Weak	Strong
Gauge boson(s)	graviton	photon	W^\pm, Z^0	gluon
its spin ^{parity}	2^+	1^-	$1^-, 1^+$	1^-
and mass [GeV]	0	0	80.2, 91.2	0
range [m]	∞	∞	10^{-18}	$\leq 10^{-15}$
source	mass	electric charge	weak charge	colour charge
coupling constant	$\frac{G_N M^2}{4\pi\hbar c}$ $= 5 \times 10^{-40}$	$\alpha = \frac{e^2}{4\pi\hbar c}$ $= \frac{1}{137}$	$\frac{G(MC^2)^2}{(\hbar c)^3}$ $= 1.17 \times 10^{-5}$	$\alpha_S \leq 1$
typical cross-section [m ²]		10^{-33}	10^{-39}	10^{-30}
typical lifetime [s]		10^{-20}	10^{-10}	10^{-23}

Table 2: The fundamental interactions ($Mc^2 = 1 \text{ GeV}$)

1.2 Quantum Chromodynamics

Quantum chromodynamics (QCD) is the theory of strong colour interaction between quarks. The interquark interactions, mediated by gluon, are assumed to be invariant under colour interchange. For this reason, gluons carry colour-anticolour pair belonging to the following octet

$$r\bar{b}, r\bar{g}, b\bar{g}, b\bar{r}, g\bar{r}, g\bar{b}, \frac{1}{\sqrt{2}}(r\bar{r} - b\bar{b}), \frac{1}{\sqrt{3}}(r\bar{r} + b\bar{b} - 2g\bar{g})$$

where r represents red, b blue, and g green colours.

The potential between two quarks has form

$$V = -\frac{4}{3} \frac{\alpha_S}{r} + kr.$$

where $k = 0.87 \text{ GeV fm}$. At short distances, the potential is assumed to be of the Coulomb type. At the long distances, it is assumed that quarks are held together by colour lines of force which gluon-gluon interactions pull together into a form of tube or string. When pulling out this string far enough, it becomes energetically favourable to create a new quark-antiquark pair. Thus, attempt to free a quark from hadron simply results in the production of a new meson.

The coupling constant of QCD is α_S . It expresses the value of coupling constant α at given value of

squared momentum transfer q^2 ,

$$\alpha_S(q^2) = \frac{1}{B \ln\left(\frac{q^2}{\Lambda^2}\right)},$$

where B and Λ^2 [8] are defined as

$$B = \frac{1}{12\pi} (11n_b - 4n_f),$$

$$\Lambda^2 = \mu^2 \exp\left(-\frac{1}{B\alpha_S(\mu^2)}\right),$$

where n_b is number of degrees of freedom for bosons and n_f is number of degrees of freedom for fermions and μ is renormalization scale. For asymptotically large q^2 , $\alpha_S \rightarrow 0$, i.e. quarks behave as if they are free. This phenomenon is called asymptotic freedom.

1.3 The parton model

The parton model describes interactions of hadrons as interactions of its point-like constituents. These constituents, called partons, were subsequently identified with quarks and gluons. Each parton carries part of proton's momentum. In the proton, there are quarks uud (called valence quarks) and number of quark-antiquark pairs (called sea quarks).

Interactions [11] in the high-energy hadron collisions can be classified either as hard or soft. The rates and event properties of hard processes can be predicted with good precision by perturbative QCD (pQCD). The soft processes are dominated by non-perturbative QCD effects. Those are less understood.

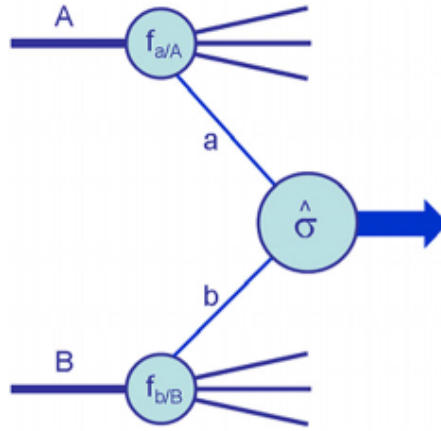


Figure 1: Diagrammatic structure of a generic hard scattering process [11]

Cross-section of these processes can be calculated using factorization theorem as

$$\sigma_{AB} = \int dx_a dx_b f_{a/A}(x_a, Q^2) f_{b/B}(x_b, Q^2) \widehat{\sigma}_{ab \rightarrow X}$$

where A and B are incoming hadrons, x_a is a fraction of original hadron momentum carried by parton a , x_b is a fraction of original hadron momentum carried by parton b , $f_{a/A}$ is parton distribution function of parton a in hadron A , $f_{b/B}$ is parton distribution function of parton b in hadron B , and $\widehat{\sigma}_{ab \rightarrow X}$ is parton level cross-section calculable in perturbative theory (X is final state). The Q is momentum scale of the process.

1.3.1 The parton distribution functions

The parton distribution functions (PDF) cannot be calculated perturbatively. These functions are determined by global fits to data from deep-inelastic scattering (DIS), Drell-Yan (DY) processes (production of massive lepton pair by quark-antiquark annihilation), and jet production. There are two major groups providing PDFs - CTEQ and MRST. In addition, there are also PDFs from Alekhin and two HERA experiments (H1 and ZEUS).

The main source of information about $f_{q/p}$ are DIS structure functions in lepton-lepton scattering and lepton pair production cross-section in hadron-hadron collisions. The hadron-hadron scattering processes with jet final states are a way to measure gluon distribution function $f_{g/p}$. Wide range of Q^2 is covered. HERA data are predominantly at low x , while fixed target DIS and DY data are at higher x . Collider jet data, covering wide range of Q^2 and x , are particularly important in determination of the high x gluon distribution. There is a remarkable consistency between the data in the PDF fits and the perturbative QCD theory fit to them. Both the CTEQ and MRST groups use over 2000 data points in their global pdf analyses and the χ^2/DOF for the fit of theory to data is on the order of unity.

All global analyses use a generic form for the parametrization of both the quark and gluon parton distribution functions [11] at some reference value Q_0

$$F(x, Q_0) = A_0 x^{A_1} (1-x)^{A_2} P(x; A_3, \dots)$$

where Q_0 is chosen to be 1-2 GeV, A_1 parameter is associated with small- x behaviour, and A_2 with large- x behaviour. Function P is a suitably chosen smooth function, depending on one or more parameters, that adds more flexibility to the pdf parametrization.

Uncertainties of PDFs are, conventionally, estimated by comparison of different sets of parton distribution functions. The gluon distribution function has the largest uncertainty out of all parton distribution functions. It can be measured at low x from the scaling violations in the quark distributions. At medium to high x , direct measurement is necessary (e.g. jet measurement).

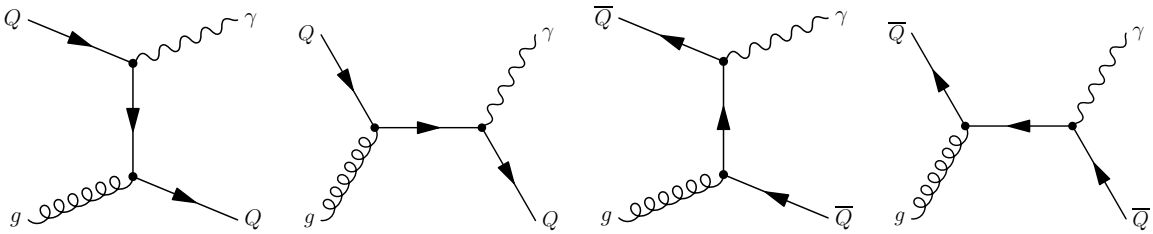


Figure 2: Feynman diagrams for Compton-QCD

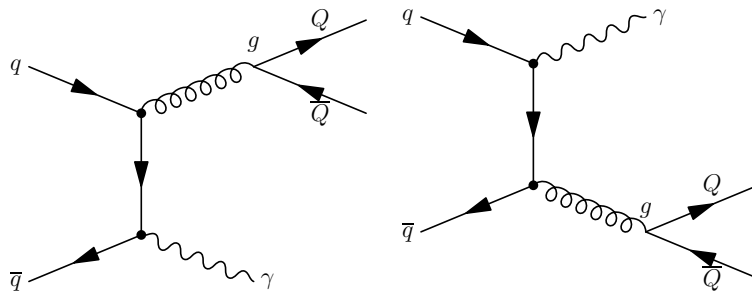


Figure 3: Feynman diagrams for quark-antiquark annihilation

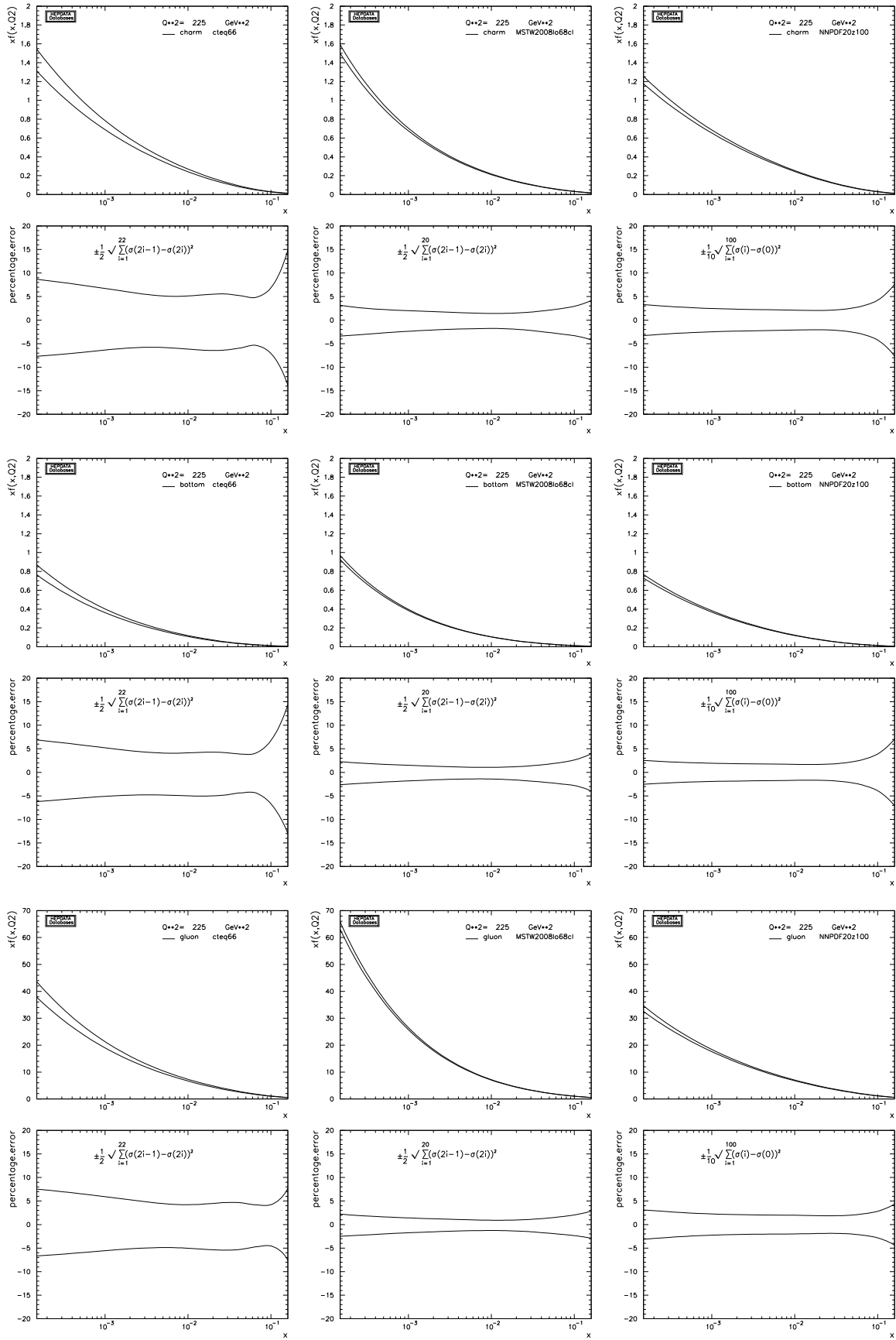


Figure 4: PDFs and their error bands. The top two rows correspond to c quark, middle to b quarks, and bottom to gluons. Left column describes CTEQ6.6, middle column MSTW2008lo68c, and right column NNPDF20_100. Plots were created at <http://hepdata.cedar.ac.uk/pdf/pdf3.html>.

1.4 Prompt photon and b jet processes

Prompt photons can be produced either during the hard interactions (direct photons) or from fragmentation of hard parton (fragmentation photons).

There are two processes which produce direct photon and heavy quark at the lowest order. The first one is Compton-QCD scattering where heavy quark and photon are coming out of quark-gluon interaction. The second process is quark-antiquark annihilation where gluon and photon are products of the annihilation and gluon decays into pair of heavy quarks. Feynman diagrams are on Figures 2 and 3.

The influence of parton distribution functions can be demonstrated on Compton-QCD scattering. The parton distribution functions of c and b quarks and gluon appear in formulas for the cross sections (1) and (2)

$$\sigma(pp \rightarrow \gamma + c + X) \sim \int dx_g dx_c f_{g/p}(x_g, Q^2) f_{c/p}(x_c, Q^2) \hat{\sigma}_{cg \rightarrow \gamma c}^0, \quad (1)$$

$$\sigma(pp \rightarrow \gamma + b + X) \sim \int dx_g dx_b f_{g/p}(x_g, Q^2) f_{b/p}(x_b, Q^2) \hat{\sigma}_{bg \rightarrow \gamma b}^0, \quad (2)$$

where x_g , x_c , and x_b are fractions of the proton momentum carried by the gluon or quark, $f_{g/p}(x_g, Q^2)$, $f_{c/p}(x_c, Q^2)$, and $f_{b/p}(x_b, Q^2)$ are parton distribution function of gluon or quark in the proton at scale Q^2 , and $\hat{\sigma}_{cg \rightarrow \gamma c}^0$ and $\hat{\sigma}_{bg \rightarrow \gamma b}^0$ are cross-sections of Compton-QCD scattering.

Similarly, there are also two processes which produce fragmentation photon and heavy quark at the lowest order. The first one is Compton-QCD scattering producing quark and gluon from quark-gluon interaction. Gluon produces pair of heavy quarks and quark radiates photon (Figure 5). The second process is quark-quark or gluon-gluon interaction producing two quarks. One quark is heavy and the other quark radiates photon (Figure 6).

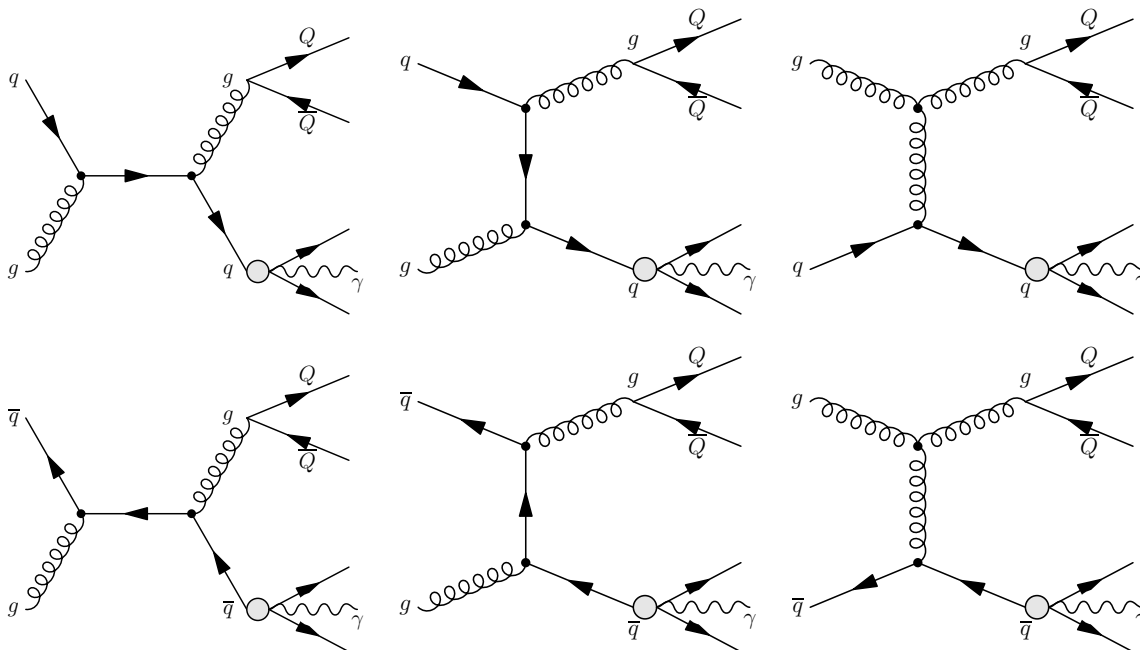


Figure 5: Feynman diagrams for fragmentation photon created with quark-antiquark pair

CTEQ6.6, MSTW2008, and NNPDF2.0 are recommended parton distribution functions for LHC physics [12], [13]. CTEQ6.6 has broader error band than MSTW2008 and NNPDF2.0 because CTEQ6.6

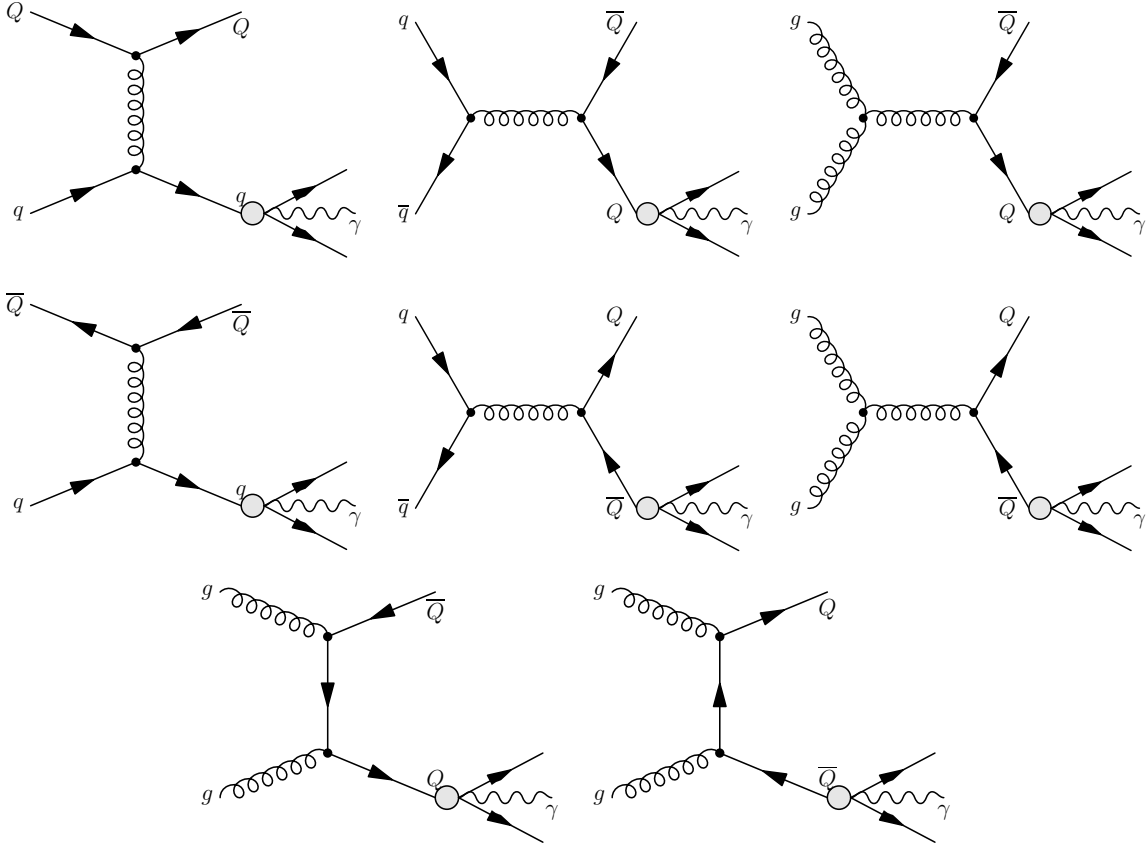


Figure 6: Feynman diagrams for fragmentation photon created with single quark

has uncertainties only at 90 % CL but MSTW2008 and NNPDF2.0 has uncertainties at 68 % CL. Examples of these parton distribution functions for c and b quark and gluon and their error bands are on Figure 4.

There were attempts to constraint the PDFs using cross-section of similar process - photon+jet [14] using 5 fb^{-1} of ATLAS data at $\sqrt{s}=7 \text{ TeV}$. Bayesian reweighting was used on NNPDF 2.1. Figure 7 shows comparison of uncertainties of NP2.1 and uncertainties of NNPDF 2.1 with data from photon+jet analysis added. The effect caused by addition is negligible (especially on gluon PDF). But it was shown that the method can give significant results. The photon+jet toy Monte Carlo with a total uncorrelated experimental uncertainty of 5 % was created and such scenario represents an improvement of about a factor of 2–3 with respect to actual measurement. Result of this addition is shown on Figure 8.

1.4.1 Previous results

Previously, cross-section of processes including prompt photon associated with heavy jet were measured in $p\bar{p}$ collisions at Tevatron's experiments CDF and D0 at $\sqrt{s} = 1.96 \text{ GeV}$.

On CDF [15], the measurement was performed using CDF II detector. It is composed of a central spectrometer measuring charged particle trajectories inside a 1.4 T magnetic field. It is surrounded by electromagnetic and hadronic calorimetry and muon chamber. Central calorimeters cover the region $|\eta| < 1.1$ (the end-wall hadronic calorimeter extends this coverage to $|\eta| < 1.3$).

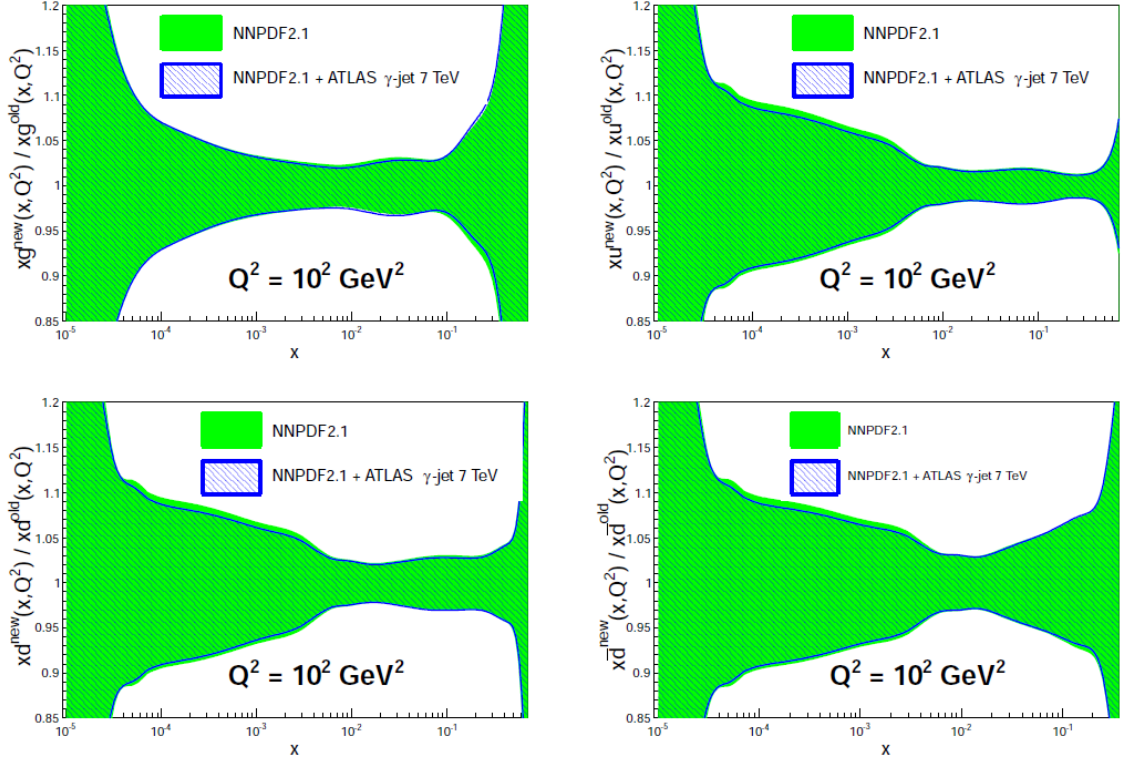


Figure 7: NNPDF 2.1 uncertainties without and with addition of photon+jet data. Result of analysis of ATLAS data

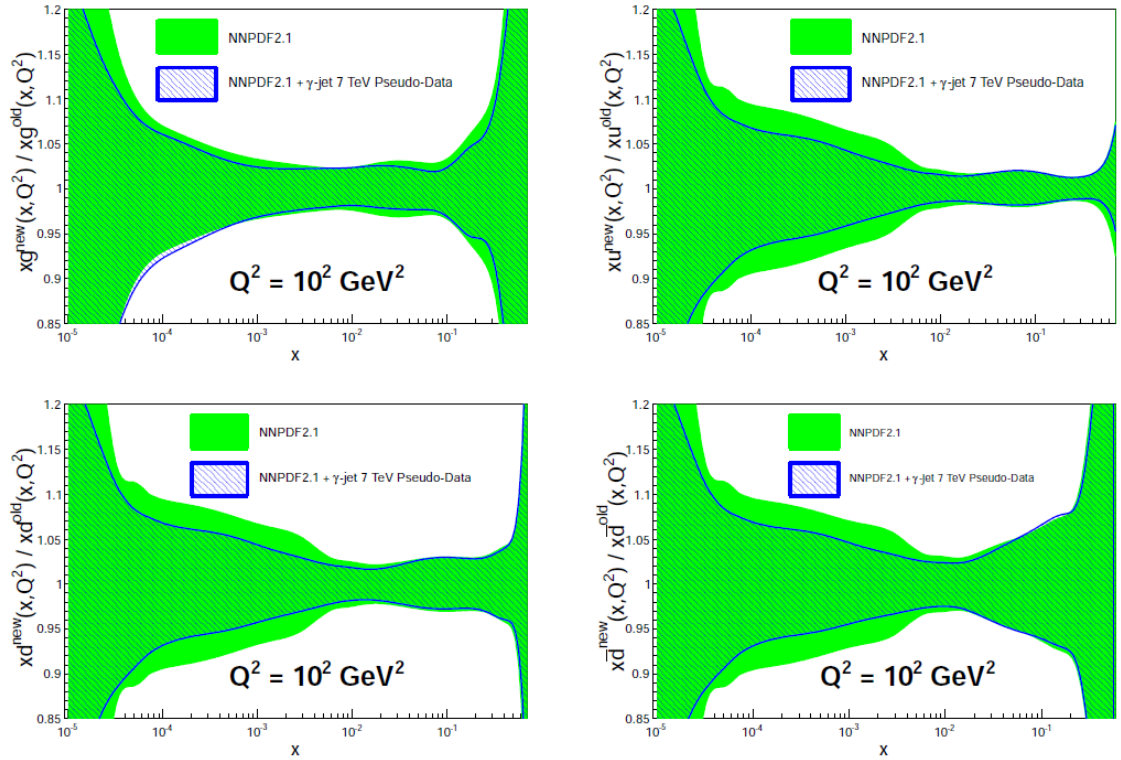


Figure 8: NNPDF 2.1 uncertainties without and with addition of photon+jet data. Result of analysis of toy Monte Carlo samples

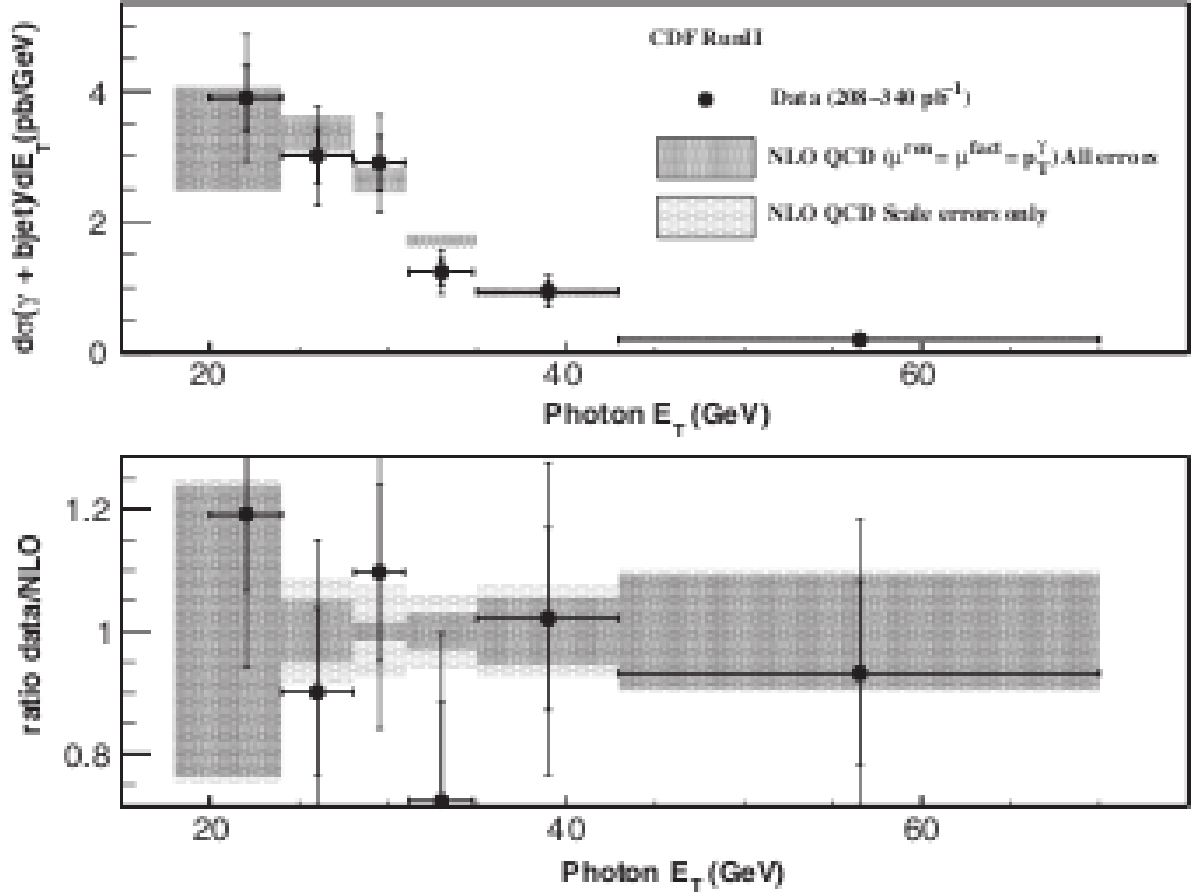


Figure 9: Cross-section measurement at CDF. Top panel: b +photon cross-section as a function of photon E_T , compared to NLO QCD calculations. The bottom panel shows the ratio of data to the NLO calculation.

To measure photons, the CDF experiment used two triggers - high E_T photon (requiring a photonlike object with $E_T > 25$ GeV) and SVT photon (which required a photonlike object with $E_T > 12$ GeV, a jet with $E_T > 10$ GeV, and a track, measured by the silicon vertex tracker (SVT), with $p_T > 2$ GeV/ c , and an impact parameter larger than $120 \mu\text{m}$). The integrated luminosity analysed using high E_T photon was 340 pb^{-1} of data, the integrated luminosity analysed using SVT photon was 208 pb^{-1} of data. Selected events must pass at least one of the two photon triggers, contain an isolated central ($|\eta| < 1.1$) photon with $E_T^\gamma > 20$ GeV and b jet of $E_T > 20$ GeV within $|\eta| < 1.5$. The jets were reconstructed using JETCLU algorithm using radii 0.4 and 0.7 for $E_T^\gamma < 26$ GeV and $E_T^\gamma > 26$ GeV, respectively. In order to reduce contamination from neutral mesons, photon candidates must be isolated from nearby calorimeter deposits and tracks.

Monte Carlo events were simulated using PYTHIA at scale $Q^2 = 225 \text{ GeV}^2$ and using CTEQ5L parton distribution functions. These events were used to estimate photon and jet selection efficiencies. A simulation of the underlying event was included.

Number of events which survived selection criteria was 10900 for high E_T photons and 55800 for SVT photons. The events were divided into bins according to the photon transverse energy. Then the number of events in each bin was corrected for background, trigger, selection, and acceptance efficiency. Also, the number of events was divided by appropriate integrated luminosity.

For systematic uncertainties, only the largest contributions were quantified. The sources of systematic uncertainty which were studied are photon identification, jet energy scale, b -jet identification, and

luminosity.

The theoretical prediction of the cross-section at the next-to-leading order was created. It was derived analytically, using the CTEQ6.6M parton density functions, and a renormalization, factorization, and fragmentation scale set to the transverse momentum of the photon.

The total cross section $\sigma(p\bar{p} \rightarrow \gamma + \geq 1b - \text{jet}) = 54.22 \pm 3.26(\text{stat})_{-5.09}^{+5.04}(\text{syst})$ pb is consistent with next-to-leading order prediction (see Figure 9) of 55.62 ± 3.87 pb.

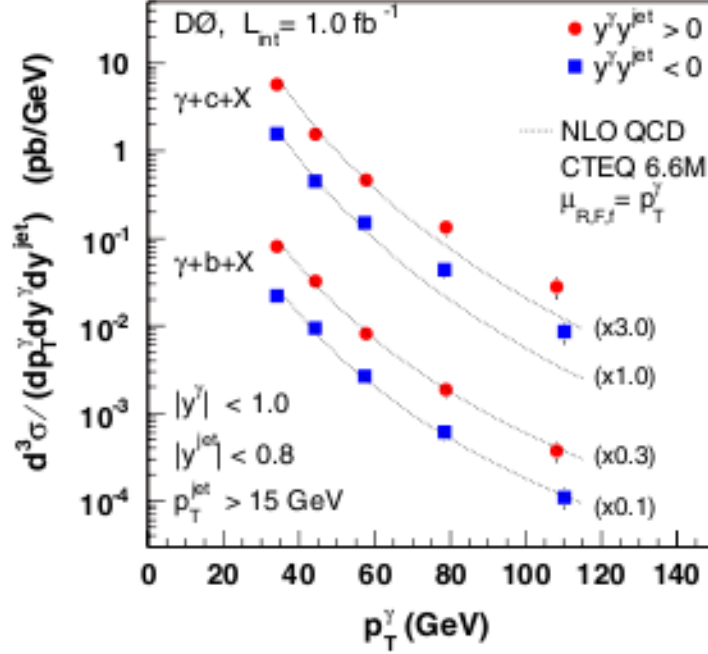


Figure 10: Measurement at D0: the $\gamma + b + X$ and $\gamma + c + X$ differential cross-sections as a function of p_T^γ in the two regions $y^\gamma y^{\text{jet}} > 0$ and $y^\gamma y^{\text{jet}} < 0$

D0 [16] measured triple differential cross-section $d^3\sigma/dp_T^\gamma dy^\gamma dy^{\text{jet}}$ (where p_T^γ is transverse momentum of the photon, y^γ is photon's rapidity, and y^{jet} is rapidity of the jet) using integrated luminosity $1.02 \pm 0.06 \text{ fb}^{-1}$. Differential cross-sections are presented for two regions of kinematics, defined by $y^\gamma y^{\text{jet}} > 0$ and $y^\gamma y^{\text{jet}} < 0$. These two regions provide greater sensitivity to the parton x because they probe different sets of x_1 and x_2 intervals.

Triggers used for analysis identify clusters of large electromagnetic energy. They are based on p_T^γ and on the spatial distribution of energy in the photon shower. Photon candidates are reconstructed from large energy deposits in radius $R=0.4$. Background from dijets was removed from reconstructed photons using artificial neural networks. The leading (highest p_T) photon is required to have $|y^\gamma| < 1.0$ and $30 < p_T^\gamma < 150$.

The events were required to have at least one jet. Jets were reconstructed using D0 Run II algorithm with a radius of 0.5. The leading jet is required to have $|y^{\text{jet}}| < 0.8$ and $p_T^{\text{jet}} > 15$ GeV. Also, it is required to have at least two associated tracks with $p_T > 0.5$ GeV and the track leading in p_T must have $p_T > 1.0$ GeV, and each track must have at least one hit in the silicon microstrip tracker. These conditions ensure that sufficient amount of information is kept to classify the jet as a heavy-flavour candidate. Light jet background was removed using artificial neural network.

A primary collision vertex has to have more than two tracks and has to be located within 35 cm of the center of the detector along the beam axis. The missing transverse momentum in the event is required to be $< 0.7 p_T^\gamma$ (to suppress background from cosmic-ray muons and W decays).

Signal events in the Monte Carlo events were generated using PYTHIA 6 and processed through a GEANT-based simulation of the detector geometry and response, and reconstructed using the same software as for the data.

The main systematic uncertainties stems from photon purity, heavy-flavour fraction fit, jet selection efficiency, photon selection efficiency, and luminosity.

NLO pQCD predictions were made with renormalization, factorization, and fragmentation scales set to p_T^γ . It uses CTEQ6.6M parton distribution function.

About 13000 events remain in the data sample after applying all selection criteria. The cross-section based on those events was compared with NLO pQCD predictions. For $\gamma + b + X$, they agree with the measurements (see Figure 10) over the entire p_T^γ range.

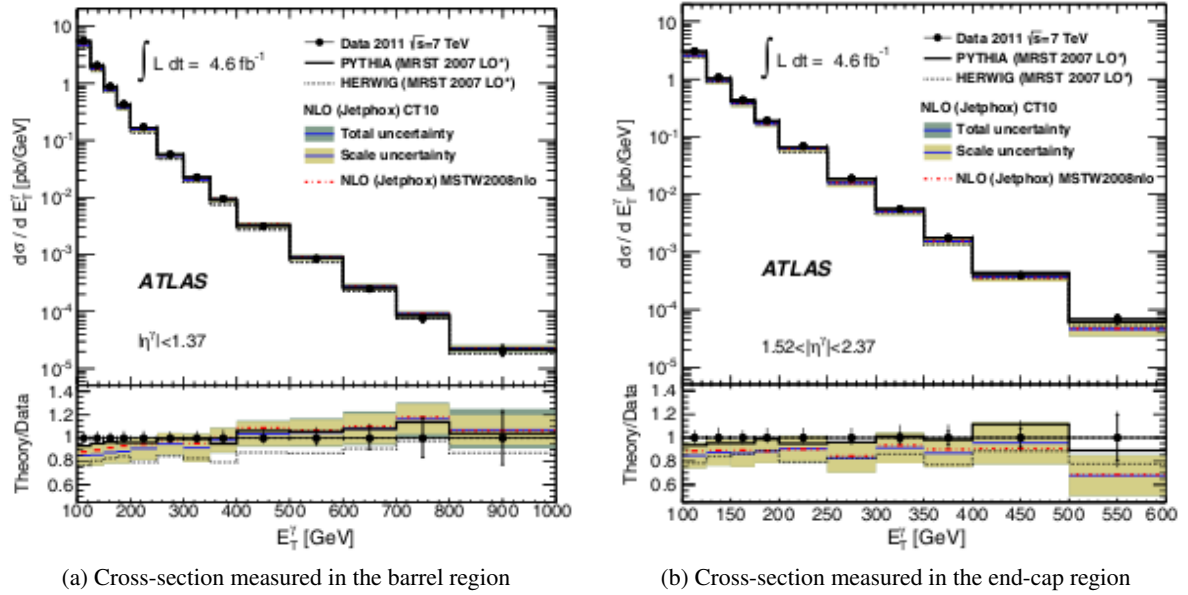


Figure 11: Measured and expected inclusive isolated prompt photon cross-section as a function of transverse energy of the photon at the ATLAS experiment

In the ATLAS experiment (see Section 3), photon and b jet were measured separately so far. Cross-section of the inclusive isolated prompt photon [17] was measured at $\sqrt{s} = 7$ GeV using 4.6 fb^{-1} of data recorded in 2011. Only events where the Inner Detector and Calorimeter are fully operational and that have good data quality are used. In order to reduce non-collision background, the events are required to have a reconstructed primary vertex consistent with average beam-spot and with at least three associated tracks.

Events were triggered using a high-level photon trigger, with a nominal E_T^γ threshold of 80 GeV and photons with $E_T^\gamma > 100$ GeV were used for analysis. The photons are measured in E_T^γ range between 100 GeV and 1 TeV and in pseudorapidity range $|\eta| < 1.37$ (barrel region) and $1.52 < |\eta| < 2.37$ (the end-cap region).

Prompt photons are expected to be more isolated than hadronic activity in the background (see Section 4.1.5). Photons are considered isolated if transverse energy (E_T^{iso}) within a cone of radius $\Delta R < 0.4$ centered around pseudorapidity and azimuthal angle is smaller than 7 GeV. Also, shower shape variables are used to further discriminate the signal from the background. So called “tight” identification criteria are created from shower shape variables (see Section 4.1.4). The cross-section measurement is based on tight photons.

Monte Carlo events were simulated using PYTHIA 6.4 and Herwig 6.5. Both PYTHIA and Herwig used

modified MRST2007 parton distribution function. The ATLAS detector response is simulated using the GEANT4 program.

The background (hadronic jets containing π^0 mesons carrying most of the jet energy and decaying to photon pairs) was estimated using 2D sideband method (see Section 9.2). There is a possible residual background from electrons that fake photons. This background is estimated to be below 0.5 %.

The next-to-leading order theoretical calculation using Jetphox 1.3 were done. It implements NLO QCD calculation of both direct and fragmentation contributions. It used BFG set II photon fragmentation function and CT10 and MSTW2008NLO parton distribution functions.

The NLO calculations agree with the data (see Figure 11) up to the highest E_T^γ considered. The data are somewhat higher than the central NLO calculation for low E_T^γ but agree within the theoretical uncertainties. At the LO, PYTHIA model describes the data fairly well while HERWIG falls below the data by 10%-20%.

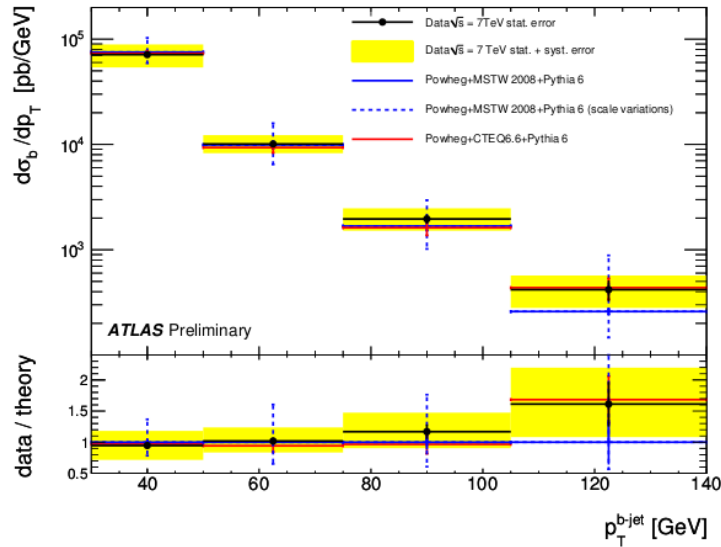


Figure 12: Measured differential cross-section $d\sigma/dp_T^{b-jet}$ using 4.8 pb^{-1} of data at the ATLAS experiment. The data are compared to NLO predictions using Powheg and PYTHIA 6

Production cross-section of the b jet was measured using muons in jets [18]. The measurement uses 4.8 pb^{-1} of data at $\sqrt{s} = 7 \text{ GeV}$ recorded in 2010.

The events were selected using a trigger requiring a reconstructed jet with $p_T > 5 \text{ GeV}$ matched to a reconstructed muon with $p_T > 4 \text{ GeV}$. Also, events are required to have well reconstructed primary vertex with at least 10 tracks.

Jets are reconstructed from topological calorimeter energy clusters using the anti- k_T algorithm with a radius parameter $R = 0.4$. They are also required to satisfy $20 < p_T^{jet} < 180 \text{ GeV}$ and $|y^{jet}| < 2.1$.

Muons in $dR < 0.4$ are associated to jet. Muon tracks are required to have at least seven hits in the silicon detectors, to be within $|\eta^\mu| < 2.5$. Also, they have to have a transverse and a longitudinal impact parameter with respect to the primary vertex of less than 2 mm, and to have a transverse momentum $p_T^\mu > 4 \text{ GeV}$. If more than one muon associated to a jet passes these selection cuts, the muon with the highest transverse momentum is used in the analysis.

The p_T^{rel} (where $p_T^{rel} = p_\mu \sin \theta^{rel}$ and θ^{rel} is angle between the muon momentum and the direction of associated jet) method is used to extract b jets from the sample - the b , c , and light jet templates (of p_T^{rel} variable) are fitted to data.

Monte Carlo events were generated using with PYTHIA 6.4.1 using the MRST LO* parton distribution functions. To simulate the detector response, the generated events are processed, using GEANT4.

The next-to-leading order calculations were done with Powheg using two parton distribution functions - MSTW 2008 NLO and CTEQ6.6. The hard processes were showered with PYTHIA 6.4.

Then the numbers of b-jets were unfolded using bin-by-bin method. Then the cross-section was compared to the NLO calculations. They reproduce data rather well (see Figure 12). The prediction using CTEQ6.6 gives a very good agreement with the measured cross-section. The central values using MSTW 2008 NLO predict a p_T^{bjet} dependence slightly harder than the measurement, but differences are within systematic uncertainties.

The production of b jet was later measure using 34 pb^{-1} [19]. The measurement was extended to range $20 < p_T < 400 \text{ GeV}$. The results were compared to NLO predictions. It is in good agreement with POWHEG+PYTHIA predictions (see Figure 13).

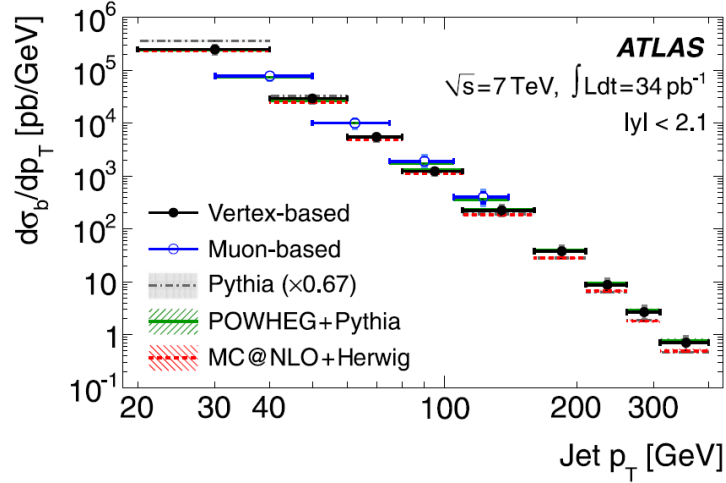


Figure 13: Differential b-jet cross-section using 34 pb^{-1} of data at the ATLAS experiment. The data are compared to NLO predictions using PYTHIA 6, Powheg, and MC@NLO

Closer to the measurement of photon and b-jet is measurement of photon+jet performed at data at $\sqrt{s} = 7 \text{ GeV}$ collected during the year 2010 [20].

Events used for the analysis had to pass detector and data-quality requirements. Events were also required to have a reconstructed primary vertex, with at least five associated charged-particle tracks with $p_T > 150 \text{ MeV}$, consistent with the average beam-spot position.

Photons were triggered by a single photon trigger with a nominal transverse energy threshold 40 GeV . They were required to have transverse momentum $p_T > 45 \text{ GeV}$ and pseudorapidity in range $|\eta^\gamma| < 2.37$ (events with photon in $1.37 < |\eta^\gamma| < 1.52$ were excluded). The “tight” identification criteria were used on photon. Also, the photon had to be isolated which in this case means that the isolation energy was required to be below 3 GeV .

Jets used in the analysis were reconstructed using anti- k_T algorithm with distance parameter $R=0.6$. After calibration, jets were required to have transverse momentum $p_T > 40 \text{ GeV}$ and rapidity in range $|\eta^{\text{jet}}| < 2.37$. The distance of leading photo and jet was set to $\Delta R > 1$.

Monte Carlo events were simulated using PYTHIA 6.423 and HERWIG 6.510. For fragmentation into hadrons PYTHIA used Lund string model and HERWIG used cluster model. The modified leading-order MRST2007 parton distribution functions were used. Simulation of underlying events was performed by the multiple-parton interaction model for PYTHIA and by JIMMY for HERWIG. All the samples of generated events were passed through the GEANT4-based ATLAS detector simulation program.

After selection, 124000 events remained. The background from multi-jet processes in which jet is misidentified as a photon was subtracted using 2D sideband method (see Section 9.2). The cross-section

was measured as a function of following variables: E_T^γ , p_T^{jet} , $|y^{\text{jet}}|$, $\Delta\phi^{\gamma j}$, $m^{\gamma j}$, and $|\cos\theta^{\gamma j}|$ (where E_T^γ is transverse energy of the leading-photon, p_T^{jet} is transverse momentum of the leading-jet, $|y^{\text{jet}}|$ is rapidity of the leading-jet, $\Delta\phi^{\gamma j}$ is the difference between the azimuthal angles of the photon and the jet, $m^{\gamma j}$ is photon-jet invariant mass, and $|\cos\theta^{\gamma j}|$ is cosine of scattering angle in the centre-of-mass frame).

The NLO calculations were computed using JETPHOX. It was set to use five flavours and renormalization, factorisation, and fragmentation scales were chosen to equal to transverse energy of the photon. The calculations used CTEQ6.6 parton distribution functions and BFG set II photon fragmentation functions. Prediction for CT10 and MSTW2008nlo were also computed.

The NLO predictions give a good description of cross-section measured as function of E_T^γ and p_T^{jet} . In $|y^{\text{jet}}|$ distribution, shape and normalization is described well. $\Delta\phi^{\gamma j}$ distribution fails to describe values less than $\pi/2$ because in calculation, photon and jet cannot be in the same hemisphere. Measurements using $m^{\gamma j}$ and $|\cos\theta^{\gamma j}|$ are described well by the calculations.

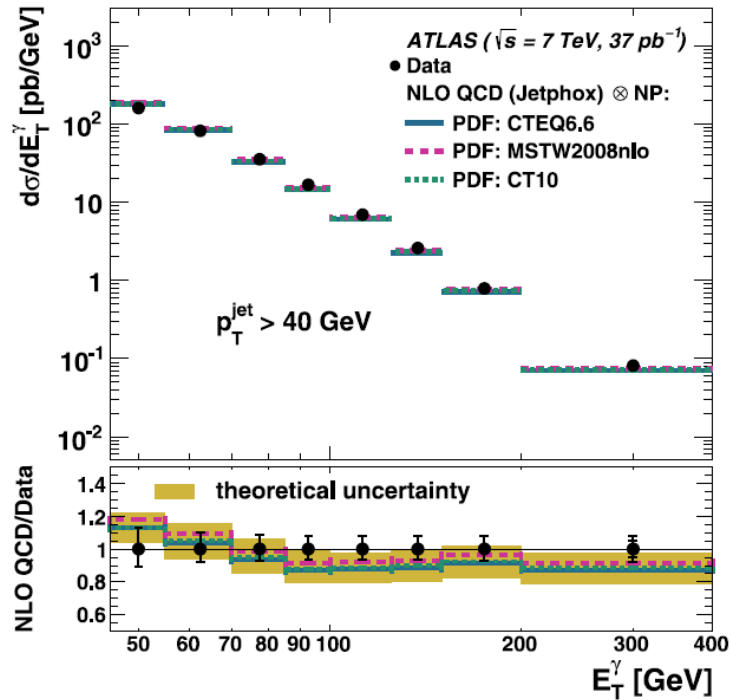


Figure 14: Measured cross-section for isolated-photon plus jet at the ATLAS experiment. The data are compared to NLO predictions using Jetphox

Motivation of this thesis is based on these measurements. The analysis of the event selection was presented last year at Workshop of Experimental Nuclear and Particle Physics [21].

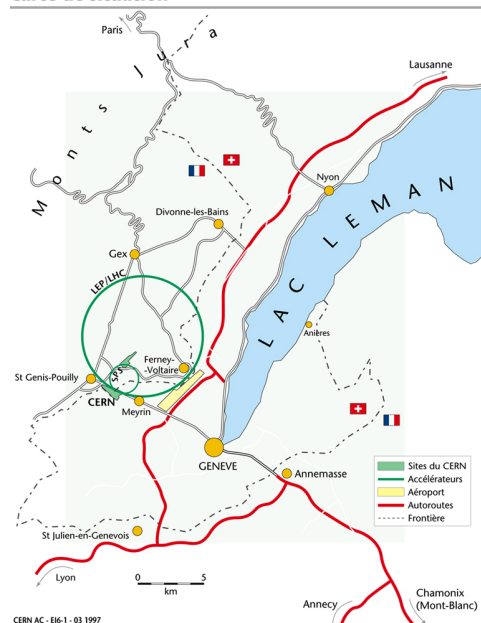
2 The LHC

The LHC is acronym for Large Hadron Collider (Figure 15b). It is a particle accelerator located at CERN (Figure 15a) near Geneva. CERN stands for Conseil Européen pour la Recherche Nucléaire (European Organization for Nuclear Research). LHC is designed to provide proton-proton collisions at centre-of-mass energy of 14 TeV and luminosities up to $10^{34} \text{ cm}^{-2} \text{ s}^{-1}$. It also can provide collisions of fully stripped lead ions ($^{208} \text{Pb}^{82+}$) at centre-of-mass energy of 2759 GeV/nucleon and luminosities up to $10^{27} \text{ cm}^{-2} \text{ s}^{-1}$.

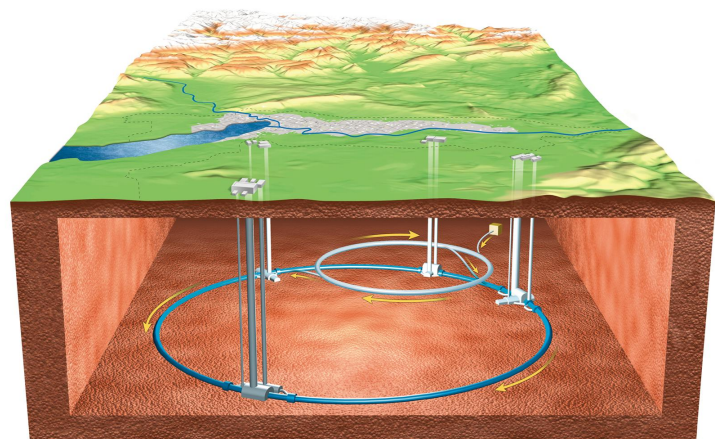
There are four large experiments located at LHC which are recording and analysing collisions:

- ALICE - detector specialised for studies of heavy-ion collisions
- ATLAS - large multi-purpose detector
- CMS - large multi-purpose detector
- LHCb - detector specialised for studies of b-physics

Carte de situation



(a) Map of the Geneva region and of the LHC [22]



(b) Overall view of the LHC [23]

Figure 15: CERN and LHC

2.1 History

The first ideas about planned multi-TeV proton collider at CERN appeared during early 1980s [24]. The LHC was approved by the CERN Council on December 16, 1994. The first proton beams were circulating in both directions at energy of 450 GeV on September 10, 2008.

A few days later, an accident during commissioning work to adapt magnets for higher energies caused severe damage to the machine. A malfunctioning magnet interconnect produced an electric arc which destroyed a helium vessel. This caused a chain reaction which resulted in many magnets being displaced and damaged and a long section of the vacuum pipe was polluted. It took about one year to repair the

damage. Also, the cause of the accident was investigated and machine protection system was improved.

First proton-proton collisions after the accident started on November 23, 2009. The beam energy was 450 GeV. Before the end of the year, the beam energy was increased to 1.18 TeV. After the technical stop during the winter, on March 30, 2010, the LHC started colliding proton-proton beams at energy of 3.5 TeV and luminosity $10^{27} \text{ cm}^{-2} \text{ s}^{-1}$. Since then, the luminosity was increased.

2.2 Basic characteristics

LHC is located in the tunnel previously occupied by the LEP (Large Electron–Positron Collider) [25]. The circumference of accelerator ring is 26658.883 m. LHC consists of eight arcs and eight straight sections. The straight sections, called points or insertions, can serve as an experimental or utility insertion. The four large experiments are located at points 1, 2, 5, and 8. Injector systems for beam 1 and beam 2 are located at points 2 and 8, respectively. Both insertions 3 and 7 contain two collimation systems. Insertion 4 contains two RF systems (one independent system for each beam). Point 6 contains the beam dump insertion.

For the proton-proton collisions, the colliding particles are inserted into the collider with energy 450 GeV. Lead ions are inserted into the collider with energy 36.9 TeV (177.4 GeV/nucleon).

3 The ATLAS experiment

The ATLAS experiment is a general purpose detector located at LHC. ATLAS stands for ‘‘A Toroidal LHC Apparatus’’. It is located at Point 1, directly opposite the main entrance to the CERN site. This section is a review from [26].

The ATLAS detector is nominally forward-backward symmetric with respect to the interaction point. The overall layout of the ATLAS detector is shown on Figure 16. It consists of three different detector systems (starting with detectors closest to the interaction point) - the Inner Detector (Section 3.1), system of calorimeters (Section 3.2), and the Muon spectrometer (Section 3.3). The overview of number of readout channels in in Table 4. The detector is using bending of charged particles trajectories in magnetic field for measurement. The magnetic field is created by the system of magnets (Section 3.4). Event data are obtained from the detector by trigger and data acquisition system (Section 3.6). They are then processed and analysed using distributed computing (Section 3.7). For luminosity measurements, ATLAS is using detectors located far from the interaction point (Section 3.5). The detectors also require cooling. Summary of cooling substances used in detector systems is shown in Table 3. The overall weight of the detector is approximately 7000 tonnes.

System	Medium	Operating Temperature [°C]
Tile calorimeter	water	17 to 22
LAr calorimeter	water	17 to 22
Muon spectrometer	water	17 to 22
pixel, SCT	C_3F_8	-30 to 10
TRT	C_6F_{14}	14 to 22

Table 3: Major cooling systems operating in the ATLAS

To investigate variables used to determine particle direction, the coordinate system must be described first. The origin of the coordinate system is the nominal interaction point. The z-axis runs along the beam. The x-y plane is transverse to the beam direction. The positive x-axis points to the centre of the LHC ring, the positive y-axis points upwards. The azimuthal angle ϕ is measured around the beam axis. The polar angle θ is measured from the beam axis. Then the pseudorapidity is defined as $\eta = -\ln \tan(\theta/2)$ and distance as $\Delta R = \sqrt{\Delta\eta^2 + \Delta\phi^2}$. The transverse momentum p_T , is defined in the x-y plane.

3.1 The Inner Detector

The Inner Detector is the innermost detector system in ATLAS. The overall layout of the Inner Detector (ID) is shown on Figure 17. For charged tracks above a given p_T threshold (0.5 GeV nominally) and within the pseudorapidity range $|\eta| < 2.5$, it provides hermetic and robust pattern recognition, excellent momentum resolution and both primary and secondary vertex measurements. It also provides electron identification over the pseudorapidity range $|\eta| < 2.0$. Charged particles tracks are bent by 2T solenoidal magnetic field provided by the central solenoid (see Section 3.4).

The Inner Detector consists of three sub-detectors. At inner radii, there are silicon detectors using discrete space-points from silicon pixel layers (pixel detector) and stereo pairs of silicon microstrip layers (SCT). To maintain an adequate noise performance after radiation damage, the silicon sensors must be kept at temperature approximately -5 to -10 °C. At larger radii, detector consisting of many layers of gaseous straw tube elements interleaved with transition radiation material (TRT) is used. The TRT operates at room temperature.

The pixel modules are arranged in three barrel layers and two end-caps each with three disk layers. Each module consists of stack, from the bottom up, of 16 front-end electronics chips, bump bonds

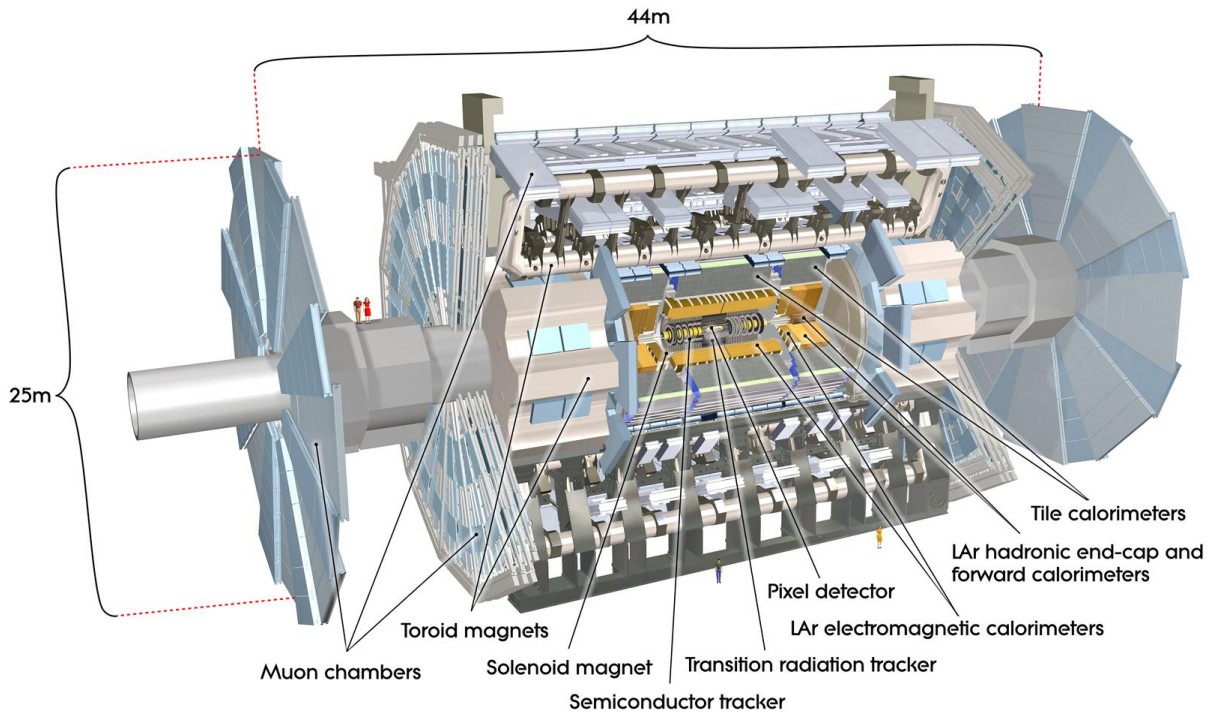


Figure 16: Cut-away view of the ATLAS detector

(connecting the electronics channels to pixel sensor elements), the sensor tile, flexible polyimide printed-circuit board, and polyimide pig-tail with Cu lines and a connector (barrel modules) or a wire micro-cable (end-cap modules). There are 1744 pixel sensors in the Inner Detector. Each sensor has 47232 pixels.

The SCT consists of 4088 modules in four coaxial cylindrical layers in the barrel region and two end-caps each containing nine disk layers. The barrel SCT modules consist of four sensors, two each on the top and bottom side. They are glued on thermal pyrolytic graphite (TPG) baseboard. The end-caps SCT modules have two sets of sensors glued back-to-back around a central TPG spine. There are 15912 SCT sensors in the Inner Detector. Each sensor has 768 active strips.

The TRT contains up to 73 layers of straws interleaved with polypropylene fibres (in the barrel) and 160 straw planes interleaved with polypropylene radiator foils separated by a polypropylene net (in the end-cap). The straws consist of polyimide drift tubes of 4 mm diameter and anodes ($31 \mu\text{m}$ diameter tungsten wires plated with $0.5\text{--}0.7 \mu\text{m}$ gold). The straw tube wall is made of two $35 \mu\text{m}$ thick multi-layer films bonded back-to-back. The straws are mechanically stabilised using carbon fibres. The straws are filled with gas mixture (70% Xe, 27% CO_2 and 3% O_2) and operated in an envelope of CO_2 .

3.2 Calorimeters

The system of calorimeters in the ATLAS experiment uses two kinds of active medium - liquid argon and scintillating tiles. There are several kinds of calorimeters using liquid argon. In the barrel, it is electromagnetic calorimeter. In the end-caps, there are a electromagnetic end-cap calorimeter (EMEC), a hadronic end-cap calorimeter (HEC), and a forward calorimeter (FCal). As for calorimeters with scintillating tiles, there is TileCal (tile calorimeter). The overall layout of system of calorimeters in the ATLAS detector is shown on Figure 18.

The electromagnetic calorimetry is used for electron and photon identification and measurements.

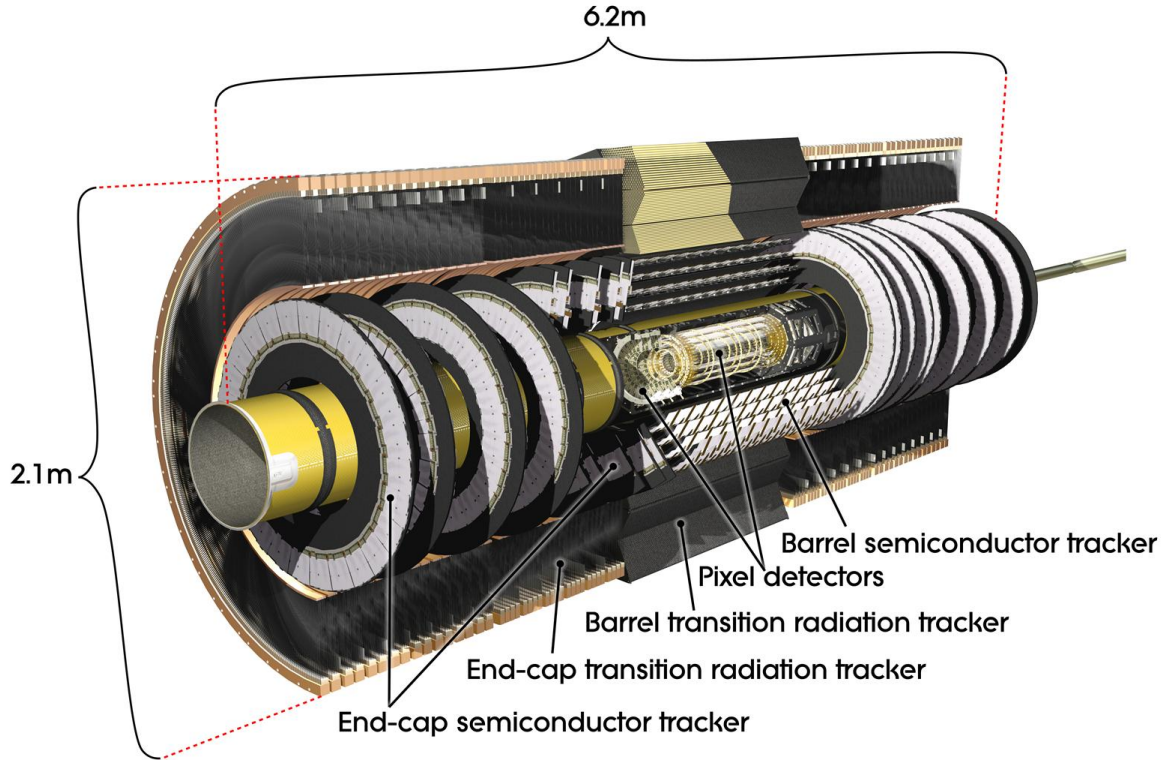


Figure 17: Cut-away view of the Inner Detector

The hadronic calorimetry is used for accurate jet and missing transverse energy measurements. The electromagnetic coverage at higher pseudorapidities ($3.1 < |\eta| < 4.9$) is provided by the FCal. The hadronic calorimetry is extended to larger pseudorapidities ($|\eta| < 4.9$) by the HEC and the FCal.

The electromagnetic calorimeter is lead-liquid argon detector with accordion-shape (accordion waves run in ϕ , from the center of the detector to the edge) absorbers and electrodes. It reaches the pseudorapidity range $|\eta| < 3.2$. In the barrel (made of two half-barrels), the accordion waves are axial and run in ϕ . In the end-caps, the waves are parallel to the radial direction and run axially. The absorbers are made of lead plates with two stainless-steel sheets glued to them. The readout electrodes are positioned in the middle of the gap between the absorbers by spacers. The electrodes consist of three conductive copper layers (the inner one is used for reading out the signal) separated by insulating polyimide sheets. In the region ($0 < |\eta| < 1.8$) the electromagnetic calorimeters are complemented by presamplers which provide a measurement of the energy lost in front of the electromagnetic calorimeters. The energy resolution degrades significantly in the transition region between the barrel and end-cap cryostats ($1.37 < |\eta| < 1.52$). This crack region is used neither for photon identification nor for precision measurements with electrons. In the data collected in 2012, the crack region location was changed to $1.37 < |\eta| < 1.56$ (see [27]).

The hadronic end-cap calorimeter uses copper as absorber and liquid-argon as the active medium. It covers pseudorapidity range $1.5 < |\eta| < 3.2$. It consists of two wheels in each end-cap. Three electrodes divide the gaps between absorbers into four separate LAr drift zones. The middle electrode is the readout electrode. The space between the electrodes is maintained using a honeycomb sheet. The hadronic end-cap calorimeter has 5632 readout channels.

The forward calorimeter is split onto three modules - one electromagnetic using copper as absorber and two hadronic ones using tungsten as absorber. Liquid argon is used as active medium. Pseudorapidity range $3.1 < |\eta| < 4.9$ is covered by FCal. The FCal design is using electrode structure of small-diameter

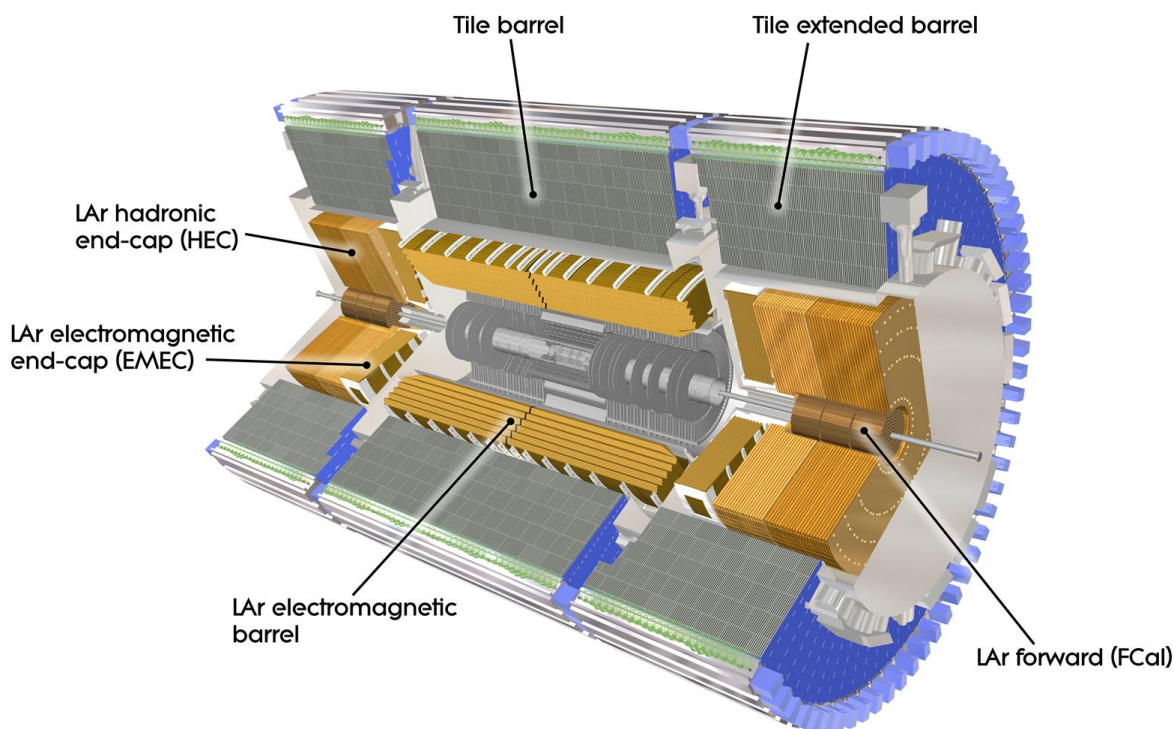


Figure 18: Cut-away view of calorimeter system

rods, centred in tubes which are oriented parallel to the beam direction. Liquid argon gap between rod and tube is very small. An electrode consists of a co-axial copper rod (for electromagnetic part) or tungsten rod (for hadronic part) and copper tube separated by a precision, radiation-hard plastic fibre wound around the rod. Each FCal has 1762 channels.

The tile calorimeter is using steel as the absorber and scintillator as the active medium. It covers the range $|\eta| < 1.7$. It is composed of three parts, one central barrel and two extended barrels. The tiles, made of the base material (polystyrene) and wavelength-shifting fluors (the polystyrene is doped with 1.5% PTP and with 0.044% POPOP), are oriented radially. They are read out by wavelength-shifting fibres on the tile edges which collect the scintillation light produced in the scintillators and convert it to a light with longer wavelength. The readout fibres are grouped into the readout photomultiplier tubes (PMT's).

3.3 The Muon Spectrometer

The muon spectrometer is the most outer part of the ATLAS detector. It is designed to detect charged particles exiting the barrel and end-cap calorimeters. It measures particles momentum in the pseudorapidity range $|\eta| < 2.7$ and also triggers on particles in the region $|\eta| < 2.4$. It consists of two precision-tracking chambers (MDT's and CSC) and two fast trigger chambers (RPC and TGC). The overall layout of the muon spectrometer is shown on Figure 19.

The chambers in the barrel are arranged in three concentric cylindrical shells around the beam axis. In the end-cap regions, muon chambers form large wheels, perpendicular to the z-axis.

The Monitored Drift Tube chambers (MDT's) are precision-tracking chambers consisting of three to eight layers of drift tubes. The drift tubes are filled with gas mixture (93% of Ar and 7% of CO₂). The

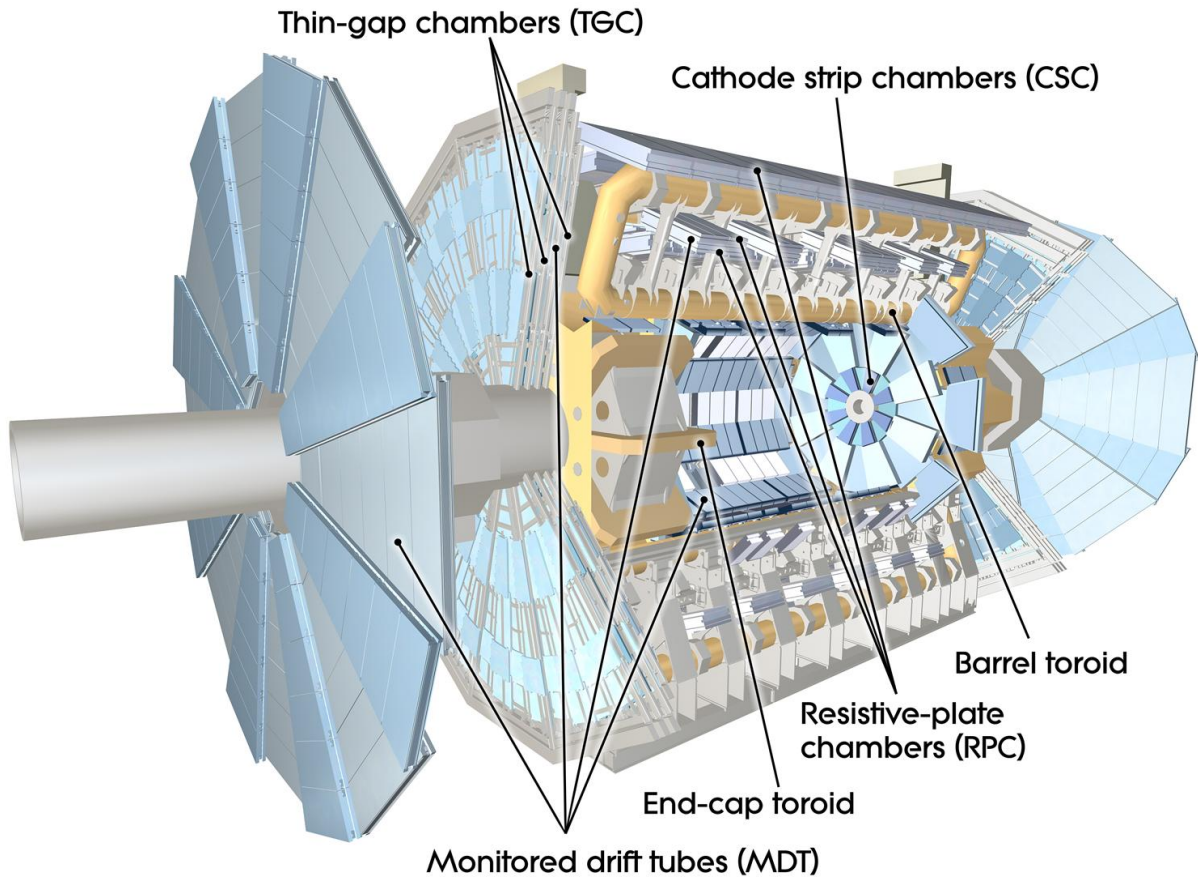


Figure 19: Cut-away view of the muon spectrometer

electrons resulting from ionisation are collected at the central tungsten-rhenium wire. There are 1088 chambers in the muon spectrometer. They cover the pseudorapidity range $|\eta| < 2.7$ (except in the innermost end-cap layer where their coverage is limited to $|\eta| < 2.0$). They are rectangular in the barrel and trapezoidal in the end-cap.

The Cathode-Strip Chambers (CSC) are precision-tracking chambers located at two end-cap disks with eight chambers each. They are multiwire proportional chambers with the wires oriented in the radial direction. Both cathodes are segmented, one with the strips perpendicular and the other parallel to the wires. The position of the track is obtained by interpolation between the charges induced on neighbouring cathode strips. They are used in the innermost tracking layer at $2 < |\eta| < 2.7$. The chambers are filled with gas mixture (80% of Ar and 20% of CO_2).

The Resistive Plate Chambers (RPC) are trigger chambers located in the barrel region in three concentric cylindrical layers around the beam axis. They cover the pseudorapidity range $|\eta| < 1.05$. They are gaseous parallel electrode-plate detectors. They consist of two rectangular detectors with two independent detector layers. The detector layer consists of two parallel resistive plates, made of phenolic-melaminic plastic laminate. On the outer faces of the resistive plates are mounted metallic strips used for readout. The chambers are filled with gas mixture (94.7% of $\text{C}_2\text{H}_2\text{F}_4$, 5% of Iso- C_4H_{10} , and 0.3% of SF_6).

The Thin Gap Chambers (TGC) are trigger chambers mounted in two concentric rings in the end-cap region. They cover the pseudorapidity range $1.05 < |\eta| < 2.4$. They are multi-wire proportional chambers. Their wire-to-cathode distance is smaller than the wire-to-wire distance. The chambers are filled

with gas mixture (CO₂ and n-C₅H₁₂).

subdetector	number of channels
pixel	~80.4 million
SCT	~6.3 million
TRT	351000
EMEC	163968
HEC	5632
FCal	3524
TileCal	9852
MDT	354000
CSC	31000
RPC	373000
TGC	318000

Table 4: Number of readout channels in the ATLAS subdetectors

3.4 Magnets

ATLAS magnet system (see Figure 16) is a unique hybrid system of four large superconducting magnets - one solenoid and three toroids (one barrel and two end-caps).

The solenoid is aligned on the beam axis and provides a 2 T axial magnetic field for the inner detector. Its design was optimised to minimise the radiative thickness in front of the barrel electromagnetic calorimeter. The total mass is 5.7 ton.

The barrel toroid produces a toroidal magnetic field of approximately 0.5 T in the central region surrounding the calorimeters and both end-cap toroids. It consists of eight coils. The total mass is 830 tonnes.

The end-cap toroids produce a toroidal magnetic field of approximately 1 T in the end-cap regions. Their purpose is to optimize the bending power in the end-cap region of the muon spectrometer system. Each toroid is made of eight coils. The total mass of each end-cap toroid is 239 tonnes.

3.5 Forward detectors

To provide good coverage in the very forward region, three smaller sets of detectors were built. The closest to the interaction point is LUCID (LUminosity measurement using Cerenkov Integrating Detector). Next is ZDC (Zero-Degree Calorimeter). The most remote detector is ALFA (Absolute Luminosity For ATLAS). Location of forward detectors is shown on Figure 20.

LUCID is the main relative luminosity monitor in ATLAS and is located at a distance of ± 17 m from the interaction point (one in each end-cap). It detects inelastic p-p scattering in the forward direction, in order to both measure the integrated luminosity and to provide online monitoring of the instantaneous luminosity and beam conditions. It is based on the principle that the number of interactions in a bunch-crossing is proportional to the number of particles detected in this detector. This holds true even when most of the detected particles originate from secondary interactions. The detector consists of mechanically polished aluminium tubes which surround the beam-pipe and point toward the interaction point. The tubes are placed in a light-weight aluminium gas vessel and filled with C₄F₁₀. The Cerenkov light emitted by a particle traversing the tube is measured by photomultiplier tubes (PMT's).

ZDC is located at a distance of ± 140 m from the interaction point. It is embedded between the beam-pipes. Its primary purpose is to detect forward neutrons ($|\eta| > 8.3$) in heavy-ion collisions. From

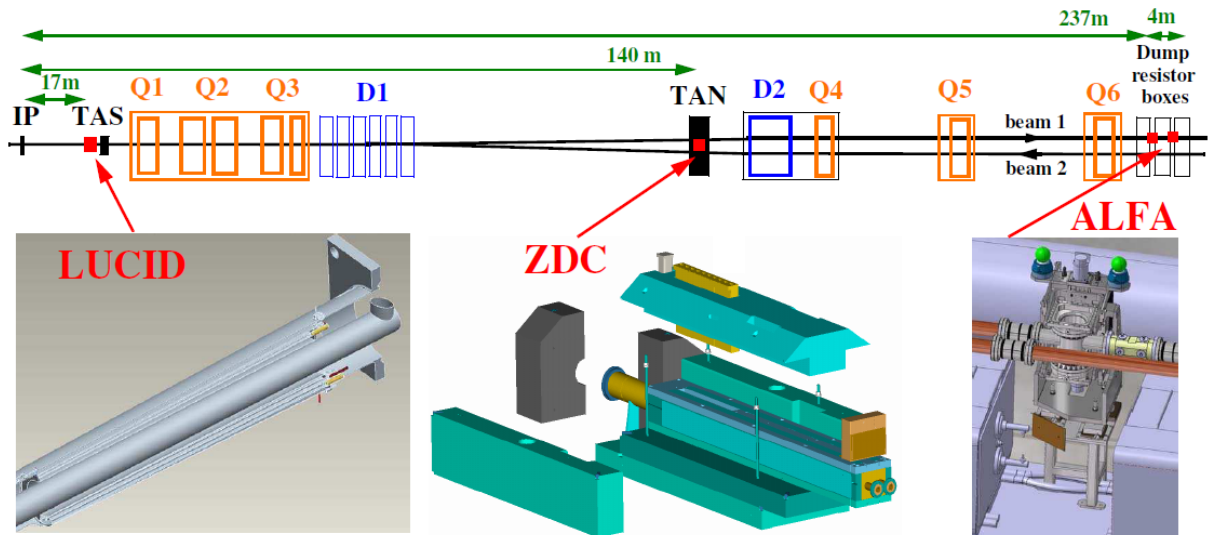


Figure 20: Location of forward detectors with respect to the interaction point (IP)

these measurements, centrality of heavy-ion collisions can be determined. There are two kinds of ZDC modules - electromagnetic and hadronic. The electromagnetic module consists of tungsten plates, with their faces perpendicular to the beam direction. Quartz rods penetrate the tungsten plates parallel to the beam. The rods are read out by multi-anode phototubes capturing the Cerenkov light from shower products of incident particles. The hadronic modules are similar, but they have different rods-onto-phototube mapping than the electromagnetic modules.

ALFA is the absolute luminosity detector. It determines absolute luminosity via elastic scattering at small angles. It consists of scintillating-fibre trackers located inside Roman pots at a distance of approximately ± 240 m from the interaction point (on each side there will be two Roman-pot stations separated by four metres). The Roman-pot concept is based upon a detector volume (the pot) that is separated from the vacuum of the accelerator by a thin window but is connected with bellows to the beam-pipe and thus can be moved close to the beam. The square fibres are read out by multi-anode phototubes.

3.6 Trigger and data acquisition

The trigger consists of three levels of event selection: Level-1 (L1), Level-2 (L2), and the event filter (EF). The L2 and EF together form the High-Level Trigger (HLT). The L1 trigger searches for events with large missing transverse energy (E_T^{miss}) and large total transverse energy and events with high- p_T muons, electrons/photons, jets, and τ -leptons decaying into hadrons. The data acquisition system also provides for the configuration, control and monitoring of the ATLAS detector during data-taking. Supervision of the detector hardware is provided by the Detector Control System (DCS).

L1 trigger uses reduced-granularity information from a subsets of detectors. It performs the initial event selection based on information from the calorimeters and muon detectors. High- p_T muons are triggered by RPC and TGC. Electromagnetic clusters, jets, τ -leptons, E_T^{miss} , and large total transverse energy are triggered by calorimeters. The maximum L1 accept rate is 75 kHz. The L1 accept decision is made by the Central Trigger Processor (CTP). It combines the information for different object types. The L1 trigger decision is based only on the multiplicity of trigger objects but information about the geometric location of trigger objects is retained in the muon and calorimeter trigger processors. If the event is accepted by L1 then this geometric information is sent as RoI's to the L2 trigger. Another essential function of the L1 trigger is unambiguous identification of the bunch-crossing.

Calorimeter trigger (L1Calo) work with about 7000 analogue trigger towers of reduced granularity from the electromagnetic and hadronic calorimeters. It is located off-detector in the service cavern. It digitises the analogue input signals and associate them with specific bunch-crossings. Then it produces the transverse-energy values using look-up table. After that electron/photon and τ -lepton candidates with E_T above the corresponding threshold and jets are identified (isolation criteria can be added). These informations are then send to CTP. If L1 accepts CTP decision then data are read out to the data acquisition system.

Muon trigger is based on dedicated finely segmented detectors with three trigger stations in both the barrel and the end-cap regions. The basic principle of the algorithm is to require a coincidence of hits in the different trigger stations within a road, which tracks the path of a muon from the interaction point through the detector. The width of the road is related to the p_T threshold to be applied. There are six thresholds in total - three low- p_T and three high- p_T ones.

In the HLT, the trigger decisions are refined by use of the full granularity and precision of calorimeter and muon chamber data and inner detector data. At the L1 trigger rate, the data acquisition system (DAQ) receives and buffers the event data from the detector-specific readout electronics. Readout Links (ROL's) perform the transmission of any data requested by the trigger to the L2 trigger. If the event does not fulfil any of the L2 selection criteria, event data are expunged. If event fulfil L2 selection criteria, event data are collected and event is built. The full event structure is sent to the event filter for further analysis. The event filter, in addition to the selection, classifies the selected events according to a predetermined set of event streams and the result of this classification is added to the event structure. The events not fulfilling any of the event filter selection criteria are expunged from the system. Events fulfilling event filter selection criteria are stored in local file system according to the classification performed by the event filter. The event files are subsequently transferred to CERN's central data-recording facility. The local storage can store all events up to 24 hour (in case there is failure in the transmission of data to CERN's central data recording service).

L2 trigger is seeded by Regions-of-Interest (RoI's). Coordinates, energy, and type of signatures from RoI's are used to limit the amount of data which must be transferred from the detector readout. When the RoI information from the different sources within the L1 trigger is received, they are merged into a single data structure. The physics selection is performed on this structure. A list of physics signatures (trigger chains), implemented event reconstruction (feature extraction) and selection algorithms are used to build signature and sequence tables for all HLT steps. The decision to reject the event or continue is based on the validity of signatures. The results of the L2 trigger's analysis are built into the final event and subsequently used by the event filter to seed its selection. The L2 trigger event rate is 3.5 kHz.

The event filter uses offline analysis procedures on fully-built events which are then recorded for subsequent offline analysis. It is a processing farm. Here tasks based on standard ATLAS event reconstruction and analysis applications receive and process events. For those events passing the selection criteria, a subset of the data generated during the event analysis is appended to the event data structure, enabling subsequent offline analysis to be seeded by the results from the event filter. During the selection process, events are classified according to the ATLAS physics streams and a tag is added to the event data structure identifying into which physics stream the event has been classified. The event filter event rate is approximately 200 Hz.

3.7 ATLAS Distributed Computing

The data recorded by the experiment needs to be stored (during Run 1 ATLAS accumulated 8 PB of RAW data) and processed [28]. ATLAS uses the Worldwide LHC Computing Grid (WLCG) and several compute cloud technologies to process data. The grid and cloud resources are spread over more than 130 computing sites distributed worldwide. The grid computing sites host over 140 PB of storage. They are very heterogenous - there are various disk and tape storage systems, CPU architectures, etc. ATLAS

grid sites are organized within three different flavors of grid: EGI (European Grid Infrastructure), OSG (Open Science Grid), and NeIC (Nordic e-Infrastructure Collaboration).

ATLAS Distributed Computing (ADC) [29] is implementing the specific aspects of ATLAS computing model on the top of WLCG baseline services. Some of the achievements of the framework are:

The workload management system managed to execute up to 1.5 M jobs/day filling in peak periods all available CPU resources and even resources beyond pledge (reaching 200 kCPU cores simultaneously occupied) for many consecutive days. The data management system was capable to deliver an aggregated traffic exceeding 10 GB/s over many days (without the loss of even a single RAW event).

4 Properties of basic objects

4.1 Photon

In this section, basic properties of the photon (its triggers, reconstruction, calibration, and identification) will be described [30], [31].

In the following, all photons produced in pp collisions and that are not originating from hadron decays are considered as “prompt.” They include “direct” photons, which originate from the hard processes calculable in perturbative QCD, and “fragmentation” photons, which are the result of the fragmentation of a coloured high- p_T parton [17].

4.1.1 Photon trigger

Overall structure of the ATLAS experiment trigger system is described in Section 3.6. The photon selection starts at L1. The electromagnetic calorimeter cluster is retained if the transverse energy of the photon passes a threshold. The transverse energy threshold is specified by the trigger menu. If the event is accepted by L1, it is passed to L2 which is seeded by L1 cluster position. Full granularity data is available here. The cluster seed finding step is using the most energetic cell in the second EM layer (EF is using the sliding window algorithm). The EF selects from the initial collection of photon candidates corresponding to energy clusters in the electromagnetic calorimeter at the trigger level. It discriminates isolated photons from jets with a large electromagnetic component.

4.1.2 Photon reconstruction

The reconstruction photons starts from energy deposits (clusters) in the electromagnetic calorimeter. The calorimeter is divided into grid of $N_\eta \times N_\phi$. Then towers of size $\Delta_\eta \times \Delta_\phi = 0.025 \times 0.025$ are created. Inside each of these elements, the energy of all cells in all longitudinal layers is summed into the tower energy. The clusters are seeded by towers with total transverse energy above 2.5 GeV and searched for by a sliding-window algorithm, with a window size of 3×5 towers.

The clusters without track matching to a well-reconstructed ID track are classified as unconverted photons. The clusters with matching track consistent with originating from a photon conversion and with reconstructed conversion vertex are considered converted photons. They are classified as single-track or double-track conversions depending on the number of assigned electron-tracks. Then the clusters are rebuild using an area of calorimeter cells corresponding to 3×7 for converted photons and 3×5 for unconverted photons in the barrel. In the end-caps, size 5×5 is used for both converted and unconverted photons.

4.1.3 Photon calibration

The energy of photon candidate is built from the energy of a cluster of cells in the EM calorimeter. The EM cluster properties are calibrated to the original photon energy in simulated Monte Carlo samples using multivariate techniques. The MC-based e/γ response calibration is applied to the cluster energies reconstructed both from collision data and MC simulated samples. Then more corrections are implemented and the response in data is calibrated so that it agrees with the expectation from simulation, using a large sample of $Z \rightarrow ee$ events. The calibrated energy is validated on $J/\psi \rightarrow e^+e^-$ events in data. This calibration is valid in E_T range between 10 GeV and 1 TeV [32].

There is a difference observed in the shower shape variables which can be parametrised as a simple shift. These shifts (a.k.a. fudge factors [33]) are computed as the difference between the means of a given variable in data and Monte Carlo. These corrections are then applied to events from Monte Carlo samples.

4.1.4 Cuts for photon identification

For good separation between isolated photons and fake signatures from QCD jets, the baseline photon identification algorithms rely on rectangular cuts using calorimetric variable. There are several categories of variables used for photon identification cuts:

- Acceptance - $|\eta| < 2.37$, $1.37 < |\eta| < 1.52$ excluded
- Hadronic leakage
 - R_{had_1} - ratio of E_T in the first sampling of the hadronic calorimeter to E_T of the EM cluster (used over the range $|\eta| < 0.8$ and $|\eta| > 1.37$)
 - R_{had} - ratio of E_T in all the hadronic calorimeter to E_T of the EM cluster (used over the range $0.8 < |\eta| < 1.37$)
- EM Middle layer
 - R_η - ratio in η of cell energies in 3×7 versus 7×7 cells
 - w_2 - lateral width of the shower
 - R_ϕ - ratio in ϕ of cell energies in 3×3 and 3×7 cells
- EM Strip layer
 - w_{s3} - shower width for three strips around maximum strip
 - $w_{s\text{ tot}}$ - total lateral shower width
 - F_{side} - fraction of energy outside core of three central strips but within seven strips
 - ΔE - difference between the energy associated with the second maximum in the strip layer, and the energy reconstructed in the strip with the minimal value found between the first and second maxima
 - E_{ratio} - ratio of the energy difference associated with the largest and second largest energy deposits over the sum of these energies

There are two sets of cuts - loose and tight. The tight cut is using all of above mentioned variables. The loose cut is using only following variables: R_{had} , R_{had_1} , R_η , and w_2 . Both loose and tight cut values are optimized in $|\eta|$ bins. Tight cuts are separately optimized for unconverted and converted photon candidates.

In the loose selection, photons share a common set of loose cuts and cut thresholds with electrons. These variables show relatively small differences for unconverted and converted photons. The values of the cuts are optimized for nine different $|\eta|$ regions to respect the `g20_loose` trigger rate requirements.

In the tight selection, variables used for loose selection have tighter cuts. Also, additional variables are used. As a consequence, photon candidates are required to lie in the pseudorapidity region covered by the finely segmented part of the first layer of the electromagnetic calorimeter. Thus, photon candidates in the regions $1.37 < |\eta| < 1.52$ (in the data collected in 2012, the crack region location was increased to $1.37 < |\eta| < 1.56$ (see [27])) and $|\eta| > 2.37$ are rejected. Tight selection requirements are also optimized to provide good rejection of isolated leading π^0 s. The tight cuts are separately optimized for unconverted and converted photon candidates. Tight cuts have been optimized for each of the seven pseudorapidity regions covered by the strip layer - there are 14 independent optimizations, 7 for converted photons and 7 for unconverted photons.

4.1.5 Photon isolation

The isolation energy [34] is designed to distinguish direct photons (i.e. produced in the hard process) from fake or non-direct (i.e. produced in hadron decays) photons coming from jets. It is estimated by collecting the energy deposited in a cone around the photon candidate. Direct photons do not have deposits in the cone (there are only low-energy objects coming from the underlying event, multiple interactions and pile-up collisions). Fakes and non-direct candidates have some additional (potentially large) energy coming from the accompanying objects in the jet.

The isolation variable is built from topological clusters. The cells belonging to the cluster are used to calculate signal to noise energy ratios. The topological cluster is built using the ratios. The final isolation variable is constructed by summing the transverse energy of clusters with positive energy whose barycenters fall into the isolation cone. A rectangle of $\Delta\eta \times \Delta\phi = 5 \times 7$ electromagnetic calorimeter cells centered on the photon candidate is removed (in order to subtract photon's energy) itself.

Several corrections to the variable are applied:

- leakage correction:
Most of the energy of the photon candidate shower is contained in the 5×7 cluster centered on the cluster. But as the energy of the photon increases, the shower leaks outside the 5×7 cluster. A correction is applied in order not to include this energy in the isolation energy.
- underlying event and pile-up corrections:
The isolation variable is also corrected for the energy deposits from the underlying events or additional proton-proton interactions (on an event by event basis)

4.2 Jet

Collimated sprays of energetic hadrons, called jets, are the dominant feature of high energy hard proton-proton interactions. They are observed as groups of topologically related energy deposits in the ATLAS calorimeters reconstructed using anti- k_t algorithm (see Section 4.2.1). Then the jets are calibrated using Monte Carlo in a way that average jet energy corresponds to that of the associated stable particles in the ATLAS detector (see Section 4.2.2).

4.2.1 anti- k_t clustering algorithm

In the anti- k_t algorithm [35], the distances between entities are defined as follows:

- distance between entities (particles, pseudojets) i and j - d_{ij}

$$d_{ij} = \min(k_{ti}^{2p}, k_{tj}^{2p}) \frac{\Delta_{ij}^2}{R^2}$$

where k_{ti} is transverse momentum of particle i , R is radius of jet, and $\Delta_{ij}^2 = (y_i - y_j)^2 + (\phi_i - \phi_j)^2$

- distance between entity i and the beam (B) - d_{iB}

$$d_{iB} = k_{ti}^{2p}$$

Depending on the value of p , different algorithms can be recovered: for $p = 1$, it is the k_t algorithm; for $p = 0$, it is the Cambridge/Aachen algorithm; and for $p = -1$ it is the anti- k_t algorithm.

The behaviour arise from the aforementioned formulas, e.g. by considering an event with a few well-separated hard particles with transverse momenta k_{t1}, k_{t2}, \dots and many soft particles. The soft particles

will tend to cluster with hard ones long before they cluster among themselves. If a hard particle has no hard neighbours within a distance $2R$, then it will simply accumulate all the soft particles within a circle of radius R , resulting in a perfectly conical jet. If there is another hard particle such that $R < \Delta_{12} < 2R$ then there will be two hard jets. For this case, there can be either one conical jet and one partly conical (if $k_{t1} \gg k_{t2}$) or both cones will be clipped (if $k_{t1} \sim k_{t2}$). And if $\Delta_{12} < R$, both particles will cluster to form one jet.

Input to calorimeter jets which are found by anti- k_t algorithm are topological calorimeter clusters (topo-clusters) [36]. Topological clusters are groups of calorimeter cells that are designed to follow the shower development. The topo-cluster formation algorithm starts from a seed cell. Such cell has signal-to-noise (S/N) ratio (estimated as the absolute value of the energy deposited in the calorimeter cell over the RMS of the energy distribution measured in randomly triggered events without proton-proton collisions) above a threshold $S/N=4$. Cells neighbouring the seed that have a signal-to-noise ratio of at least $S/N = 2$ are included iteratively. Finally, all calorimeter cells neighbouring the formed topo-cluster are added. The topo-cluster algorithm efficiently suppresses the calorimeter noise.

4.2.2 Jet calibration

The calibration [36] scheme starts from the measured calorimeter energy which is deposited by electromagnetic and hadronic showers. Then the jet Lorentz four-momentum is reconstructed from the corrected energy and angles with respect to the primary event vertex. Jets with transverse momentum $p_T > 20$ GeV and pseudorapidity $|\eta| < 4.5$ are calibrated. The jet calibration corrects for the following detector effects:

- calorimeter non-compensation (partial measurement of the energy deposited by hadrons)
- dead material (energy losses in inactive regions of the detector)
- leakage (energy of particles reaching outside the calorimeters)
- out of calorimeter jet cone (energy deposits of particles inside the truth jet entering the detector that are not included in the reconstructed jet)
- noise thresholds and particle reconstruction efficiency (signal losses in the calorimeter clustering and jet reconstruction)

The scheme which is currently used is Global Sequential Calibration (GSC). First, jet calibration is derived as a simple correction - the calibrated jet energy is measured jet energy divided by calibration function that depends on the measured jet energy. Then, it exploits the topology of the energy deposits in the calorimeter to characterise fluctuations in the jet particle content of the hadronic shower development.

4.2.3 Jet background

The main background of the jets from collisions [37] are:

- Beam-gas events, where one proton of the beam collided with the residual gas within the beam pipe.
- Beam-halo events, for example caused by interactions in the tertiary collimators in the beam-line far away from the ATLAS detector.
- Cosmic ray muons overlapping in-time with collision events.
- Calorimeter noise.

4.2.4 Removal of non-collision background

Calorimeter electronics noise can lead to fake energy deposits. They can be reconstructed as fake jets. Pulse in calorimeter cells caused by particle showering is characteristic and can be distinguished from noise using Q_{cell}^{LAr} variable. This variable is defined as quadratic difference between the actual and expected (from simulation) pulse shape. Several jet level quantities can be derived from it:

$\langle Q \rangle$ = average jet quality. It is the energy squared weighted average of the pulse quality of the calorimeter cells (Q_{cell}^{LAr}) in the jet. This quantity is normalized such that $0 < \langle Q \rangle < 1$.

f_Q^{LAr} = Fraction of the energy in LAr calorimeter cells with poor signal shape quality ($Q_{cell}^{LAr} > 4000$).

f_Q^{HEC} = Fraction of the energy in HEC (hadronic end-caps) calorimeter cells with poor signal shape quality ($Q_{cell}^{LAr} > 4000$).

There are two types of calorimeter noise. First, sporadic noise bursts in HEC where a few noisy calorimeter cells contribute to almost all of the jet energy. Jets reconstructed from these problematic cells are characterized by a large energy fraction in the HEC (f_{HEC}) as well as a large $\langle Q \rangle$ and large f_Q^{HEC} and its neighbouring cells will have an apparent negative energy (E_{neg}). Second, coherent noise in the electromagnetic calorimeter. Jets reconstructed from this source are characterized by a large electromagnetic energy fraction (f_{EM}), defined as the ratio of the energy deposited in the electromagnetic (EM) calorimeter to the total energy, large $\langle Q \rangle$ and large f_Q^{LAr} .

Another sources of non-collision background are cosmic rays and beam-induced background. They also produce energy deposits which are not arising from proton-proton collisions. These backgrounds can be discriminated using electromagnetic energy fraction (f_{EM}) and the maximum energy fraction in any single calorimeter layer (f_{max}). For jets within the tracking acceptance, jet charged fraction (f_{ch}) (the ratio of the scalar sum of the p_T of the tracks associated to the jet divided by p_T^{jet}) is used. And finally, for jets which are not in time with the beam collision, the jet time (t_{jet}) (the weighted average of the time of the energy deposits in the jet, weighted by the square of the cell energies) is used.

4.2.5 Jet quality selection

The intention of selection criteria is to efficiently reject jets from background processes while keeping the highest efficiency selection for jets. Jets candidates are reconstructed using the anti- k_r clustering algorithm with a distance parameter $R=0.4$. The inputs to this algorithm are topologically connected clusters of calorimeter cells (topo-cluster). Jet candidates arising as high energy objects produced in collisions are called “good jets” while jet candidates coming from the background are called “fake jets”.

For the quality selection, there are four sets of criteria: “Looser”, “Loose”, “Medium”, and “Tight”. The “Looser” selection was designed to provide an efficiency above 99.8 % with as high a fake jet rejection as possible while the “Tight” selection was designed to provide a much higher fake jet rejection with an inefficiency not larger than a few percent.

To be more specific, the “Looser” set is to avoid the following effects using following conditions:

$$\begin{aligned}
 \text{HEC spikes:} & \quad (f_{HEC} > 0.5 \text{ and } |f_Q^{HEC}| > 0.5 \text{ and } \langle Q \rangle > 0.8) \text{ or } E_{neg} > 60 \text{ GeV} \\
 \text{Coherent EM noise:} & \quad (f_{EM} > 0.95 \text{ and } |f_Q^{LAr}| > 0.8 \text{ and } \langle Q \rangle > 0.8 \text{ and } |\eta| < 2.8) \\
 \text{Non-collision background:} & \quad (f_{max} > 0.99 \text{ and } |\eta| < 2) \text{ or } (f_{EM} < 0.05 \text{ and } |f_{ch}| < 0.05 \text{ and } |\eta| < 2) \\
 & \quad \text{or } (f_{EM} < 0.05 \text{ and } |\eta| \geq 2)
 \end{aligned}$$

4.3 b-tagging in the ATLAS experiment

4.3.1 Introduction

The b-tagging is the ability to identify jets containing b-hadrons. It is important for several physics programmes, e.g. selection of very pure top samples, SM Higgs study, SUSY Higgs study, veto of $t\bar{t}$ background for several physics channels and for searching for new physics: SUSY decay chains, heavy gauge bosons, etc. Most of these studies requires good b-tagging performance for jets with transverse momentum from 20 to 150 GeV but some requires the b-tagging for jets up to a few TeV. This subsection is a review from [38], pages 398-431.

The properties of the b-jet allow us to distinguish them from light quark jets. First, the fragmentation is hard and the b-hadron retains about 70 % of the original b quark momentum. Second, high mass of the b-hadrons (> 5 GeV) implies that decay products may have a large transverse momentum with respect to the jet axis and the opening angle of the decay products is large enough to allow separation. Finally, the b-hadrons have relatively long lifetime and therefore will have a significant flight path length (a b-hadron in a jet with $p_T = 50$ GeV travels on average about 3 mm in the transverse plane before decaying). The tracks from b-hadron decay products also tend to have rather large impact parameters. The transverse impact parameter d_0 is defined as the distance of closest approach of the track to the primary vertex point, in the $r-\varphi$ projection (r is radius and φ is azimuthal angle). The longitudinal impact parameter z_0 is the z coordinate of the track at the point of closest approach in $r-\varphi$. Their geometrical meaning is illustrated on Figure 21.

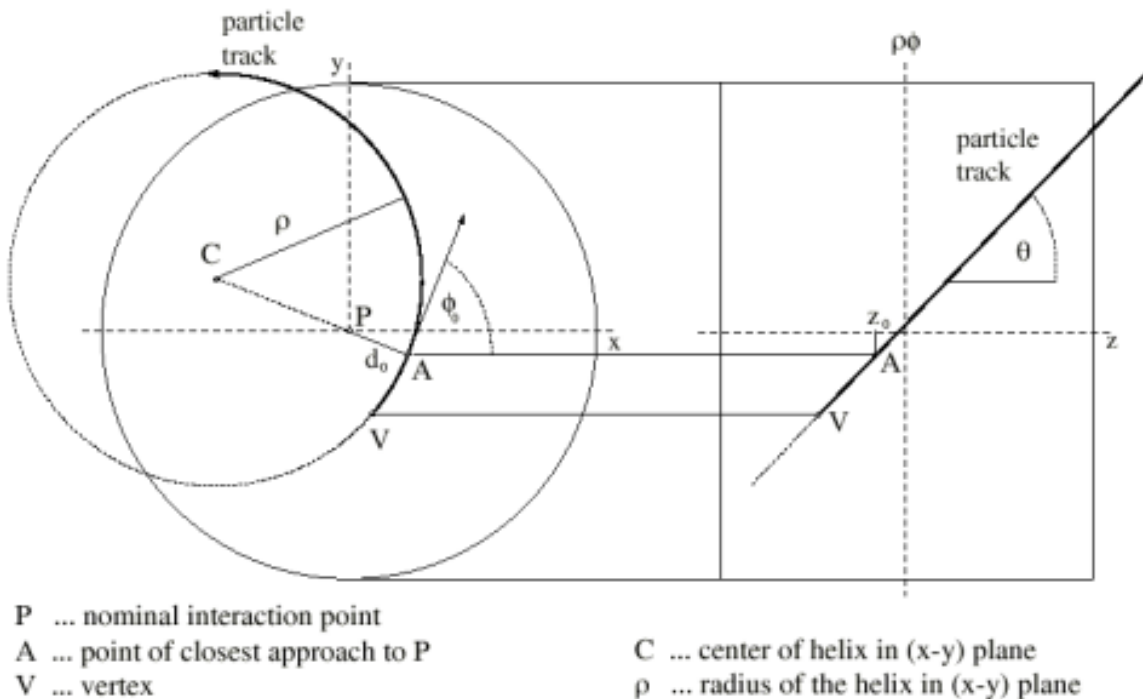


Figure 21: The illustrative drawing of the meaning of the transverse and the longitudinal impact parameter. Figure from [39].

Also the leptons from the semi-leptonic decays of b-hadron can be used for b-tagging. The lepton will have relatively large transverse momentum and large momentum relative to the jet axis because of the hard fragmentation and high mass of b-hadrons.

4.3.2 Reconstruction of the key objects

Several key objects are required for the b-tagging. Their reconstruction is briefly described in this subsection.

The charged tracks for b-tagging are reconstructed mainly in the Inner Detector. Average track consists of 3 pixel hits, 4 space-points in the SCT and about 36 hits in the TRT. The innermost pixel layer is called b-layer. The tracker measures efficiently and with good accuracy the tracks within $|\eta| < 2.5$ and down to $p_T \sim 500$ MeV. The track selection is designed to find well-measured tracks and reject fake tracks (the fake rate is defined as the fraction of reconstructed tracks which do not pass the matching criteria used for the efficiency, i.e. less than 80 % of their hits are coming from the same Monte Carlo particle), tracks from long-lived particles (impact parameter resolution is crucial for discrimination of tracks coming from long-lived hadrons and prompt tracks) and material interactions. The track selection uses two quality levels: the standard quality level and the b-tagging quality level. The standard quality level has the following properties:

- at least seven precision hits (hits in pixels or SCT),
- transverse impact parameters at the perigee must fulfil $|d_0| < 2$ mm,
- longitudinal impact parameters at the perigee must fulfil $|z_0 - z_{pv}| \sin \theta < 10$ mm (z_{pv} is the longitudinal location of the primary vertex),
- transverse momentum of tracks is $p_T > 1$ GeV.

For the b-tagging quality level, there are the extra requirements :

- at least two hits in the pixel detector of which one must be in the b-layer,
- $|d_0| < 1$ mm,
- $|z_0 - z_{pv}| \sin \theta < 1.5$ mm.

The tracking efficiency has a great influence on the b-tagging. The tracking performance deteriorates at high pseudorapidities mostly because of increased amount of material and more ambiguous measurements. It also degrades near the core of the jet where the track density is the highest and induces pattern-recognition problems. The tracks with shared hits have also influence on the b-tagging. The tracks with shared hits are the tracks which are sharing some of their hits with other tracks. For the b-tagging purposes, a track is defined as a track with shared hits if it has at least one shared hit in the pixels or two shared hits in the SCT. The fraction of tracks with shared hits increases with the local track density. Therefore, it is higher for high- p_T jets and in the core of the jets. The impact parameter significances (defined as ratio d_0/σ_{d_0} and z_0/σ_{z_0} of the impact parameter to its measured error) for tracks in light jets exhibit a very different behaviour depending on whether the track is a regular one or a track with shared hits.

Primary vertex finding is another key ingredient for the b-tagging. The impact parameters of tracks are recomputed with respect to the primary vertex position. The tracks compatible with the primary vertex are excluded from the secondary vertex searches. The efficiency to find the primary vertex is very high in the high- p_T events of interest. The pile-up and the presence of additional minimum bias vertices makes the choice of the primary vertex less trivial.

Several jet algorithms are used for the b-tagging. The baseline jet algorithm is the seeded cone algorithm using the calorimeter towers with a cone size of $\Delta R = 0.4$. For the b-tagging purposes, only the jet direction is relevant because the direction is used to define which tracks should be associated with the jets. Currently tracks within a distance $\Delta R < 0.4$ of the jet axis are associated to the jet. A given track is associated to only one jet (the closest in ΔR). Only the taggable jets are used for the b-tagging. They have the following properties:

- $p_T > 15 \text{ GeV}$
- $|\eta| < 2.5$.

Soft lepton reconstruction is important for the soft lepton tagging because leptons from semi-leptonic decays of b(c)-hadrons can be used to tag b-jets. Soft muons are reconstructed using two complementary reconstruction algorithms. A combined muon corresponds to a track fully reconstructed in the Muon Spectrometer that matches a track in the Inner Detector. Low-momentum muons (below $p \sim 5 \text{ GeV}$) cannot reach the muon middle and outer stations. They are identified by matching an Inner Detector track with a segment in the Muon Spectrometer inner stations. Soft electrons are reconstructed in the Inner Detector and the Electromagnetic Calorimeter. Reconstruction is achieved by matching an inner detector track to an electromagnetic cluster. The performance is depending on the track density in jets and the quantity of matter in front of the electromagnetic calorimeter.

4.3.3 b-tagging algorithms

Various algorithms are used to tag b-jets in the ATLAS Experiment. The spatial b-tagging algorithms are using the impact parameters of tracks or reconstructed the secondary vertex. The soft lepton tagging algorithms are using leptons from the semi-leptonic decays of b(c)-hadrons.

The spatial algorithms based on likelihood ratio are using jets in which all tracks are fulfilling the b-tagging quality cuts as defined in Section 4.3.2. In the likelihood ratio method, the measured value S_i of a discriminating variable is compared to pre-defined smoothed and normalized distributions for both the b- and light jet hypotheses, $b(S_i)$ and $u(S_i)$. Some tagging algorithms also use two- and three-dimensional probability density functions. The track or vertex weight is defined by the ratio $\frac{b(S_i)}{u(S_i)}$. These weights can be combined into the jet weight W_{jet}

$$W_{jet} = \sum_{i=1}^{N_T} \ln W_i = \sum_{i=1}^{N_T} \ln \frac{b(S_i)}{u(S_i)}$$

where N_T is the number of individual track. To select b-jets, a cut value on W_{jet} must be chosen corresponding to a given efficiency. The relation between the cut value and the efficiency depends on the jet transverse momentum and rapidity. In case the track categories are used, the jet weight W_{jet} is defined as

$$W_{jet} = \sum_{j=1}^{N_C} \sum_{i=1}^{N_T^j} \ln \frac{b_j(S_i)}{u_j(S_i)}$$

where N_C is the number of categories. In the current b-tagging software, two track categories are used: the Shared tracks (tracks with shared hits), and the complementary subset of tracks called Good tracks. These track categories are only used for the time being for the IP1D, IP2D and IP3D tagging algorithms. The algorithms need to reject V^0 and secondary interactions first. The preselection cuts on impact parameters cause rejection of a large fraction of long-lived particles and secondary interactions. From remaining tracks, tracks which are likely to come from V^0 decays are rejected. To achieve this rejection, all two-track pairs that form a good vertex are built. The mass of the vertex is used to reject the tracks which are likely to come from K_S , Λ and photon conversions. The radius of the vertex is compared to a crude description of the b-layer to reject secondary interactions in material. The tagging itself starts by computing the impact parameters of tracks with respect to the primary vertex. Then the impact parameter is signed. The sign of the transverse impact parameter d_0 is defined as

$$\text{sign}(d_0) = \left(\vec{P}_j \times \vec{P}_t \right) \cdot \left(\vec{P}_t \times \left(\vec{X}_{pv} - \vec{X}_t \right) \right)$$

where \vec{P}_j is the jet direction, \vec{P}_t is direction of the track at the point of closest approach to the primary vertex, \vec{X}_{pv} is position of the primary vertex and \vec{X}_t is position of the track at the point of closest approach to the primary vertex. For the tracks originating from the primary vertex, the experimental resolution generates a random sign but tracks from the b(c) hadron decay tend to have a positive sign. The sign of the longitudinal impact parameter z_0 is given by the sign of

$$(\eta_j - \eta_t) \times z_0,$$

where subscript t refers to quantities defined at the point of closest approach to the primary vertex and subscript j refers to jet. The meaning of the impact parameters signs is that the transverse (d_0) and longitudinal (z_0) impact parameters of tracks are computed with respect to the primary vertex and are signed positively if the track crosses the jet axis in front of the primary vertex and negatively otherwise [40]. There are three tagging algorithms using the impact parameter significances of all the tracks in the jet - IP1D uses the longitudinal impact parameter, IP2D the transverse impact parameter and IP3D two-dimensional histograms of the longitudinal versus transverse impact parameters. Secondary vertex tagging algorithms are used to further improve the b-tagging performance. They can increase the discrimination between light jets and b-jets. The search for the secondary vertex starts by building all two-track pairs that form a good vertex. Only tracks far enough from the primary vertex, i.e. $L_{3D}/\sigma_{L_{3D}} > 2$ where $L_{3D} \equiv \|\vec{X}_{pv} - \vec{X}_t\|$ is the three dimensional distance between the primary vertex and the point of closest approach of the track to this vertex, are used. Vertices compatible with a V^0 or material interaction are rejected. All tracks from the remaining two-track vertices are combined into a single inclusive vertex. An iterative procedure removes the worst tracks until the χ^2 of the vertex fit is good. The secondary vertex (SV) tagging algorithms uses three vertex properties: the invariant mass of all tracks associated to the vertex, the ratio of the sum of the energies of the tracks participating to the vertex to the sum of the energies of all tracks in the jet and the number of two-track vertices. SV1 uses a 2D-distribution of the two first variables and a 1D-distribution of the number of two-track vertices. SV2 uses a 3D-histogram of the three properties. There is also algorithm called JetFitter. JetFitter exploits the topological structure of weak b- and c-hadron decays inside the jet. The discrimination between b(c) and light jets is based on a likelihood using similar variables to the SV tagging algorithm.

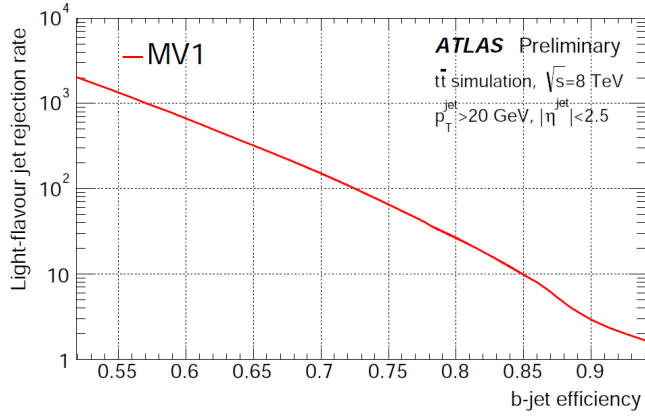
The IP3D+SV1 algorithm is created by combining tagging algorithms. Only the likelihood-based tagging algorithms have been combined because in this formalism, the weights of the individual tagging algorithms are simply summed up. Another combined algorithm is IP3D+JetFitter. The SV tagging algorithms have been optimized to work in conjunction with the IP ones.

4.3.4 MultiVariate tagging algorithm

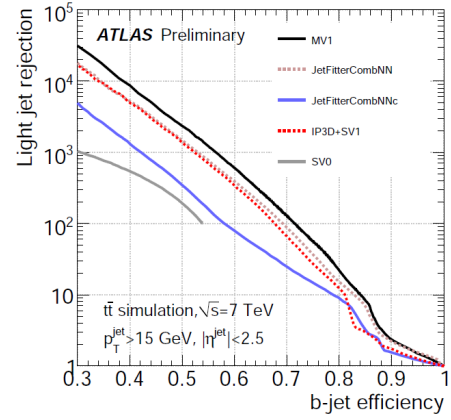
The MV1 algorithm [41] is b-tagging algorithm currently used by the ATLAS Collaboration because it is best performing validated b-tagging algorithm (see Figure 22b). It is using the most discriminating variables from IP3D, SV1, and JetFitter algorithms. They are combined in artificial neural networks. MV1 is trained with b jets as signal and light-flavour jets as background, and computes a tag weight for each jet.

Fixed cuts, called working points or operating point, can be applied to tag weight distribution to obtain specified b-jet efficiencies. The performance of the MV1 algorithm has been calibrated at working points corresponding to efficiencies of 60%, 70% and 80%.

The calibration results are provided as data/MC scale factors.



(a) light jet rejection efficiency as a function of b-tagging efficiency for MV1 tagger at $\sqrt{s}=8$ TeV[42]



(b) light jet rejection efficiency as a function of b-tagging efficiency for advanced b-tagging algorithms at $\sqrt{s}=7$ TeV[41]

Figure 22: Light jet rejection efficiency as a function of b-tagging efficiency

5 Data and MC samples

Information about datasets used for analysis is provided in this section. More detailed specification (dataset names, number of events, cross-sections, and filtering efficiencies including) is summarized in Appendix A.

5.1 Data samples

The data sample used in this analysis represents data collected by the ATLAS experiment in the year 2012 (see Figure 23). All data distributions in the analysis are scaled by $1/\text{luminosity}$.

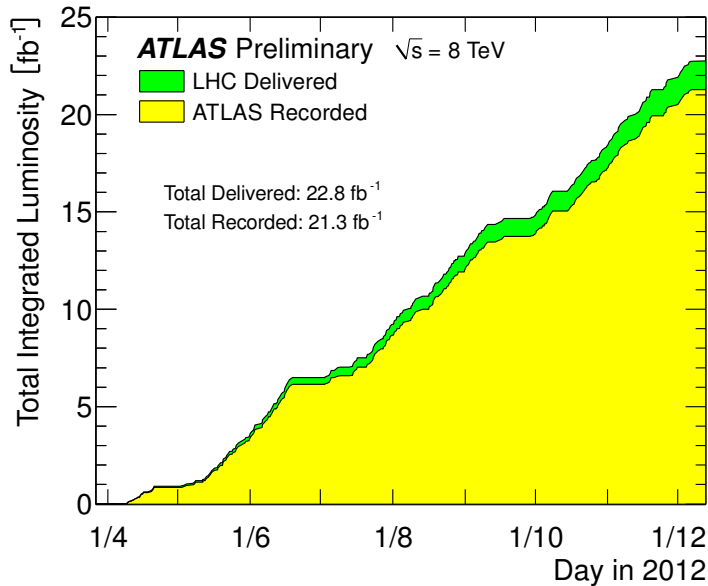


Figure 23: Delivered and recorded luminosity [43]

5.2 Monte Carlo generator level samples

PyTHIA 8 [44] represents a complete rewrite of PyTHIA [45] from Fortran to C++. As such it is not yet tested and tuned enough to have reached the same level of maturity as Pythia 6. Currently the program only works with pp , $p\bar{p}$, e^+e^- and $\mu^+\mu^-$ incoming beams. Much of the physics aspects are unchanged relative to the Pythia 6.4 (with the exception of the Supersymmetry and Technicolor sectors which have not been implemented yet). The initial- and final-state algorithms are based on the new p_T -ordered evolution. Hadronisation is based solely on the Lund string fragmentation framework. The events are generated as follows: a hard process is generated first. After that, all subsequent activity (initial- and final-state radiation, multiple parton-parton interactions and the structure of beam remnants) on partonic level is generated. The parton configuration is hadronized by string fragmentation followed by the decays of unstable particles. The samples contain jet+jet (scatterings of quarks and gluons) and gamma+jet (Compton-QCD and quark-antiquark annihilation producing direct photon and gluon) events with at least one hard process or parton shower photon with $p_T > 17, 35, 70, 140, 280, 500$ and 800 GeV. The reconstructed photon spectra are biased by the generator and filter cuts close to the threshold. Thus, E_T of photon (reconstructed or true) should be sufficiently higher than threshold. Correspondence between sample threshold and photon transverse momentum range is shown in Figure 24 and Table 5.

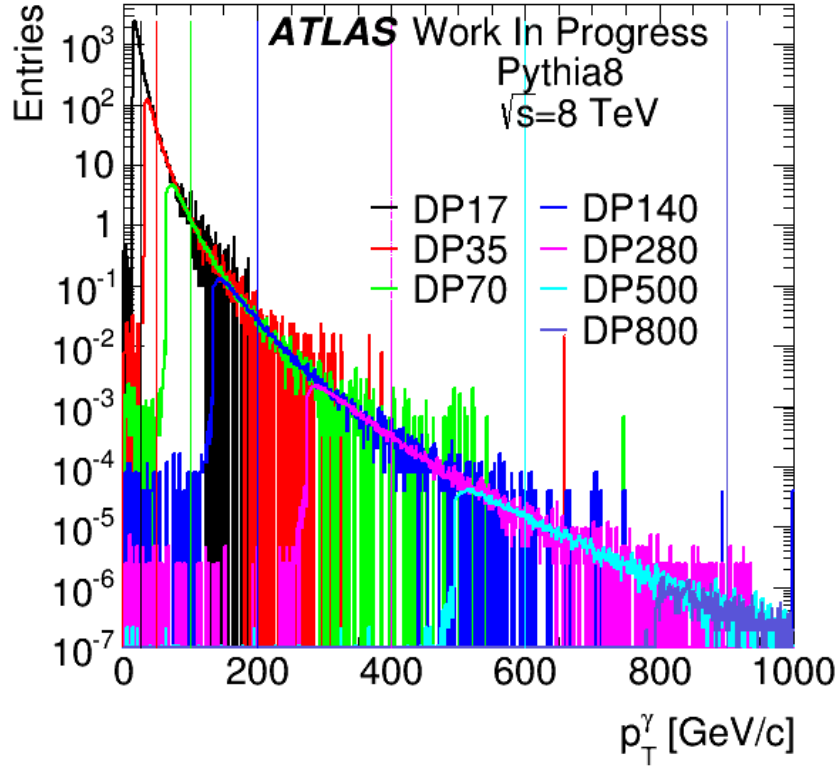


Figure 24: p_T^γ distribution of photon used for analysis in Monte Carlo generator level samples. Vertical lines indicate the range of validity (where the given sample is used) - the color of the line means the sample the beginning of the range where the sample is used. The next line means the beginning of the next sample which is the end of range where current sample is used

p_T^γ range [GeV]	sample threshold [GeV]
(25, 50)	17
(50, 100)	35
(100, 200)	70
(200, 400)	140
(400, 600)	280
(600, 900)	500
(900, 1000)	800

Table 5: Transverse momentum range of photon used for analysis for particular Monte Carlo generator level sample

All distribution using Monte Carlo generator level samples are scaled by $\frac{\sigma\varepsilon}{N}$, where σ is total cross-section of given sample, ε is filtering efficiency of given sample, and N number of events in given sample

5.3 Monte Carlo reconstruction level samples

Following samples were created from subset of samples described in Section 5.2. The evgen samples are part of ATLAS simulation infrastructure [46]. Particles from evgen events are propagated through the ATLAS detector using GEANT4 [47],[48]. Hits (i.e. energy deposits in the sensitive parts of the detector) are created in this step. In the next step, hits are transformed into digits (detector responses; they serve as input to the detector electronics). In the final step, program emulates read out and physical object (photons, jets, etc.) are reconstructed in the same way as for the real data.

As these datasets were created from generator level samples, they also contain jet+jet and gamma+jet events with at least one hard process or parton shower photon with $p_T > 17, 35, 70, 140, 280, 500$ and 800 GeV. Correspondence between sample threshold and photon transverse momentum range is shown in Figure 25 and Table 6.

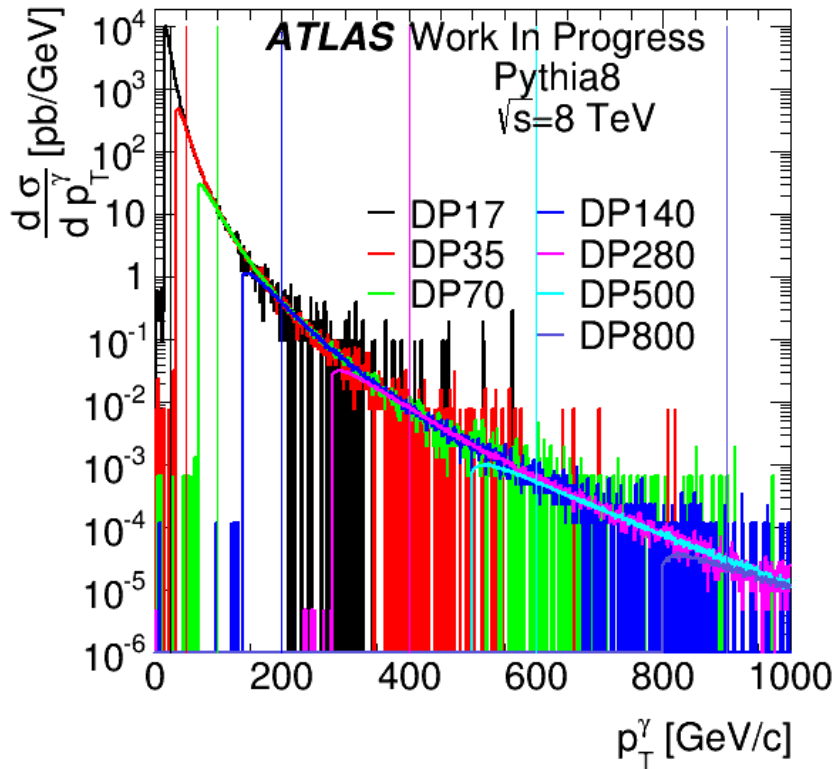


Figure 25: p_T^γ distribution of leading truth photons. Vertical lines indicate the range of validity (where the given sample is used) - the color of the line means the sample the beginning of the range where the sample is used. The next line means the beginning of the next sample which is the end of range where current sample is used

All distribution using Monte Carlo reconstruction level samples are scaled by $\frac{\sigma\varepsilon}{N}$, where σ is total cross-section of given sample, ε is filtering efficiency of given sample, and N number of events in given

sample.

p_T^γ range [GeV]	sample threshold [GeV]
(25, 50)	17
(50, 100)	35
(100, 200)	70
(200, 400)	140
(400, 600)	280
(600, 900)	500
(900, 1000)	800

Table 6: Transverse momentum range of photon used for analysis for particular Monte Carlo reconstruction level sample

6 Cross-section measurement

6.1 Monte Carlo

When analysing Monte Carlo samples, the differential cross-section (as a function of p_T^γ) in each p_T^γ bin is calculated as

$$\frac{d\sigma}{dp_T^\gamma} = \frac{\sigma_{tot} \times \varepsilon_f}{\Gamma_{bin} \times N_{event}} \times N(p_T^\gamma) \quad (3)$$

where

- σ_{tot} is total cross section for given dataset
- ε_f is filtering efficiency for given dataset
- N_{event} is number of all generated events for given dataset
- Γ_{bin} is a width of given p_T bin (see Section 6.3)
- $N(p_T^\gamma)$ is number of events in given p_T bin (see Section 6.3)

6.2 Data

When analysing samples of measured data, the differential cross-section (as a function of p_T^γ) in each p_T^γ bin is calculated as

$$\frac{d\sigma}{dp_T^\gamma} = \frac{N(p_T^\gamma) \times C}{\Gamma_{bin} \times \int Ldt} \quad (4)$$

where

- $N(p_T^\gamma)$ is number of events in given p_T bin (see Section 6.3)
- Γ_{bin} is a width of given p_T bin (see Section 6.3)
- $\int Ldt$ is integrated luminosity
- $C = \frac{N^{MC,truth}}{N^{MC,reco}}$, where $N^{MC,truth}$ is number of events at the generation level in each p_T^γ bin with $p_T^{jet} > 20$ GeV, $|\eta^{jet}| < 2.4$, $p_T^\gamma > 25$ GeV, $|\eta^\gamma| < 1.37$ or $1.56 < |\eta^\gamma| < 2.37$, and $\Delta R(\gamma - jet) > 1$ and $N^{MC,reco}$ is number of events at reconstruction level in each p_T^γ bin after event selection and background subtraction

6.3 Binning

The p_T^γ distributions were binned with variable bin size binning to reflect how number of events is changing with p_T^γ . The following binning was used for both event generation level and reconstructed level samples:

(25, 45)	(45, 65)	(65, 85)	(85, 105)	(105, 125)	(125, 150)
(150, 200)	(200, 250)	(250, 300)	(300, 400)	(400, 600)	(600, 1000)

7 Analysis of events at the generator level

Differential cross-sections as a function of transverse momentum of photon at event generation level (i.e. before simulation) are provided in this section. The analysis is performed using event record dump from ROOT files. The event record contains list of all particles in the event with detailed informations about them - for every vertex it contains list of incoming and outgoing particles with their PDG IDs (Particle Data Group ID: identifier specifying particle type in Monte Carlo; PDG IDs relevant for this analysis are in Table 7), four-momentum components, status code (code specifying history of particle in the process of interaction simulation - it enables e.g. to identify particles in final state), and their decay vertex (if it exists). Using these informations, hard scattering products can be identified and their properties analysed.

PDG ID	2212	-5	-4	-3	-2	-1	1	2	3	4	5	21	22
particle	proton	\bar{b}	\bar{c}	\bar{s}	\bar{u}	\bar{d}	d	u	s	c	b	g	γ

Table 7: PDG IDs of relevant particles

Relevant status codes are defined [49] as

- status=21: particles of the hardest subprocess - incoming
- status=23: particles of the hardest subprocess - outgoing

Events from datasets were stitched together as suggested in Section 5.2. Differential cross-section (as a function of p_T^γ) were obtained from these events (calculated using the formula 3).

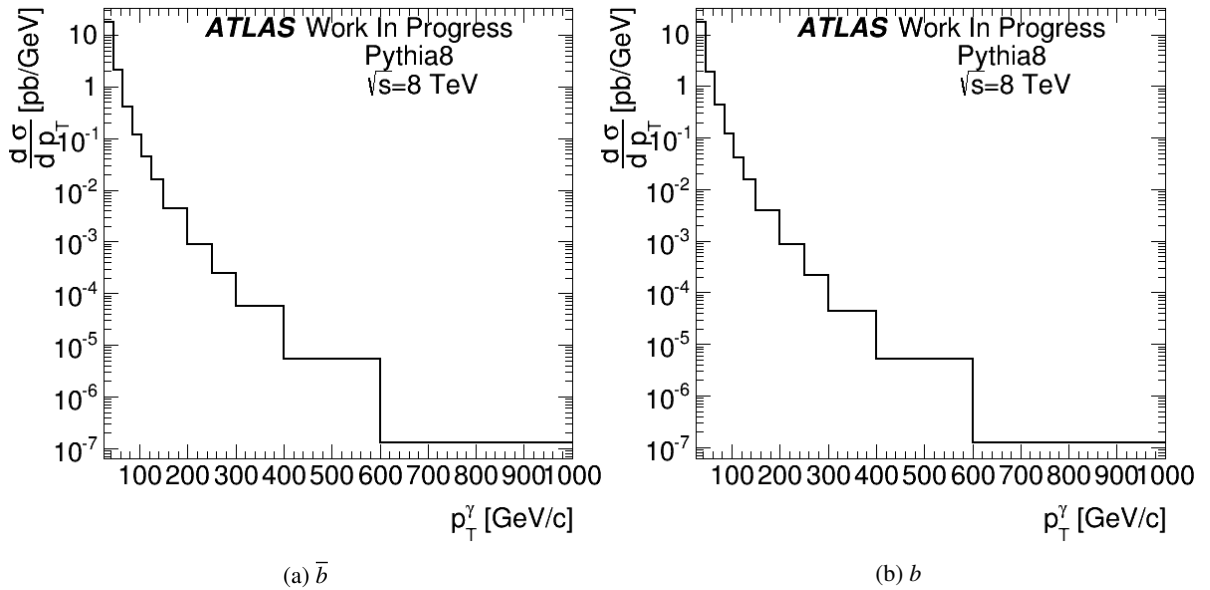


Figure 26: Cross-section of Compton-QCD for b flavoured quarks

7.1 PYTHIA 8 processes

Presented differential cross-section are created from official ATLAS datasets generated by PYTHIA 8 at energy $\sqrt{s} = 8$ TeV. For more details about samples, see Section 5.2 and Appendix B.

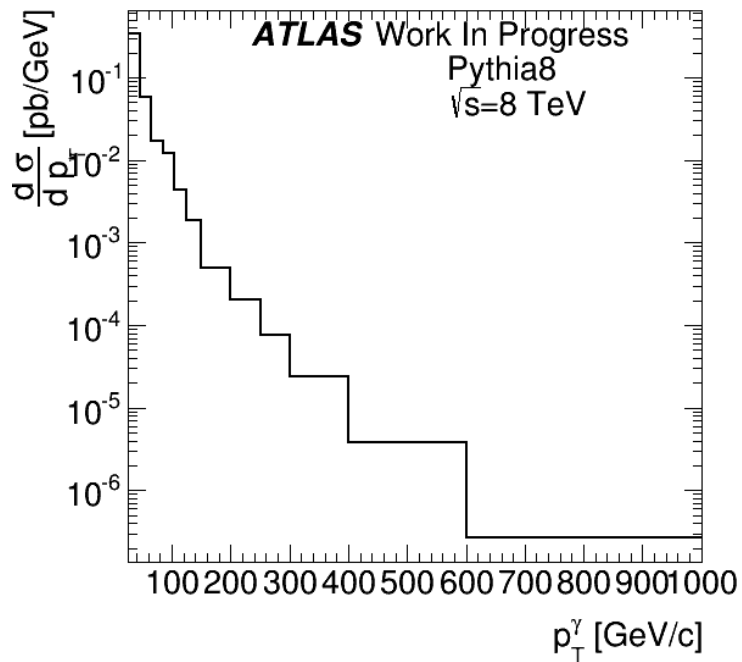


Figure 27: Cross-section of quark-antiquark annihilation for b flavoured quarks

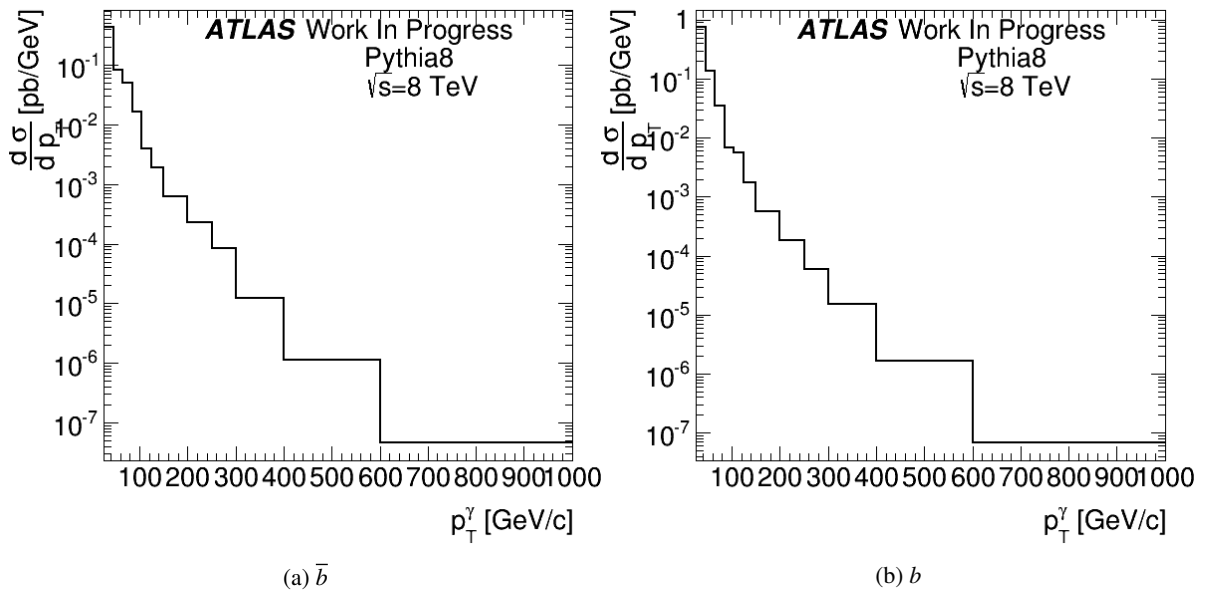


Figure 28: Cross-section of event where fragmentation photon is created with b flavoured quark

7.1.1 $Qg \rightarrow \gamma Q$

Structure of the PYTHIA 8 event on Figure 31 represents Feynman diagrams depicted on Figure 2. The event starts with two incoming protons. Hard scattering corresponds to vertex 3. Quarks and gluons with barcodes 3 and 4 are coming in the vertex. Photon and b (or \bar{b}) quark with barcode 5 and 6 are going out of the vertex.

Figure 26 shows differential cross-section of processes $\bar{b}g \rightarrow \gamma\bar{b}$ and $bg \rightarrow \gamma b$

7.1.2 $q\bar{q} \rightarrow \gamma g, g \rightarrow Q\bar{Q}$

Structure of the PYTHIA 8 event on Figure 32 represents Feynman diagrams depicted on Figure 3. The event starts with two incoming protons. Quarks and gluons with barcodes 3 and 4 are scattered in vertex 3. Photon and gluon with barcode 5 and 6 are going out of the vertex. Photon after that just changes its status. Gluon decays into $b\bar{b}$ pair.

Figure 27 shows differential cross-section of process $q\bar{q} \rightarrow \gamma g, g \rightarrow b\bar{b}$

7.1.3 $qq, gg \rightarrow Qq, q \rightarrow \gamma + X$

Structure of the PYTHIA 8 event on Figure 33 represents Feynman diagrams depicted on Figure 6. The event starts with two incoming protons. Quarks with barcodes 3 and 4 enter the vertex 3. One b (or \bar{b}) quark goes out. The other particle is quark of any flavour which decays into several particles including photon.

Figure 28 shows differential cross-section of processes $qq, gg \rightarrow \bar{b}q, q \rightarrow \gamma + X$ and $qq, gg \rightarrow bq, q \rightarrow \gamma + X$

7.1.4 $qg \rightarrow qq, q \rightarrow \gamma + X, g \rightarrow Q\bar{Q}$

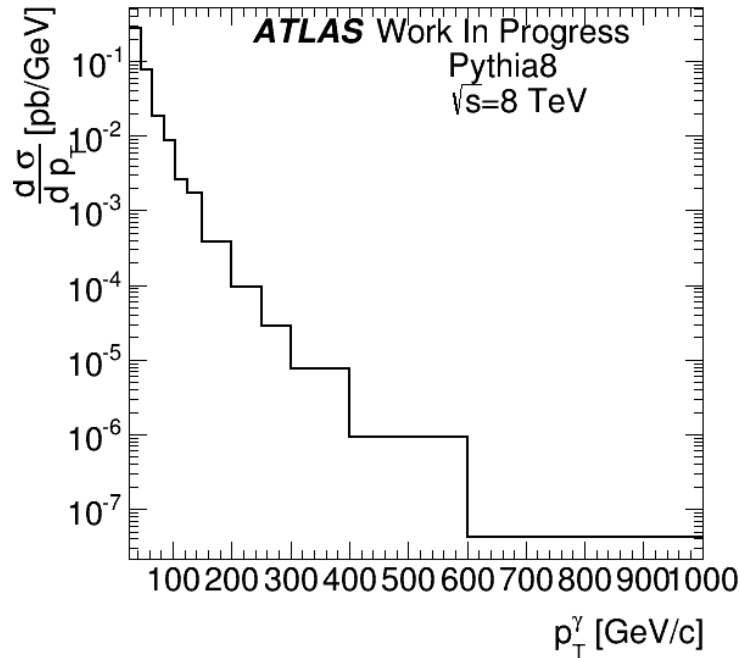


Figure 29: Cross-section of event where fragmentation photon is created with $b\bar{b}$ pair

Structure of the PYTHIA 8 event on Figure 34 represents Feynman diagrams depicted on Figure 5. The event starts with two incoming protons. Quarks and gluons with barcodes 3 and 4 interact in the vertex 3. One particle going out of the vertex is gluon which is decaying into $b\bar{b}$ pair. The other particle going out of the vertex is quark of any flavour which decays into several particles including photon.

Figure 29 shows differential cross-section of process $qg \rightarrow qg, q \rightarrow \gamma + X, g \rightarrow b\bar{b}$.

The resulting cross-section of all these processes combined is on Figure 30.

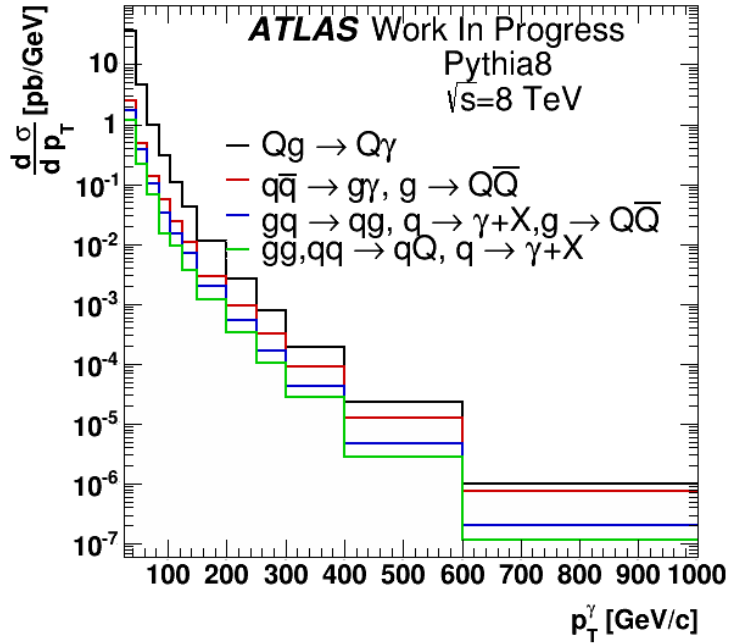


Figure 30: Combined cross-section of direct and fragmentation processes

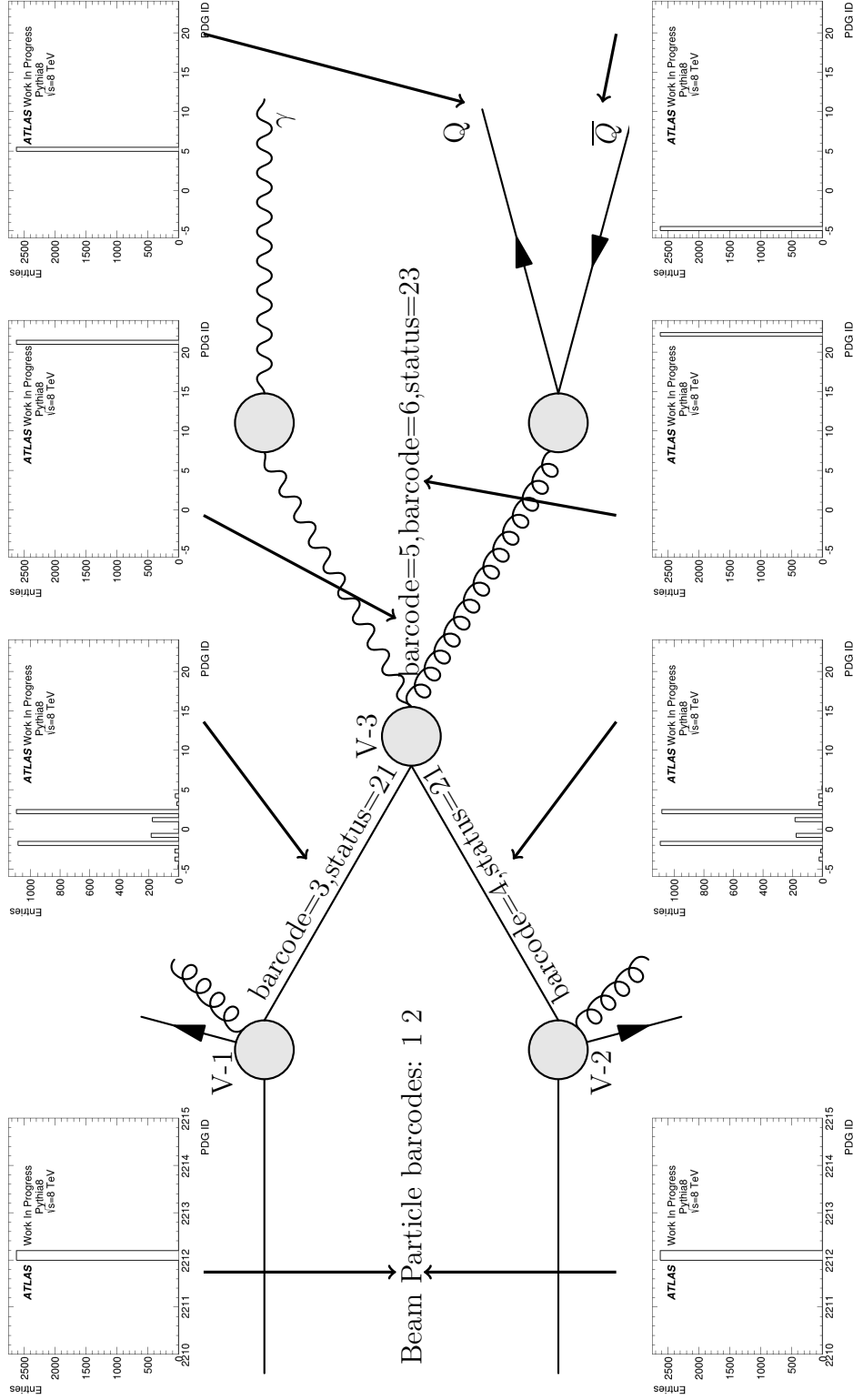


Figure 32: Event structure of the quark-antiquark annihilation. The figure in the middle represents event structure, the histograms on the edges show PDG ID of particles in the event. The incoming particles are protons (PDGID=2212). Vertex 3 is the interaction vertex. Particles coming in the vertex are quarks (PDGID \in $\{-5, 5\}$) with status 21. Particles going out of the vertex are gluon (PDGID=21) a photon (PDGID=22) with status 23. After that, photon changes status to stable particle and gluon decays into $b\bar{b}$ pair.

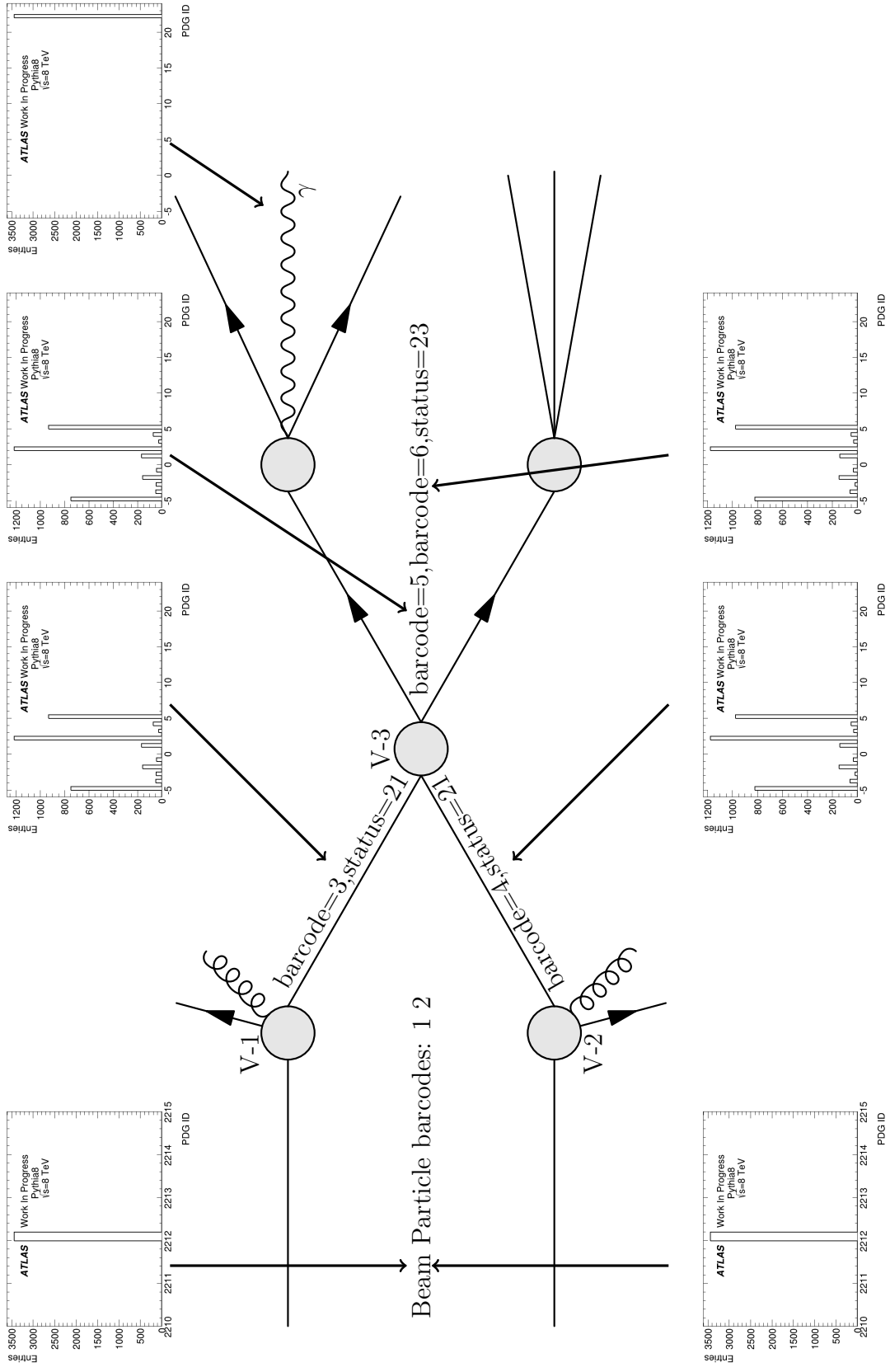


Figure 33: Event structure of event where fragmentation photon is created with b flavoured quark. The figure in the middle represents event structure, the histograms on the edges show PDG ID of particles in the event. The incoming particles are protons (PDGID=2212). Vertex 3 is the interaction vertex. Particles coming in the vertex are quarks (PDGID ∈ {−5, 5}) with status 21. Particles going out of the vertex b quark (PDGID=5) or \bar{b} quark (PDGID=−5) and another quark (PDGID ∈ {−5, 5}) with status 23. After that, quark decays into several particles including photon.

8 The event selection

This section describes selection of events based on properties of the whole events as well as leading photon and leading jet. There are many effect which are necessary to filter out to ensure sufficient quality of data collected [50].

8.1 Good Run List

The Good Run Lists (GRL) [51] are built from Data Quality (DQ) flags. Data quality flags are implemented by each of the detector systems, and also by their consecutive clients in the analysis chain (performance and/or physics groups). They are defined only for valid runs (all physics runs in the with a minimum amount of integrated luminosity (or a minimum number of events), and with no dramatic/unrecoverable DAQ failures). Several primary DQ flags are available for each system to reflect its physical segmentation (in most cases is limited to DQ flags for barrel and endcaps). They form the mechanism to ensure that the DQ assessment is applied consistently to any physics analysis.

The Good Run List (GRL) is a list of good runs/luminosity blocks based on those flags. It is formed by applying DQ flag selection criteria, and possibly other criteria, to the list of valid physics runs. From this, list of run numbers and, for each run, luminosity block ranges, is created. The list has form of XML file. Official good run lists, to be used for physics analysis and publication of physics results, are created by the Data Quality group.

The Good Run List used for this analysis is `data12_8TeV.periodAllYear_DetStatus-v61-pro14-02_DQDefects-00-01-00_PHYS_StandardGRL_All_Good`. Data available with this GRL is 20.3 fb^{-1} with corresponding uncertainty $dL/L = 3.6\%$ [50].

8.2 Incomplete events

In 2012 data-taking, the TTC (Timing, Trigger, and Control - part of L1 trigger - see Section 3.6) restart was developed to recover certain detector busy conditions without a run-restart. In the lumi-block after a TTC restart there can be incomplete events (where some detector information is missing from the event). These events are removed [52].

8.3 LAr calorimeter noise bursts and data integrity errors

Events with noise bursts and data integrity errors in the LAr calorimeter [53] needs to be removed.

8.4 Tile calorimeter event corruption

A handful of Tile corrupted events should be rejected [52].

8.5 Tile calorimeter trips

Tile Calorimeter has suffered from frequent module trips [54]. These trips are considered a tolerable data quality defect as the energy in an unpowered module is extrapolated from its neighbours (the trip is accounted for during offline reconstruction). Events with several consecutive unpowered (or not recording) tile modules are marked with an intolerable defect and rejected by the GoodRunsList (see Section 8.1). Also, events containing data corruption from one particular tile channel are rejected.

8.6 Primary vertex

Every event is required to have at least one reconstructed primary vertex with more than two tracks associated to it.

8.7 Jet acceptance

Jet acceptance is chosen in a way that jet can be detected and further processed.

- jet pseudorapidity range: $|\eta| < 2.4$
- jet momentum cut $p_T > 20$ GeV

8.8 Jet cleaning

Jet cleaning [55] at "looser" level as described in Section 4.2.5 is used.

8.9 Jet hot cell cleaning

In the data taking period B1 and B2 there was a hot Tile calorimeter cell that had not been masked in the reconstruction. A jet is removed if it points to the (η, ϕ) region close to LBC28 ($\eta = -0.15, \phi = 2.7$), if this jet has its highest energy fraction in the Tile second layer and this fraction is large.

8.10 Jet BCH cleaning

There are modules which are either temporarily or permanently masked throughout all data taking periods. In data taken in 2012, one module was off for the full dataset. Therefore it was added into a Monte Carlo samples. It turns out that the correction which was used to correct for masked cells within the tile calorimeter was not able to properly handle entire dead modules. This affects especially high- p_T jets as they are more collimated and thus can be more completely contained within masked modules. The jets in these regions are poorly reconstructed. Therefore, events where the jet falls into a masked region is removed

8.11 Photon trigger

Some basic overview of photon trigger is in Section 4.1.1. In 2012 data, several single photon triggers were defined. Table 8 displays the chains from L1 to EF level with EF level threshold. Triggered photons are required to pass the loose selection (see Section 4.1.4). The primary unrescaled single photon trigger is g120_loose [56].

Threshold [GeV]	L1 trigger	L2 trigger	EF trigger
20	L1_EM12	L2_g20_loose	EF_g20_loose
40	L1_EM30	L2_g40_loose	EF_g40_loose
60	L1_EM30	L2_g60_loose	EF_g60_loose
80	L1_EM30	L2_g80_loose	EF_g80_loose
100	L1_EM30	L2_g100_loose	EF_g100_loose
120	L1_EM30	L2_g120_loose	EF_g120_loose

Table 8: Single photon trigger chains

8.11.1 Trigger matching

The matching procedure [57] is to ensure that offline photon (photon after final stage of processing) matches to an object passing the trigger. The procedure starts with an offline photon. Then it loops over the trigger object passing given trigger and checking the distance between the offline photon and trigger objects. If the distance of the offline photon to the closest of the trigger objects is less than 0.15 then it is considered as matched.

8.11.2 Trigger prescales

Prescale factor N means only 1 in N events is selected and passed to the HLT for further consideration [38]. Prescales reduce trigger output rate for given stage (trigger chain or item).

Physics trigger prescale [58] is defined as

$$\text{prescale} = (\text{L1 prescale}) \times (\text{L2 prescale}) \times (\text{EF prescale}) \quad (5)$$

Structure of trigger chains is in Table 8. Prescales for each individual trigger level can be found in TrigConfTree in metadata of files. First, following prescale keys are read from physics tree: trig_DB_HLTPSK, trig_DB_L1PSK, and trig_DB_SMK. Then HLTPSK, L1PSK, and SMK prescale keys are read from TrigConfTree. The keys for each level are matched between trees - this also matches event from physics tree to “event” from TrigConfTree. Then, prescales for given event and trigger name are read from TrigConfTree. Using these individual prescales, the total prescale for event is calculated using formula 5.

8.12 Photon acceptance

Photon acceptance is chosen in a way that jet can be detected and further processed.

- photon pseudorapidity range: $|\eta| < 1.37$, $1.56 < |\eta| < 2.37$
- photon momentum cut $p_T > 25$ GeV

8.13 Photon object quality

Object Quality Maps [59] are used to check the quality of the egamma object. The photon is defined as bad if its cluster is affected (Affected cells = cells affected by minor problems: low noise, distorted signal, unstable noise, calibration issues) by the presence of a dead FEB (Front-End Board in the LAr calorimeter) in the first or second sampling layer or by the presence of a dead HV region affecting the three sampling layers or by the presence of a masked cell (Masked cells=cells whose energy is put at zero. They are high noise cells, dead cells and sporadic cells with $Q > 4000$) in the core or in case one of the 8 central strips is masked (since shower shape variables based on the strips, used in photon identification, could be affected). These bad photons are removed.

8.14 Photon cleaning

Photon cleaning removes clusters with large amount of energy from bad cells by requiring:

$$\frac{\sum_{\text{cluster}} E_{\text{cell}}(Q > 4000)}{\sum_{\text{cluster}} E_{\text{cell}}} > 0.8 \quad (6)$$

This cut is combined with a shower shape cut to reject only very narrow fake candidates and also with a timing cut to reject out-of-time candidates. Q is defined in Section 4.2.4.

8.15 Ambiguity resolver

Usage of electron/photon Ambiguity Resolver in association with the standard tight photon selection has been shown to reduce the fraction of electron misidentified as photon by about 1/3.

8.16 Jet b-tagging

B-tagging means the ability to identify jets containing b-hadrons. Details on b-tagging algorithms are in Section 4.3. The MV1 tagging algorithm is currently preferred algorithm in ATLAS. Operation point [60] for MV1 b-tagging efficiencies are defined as follows:

MV1 efficiency	MV1 operating point
80%	0.3511
70%	0.7892
60%	0.9827

Table 9: MV1 algorithm operating points

Operating point can be chosen with the help of Figure 22a. It shows that with decreasing b-tagging efficiency, light jet rejection is increasing. So, the operating point is chosen in a way that it suppresses as many light jets as possible while keeping b-tagging efficiency (and therefore number of b jets) high enough. The numbers are in the Table 10. For 80 % efficiency, the light jet rejection is not high enough and there are several times more light jets than b jets. For 60 % efficiency, the light jet rejection is good but the number of b jets dropped by one third. As a compromise, 70 % operating point is used. The operating points are derived for jets satisfying a JVF > 0.5 cut (for more information about JVF, see Section 8.20).

MV1 efficiency	Number of b jets	Number of c jets	Number of light jets
80%	26622	45298	60320
70%	22319	25488	12358
60%	18260	14461	3036

Table 10: Number of b, c, and light jets in Monte Carlo samples for each MV1 efficiency

8.17 Distance of photon and jet

Distance of leading photon and leading jet is set to be greater than one. As the photon isolation (see Section 9.1) is done in a cone with radius of 0.4 and jet is reconstructed using anti- k_t algorithm, it seems that it would be sufficient to set the distance to 0.8. But sometimes the jet can be wider than 0.4 and thus affecting photon isolation. So, when plotting the isolation efficiency as a function of distance between leading jet and leading photon (see Figure 35), one can see that the distribution reaches a plateau around one.

8.18 Duplicate events

Also, there are very rare DAQ problems which can lead to the same physics event being written out more than once [61]. This can be checked by looking for duplicate pairs of the event number and run number. The resulting sample after event selection was checked and no duplicate events were found.

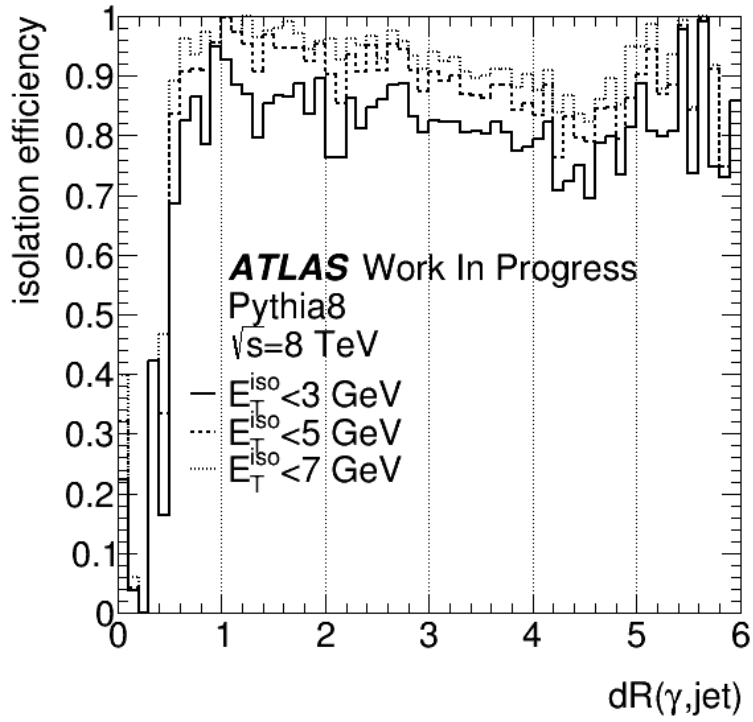


Figure 35: Isolation efficiency as a function of distance of leading photon and leading jet for three isolation energies - 3, 5, and 7 GeV

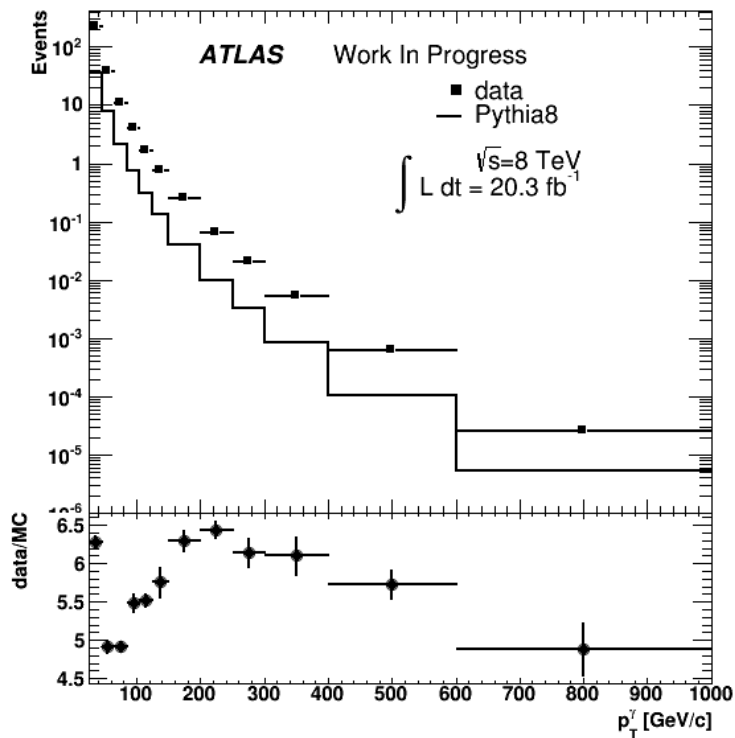


Figure 36: Comparison of p_T^γ distribution in data and Monte Carlo after event selection. Errors are statistical only.

8.19 The event selection overview

This section describes results of event selection. The distribution of p_T^γ in data and Monte Carlo is shown on Figure 37 with information about statistical uncertainty. Figure 36 compares these distributions. The Table 11 gives detailed information about number of events with each level of event filtering.

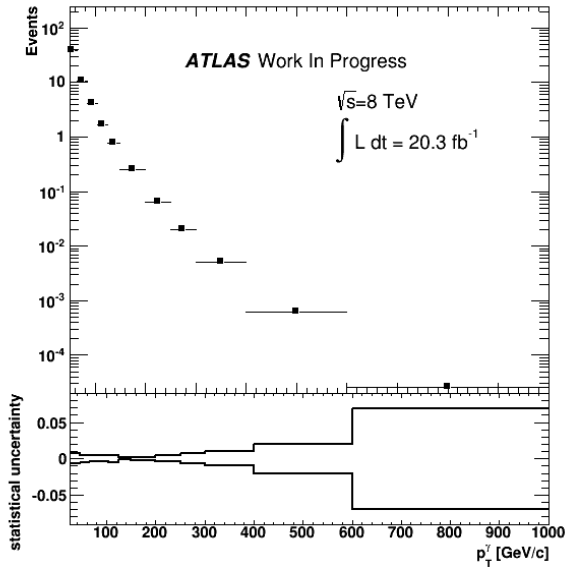
	number of events in data
all events	731415197
events with at least one photon and at least one jet	728900572
using GoodRunsList	696640289
incomplete events removed	696640011
events with at least one reconstructed PV with more than two tracks	696638871
LAr noise bursts and data integrity errors removed	695214177
Tile calorimeter corrupted events removed	695214125
Tile calorimeter trips removed	695214117
events with leading jet in acceptance	499856958
events after jet cleaning	499755298
events after jet hot cell cleaning	499755293
events after jet BCH cleaning	499755181
events passing photon trigger	25008907
events with leading photon in acceptance	22805247
events after photon object quality cleaning	22609241
events after photon cleaning	22608740
events after photon ambiguity is resolved	22450742
events with jets tagged by MV1 algorithm at 70% efficiency	1031762
events with distance of leading photon and leading jet greater than one	977548

Table 11: Number of events per event selection level

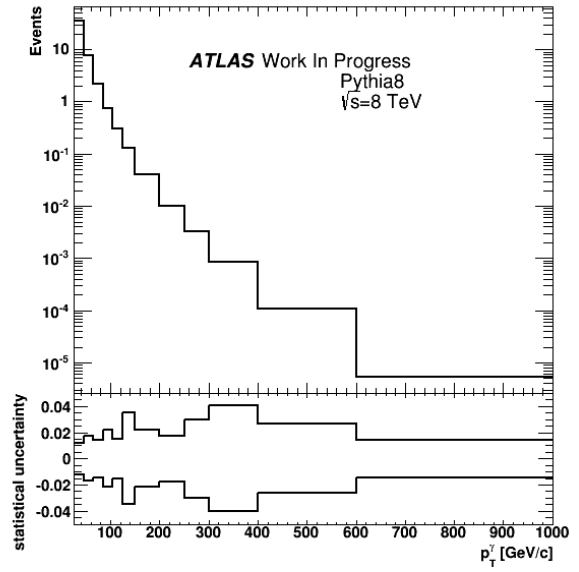
8.20 Pile-up reweighting

Pile-up [62] means detection of additional interactions to the one which is used for measurement. There are two kinds of pile-up. In-time pile-up means additional interactions in the same bunch crossing as the triggered event which are producing additional signals. Out-of-time pile-up means multiple interactions from surrounding bunch crossings causing signal modulation (enabled by LHC bunch spacing of 50 ns). The corrections were developed [63] which are applied on event-by-event basis.

The Monte Carlo datasets (see Section 5.3) belong to mc12c production campaign [64]. It means that it used updated, realistic beam spot information and pile-up profile and improved geometry description created after stop of data taking. As a result, shape of number of primary vertices (NPV) distribution without pile-up reweighting is fairly close in data and Monte Carlo (see Figure 38). So, even though agreement after reweighting is a little bit closer, it is a small effect.

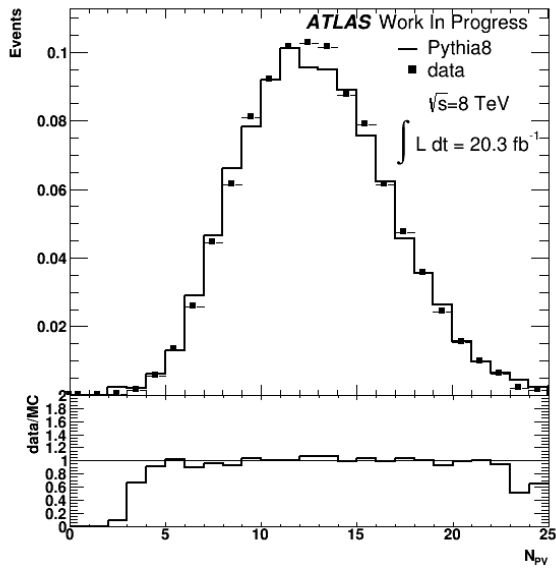


(a) data

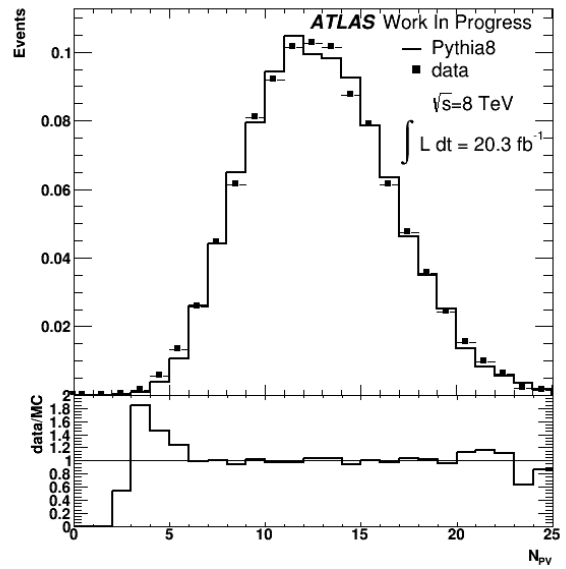


(b) Monte Carlo

Figure 37: p_T^γ distribution in data and Monte Carlo after event selection with statistical uncertainty distributions.



(a) before pile-up reweighting



(b) after pile-up reweighting

Figure 38: Number of primary vertices (NPV) distribution in data and Monte Carlo before and after pile-up reweighting. The distributions are normalized to one.

The jet vertex fraction (JVF) is a variable used to identify the origin vertex of a given jet. It means JVF can help filter jets coming from additional proton-proton collisions in the event. JVF is defined for each jet with respect to each identified primary vertex (PV) in the event. Tracks associated to calorimeter jets are used to calculate JVF. The calculation is using the following formula

$$JVF(\text{jet}_i, \text{PV}_j) = \frac{\sum_k p_T(\text{track}_k^{\text{jet}_i}, \text{PV}_j)}{\sum_n \sum_l p_T(\text{track}_l^{\text{jet}_i}, \text{PV}_n)} \quad (7)$$

i.e. JVF is the ratio of the sum of transverse momentum of matched tracks that originate from a chosen primary vertex to the sum of transverse momentum of all matched tracks in the jet, independently of their origin. In the formula 7 k runs over all tracks originating from PV_j matched to jet_i , n over all primary vertices in the event and l over all tracks originating from PV_n matched to jet_i .

Studies were performed in different topologies. They have shown that 99% of pile-up jets with $p_T > 20$ GeV has $p_T < 50$ GeV. So, it is not necessary to apply this cut to jets with $p_T < 50$ GeV. Also, to avoid a loss in signal efficiency, it is recommended to apply the JVF cut only to jets with $|\eta| < 2.4$.

9 Background subtraction

There are two major backgrounds in the γ +b jet measurement. First one is background from hadronic jets containing π^0 mesons affecting prompt photons. The other one are processes producing γ +c jet and γ +light jet affecting b jets. This section describes ways to subtract these backgrounds

9.1 Photon isolation

Photon isolation energy (E_T^{iso}) (see Section 4.1.5) is used in 2D sideband method. Unfortunately, isolation efficiency (see Figure 39) shows p_T^γ dependence and declines at higher p_T^γ . To counter that, it was decided to use p_T^γ -dependent isolation.

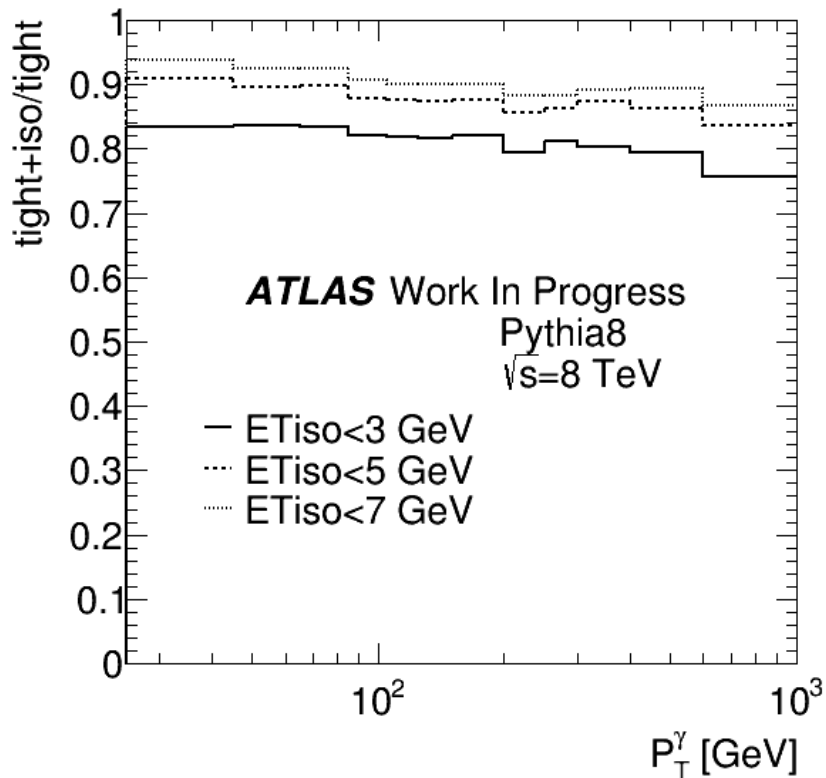


Figure 39: Isolation efficiency for energies 3, 5, and 7 GeV

The isolation function is found based on 5 GeV isolation (which is considered a baseline). Basically, it means to apply 5 GeV cut at low p_T^γ and at high p_T^γ apply cut with the same isolation efficiency. The procedure is simple - for given small range of isolation efficiency (corresponding to $E_T^{iso} \approx 5$ GeV), photon isolation energies are found for all p_T^γ bins. And this distribution is fitted with linear function $A p_T^\gamma + B$. The result is $A = 4.8 \pm 0.9 \times 10^{-3}$ and $B = 4.8 \pm 0.3$. The isolation efficiency using this p_T^γ -dependent isolation is on Figure 40. The photons with isolation energy $E_T^{iso} < A p_T^\gamma + B$ are considered isolated. The photons with isolation energy $E_T^{iso} > A p_T^\gamma + B + 2$ are considered non-isolated (the 2 GeV margin is added for uncertainty evaluation reasons).

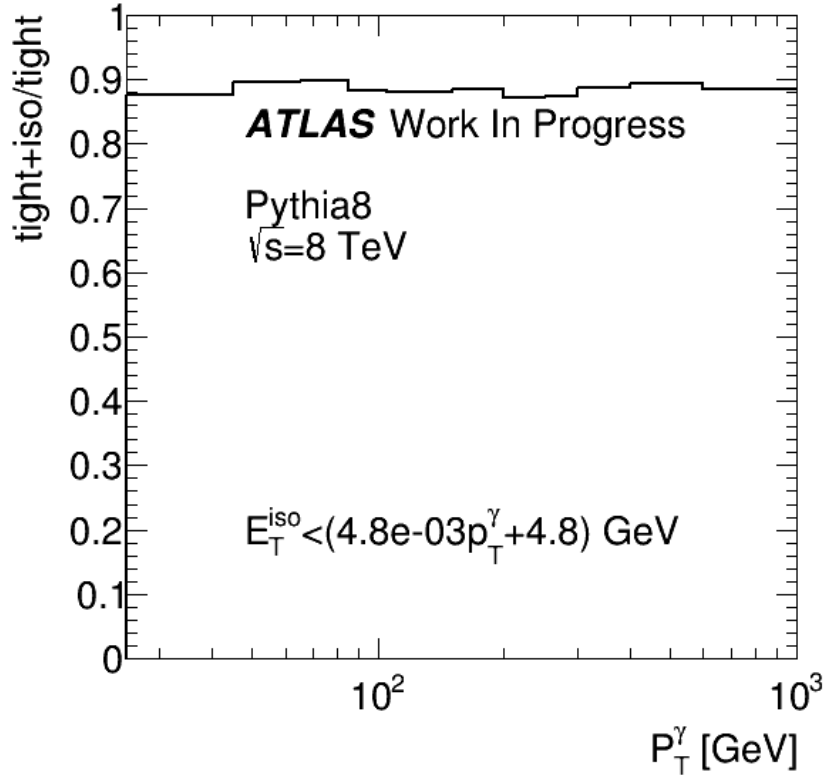


Figure 40: Isolation efficiency for p_T^γ -dependent isolation

9.2 Two-dimensional sideband method

The main background for prompt photons is from hadronic jets containing π^0 mesons that carry most of the jet energy and that decay to photon pairs [17]. These photons are expected to be less isolated than prompt photons due to activity from the other particles in the jet. Tight selection requirements are also optimized to provide good rejection of isolated leading π^0 mesons (see Section 4.1.4).

9.2.1 Derivation of the method

Two-dimensional sideband (2D sideband) method [65] uses photon identification and isolation energy variables (illustration on Figure 41) to obtain a prompt photon yield.

The method is using the number of photons in four regions - A is the signal region; B,C, and D are background control regions. They are defined as

- A - region where photons are passing the tight photon identification criteria and have such isolation energy which allows the photons to be considered isolated
- B - region where photons are passing the tight photon identification criteria but the isolation energy is too high to be considered isolated
- C - region where photons are passing the loose photon identification criteria but failing tight photon identification criteria. These photons are isolated
- D - region where photons are passing the loose photon identification criteria but failing tight photon identification criteria and also failing isolation criterion.

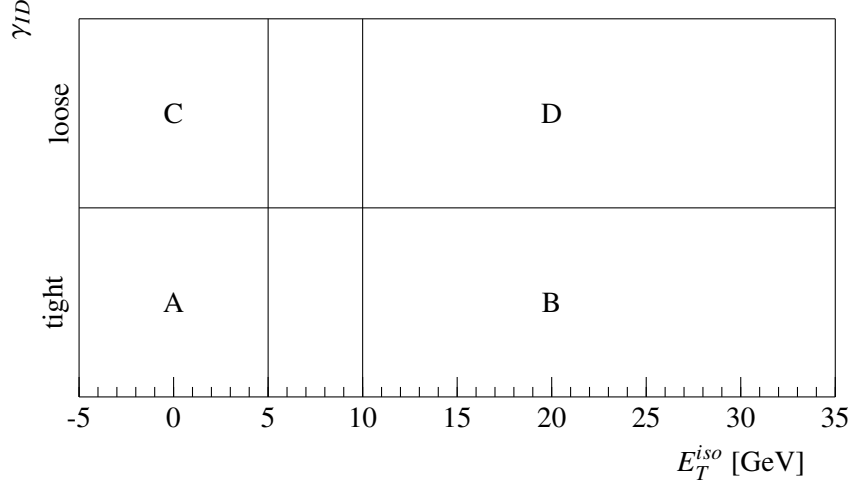


Figure 41: Illustration of the two-dimensional plane used for estimation of the background yield. A is the signal region; B,C, and D are background control regions.

The 2D sideband method is then based on two assumptions:

1. the signal contamination in the three background control regions is small, i.e.

$$\begin{aligned}
 N_A &= N_A^{\text{sig}} + N_A^{\text{BG}}, \\
 N_B &= N_B^{\text{BG}}, \\
 N_C &= N_C^{\text{BG}}, \\
 N_D &= N_D^{\text{BG}}.
 \end{aligned} \tag{8}$$

2. isolation profile in the nontight regions is the same as that of the background in the tight regions, i.e.

$$\frac{N_A^{\text{BG}}}{N_B^{\text{BG}}} = \frac{N_C^{\text{BG}}}{N_D^{\text{BG}}} \tag{9}$$

or

$$\frac{N_A^{\text{BG}} N_D^{\text{BG}}}{N_B^{\text{BG}} N_C^{\text{BG}}} = 1 \tag{10}$$

Using equations 8 and 9, the number of signal photons can be expressed as

$$N_A^{\text{sig}} = N_A - \frac{N_C N_B}{N_D}. \tag{11}$$

Now, let's see what happens if these two assumptions do not hold [66] (this is evaluated using Monte Carlo samples):

If the first assumption does not hold, it means that there is signal contribution in each background control region, i.e.

$$\begin{aligned}
 N_A &= N_A^{\text{sig}} + N_A^{\text{BG}}, \\
 N_B &= N_B^{\text{sig}} + N_B^{\text{BG}}, \\
 N_C &= N_C^{\text{sig}} + N_C^{\text{BG}}, \\
 N_D &= N_D^{\text{sig}} + N_D^{\text{BG}}.
 \end{aligned} \tag{12}$$

Using these equations, equation 11 will turn into

$$N_A^{\text{sig}} = N_A - \frac{(N_B - N_B^{\text{sig}})(N_C - N_C^{\text{sig}})}{(N_D - N_D^{\text{sig}})}. \quad (13)$$

Defining correction factors as

$$c_K = \frac{N_K^{\text{sig}}}{N_A^{\text{sig}}}, \quad (14)$$

where $K = B, C, D$, the number of signal photons can be expressed as

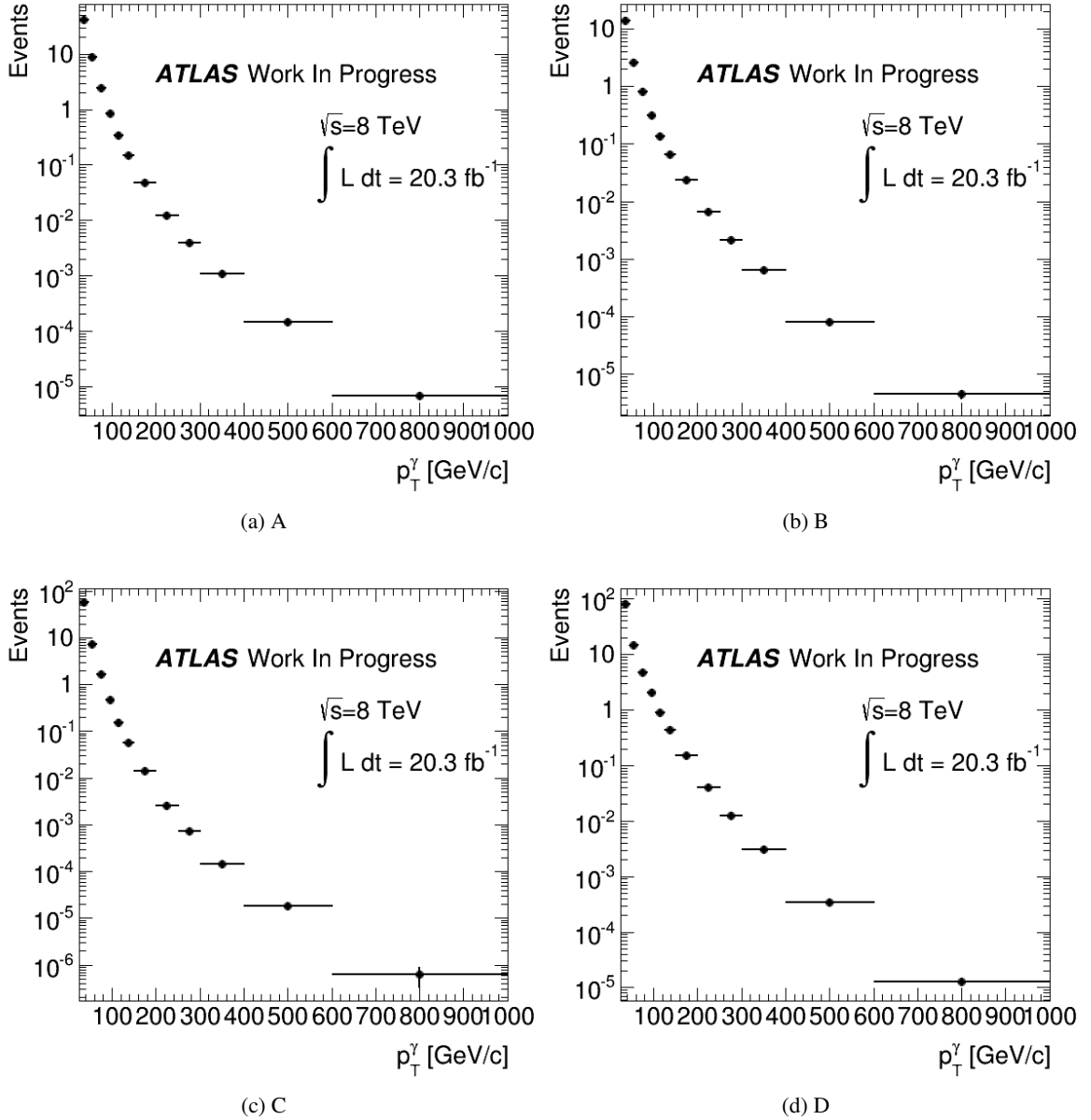


Figure 42: Distribution of p_T^γ in regions A, B, C, and D in data. Errors are statistical only.

$$N_A^{\text{sig}} = N_A - \frac{(N_B - c_B N_A^{\text{sig}})(N_C - c_C N_A^{\text{sig}})}{(N_D - c_D N_A^{\text{sig}})}. \quad (15)$$

This is quadratic equation for N_A^{sig}

$$(N_A^{\text{sig}})^2 (c_B c_C - c_D) + N_A^{\text{sig}} (N_D + c_D N_A - c_B N_C - c_C N_B) + N_B N_C - N_A N_D = 0. \quad (16)$$

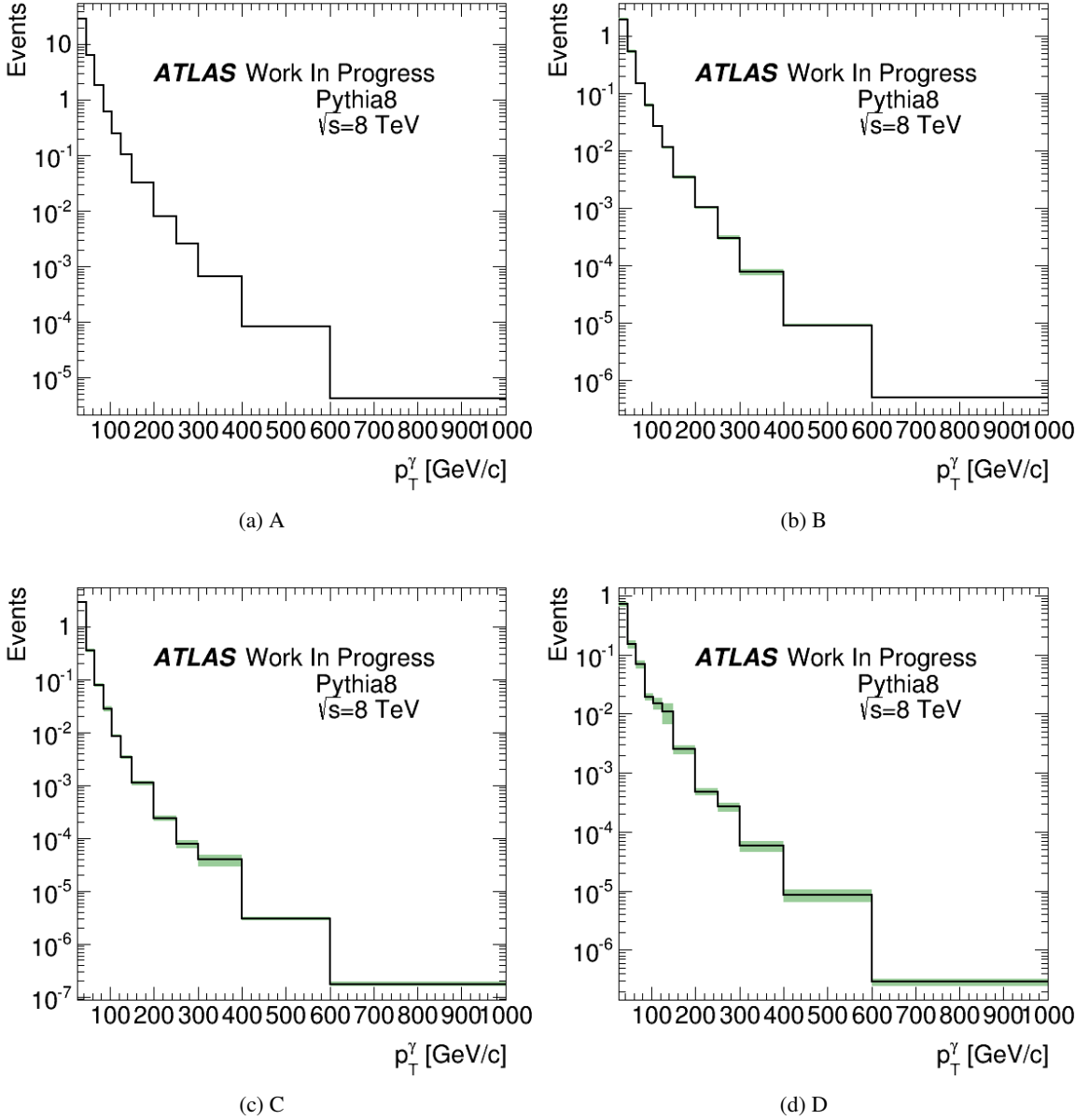
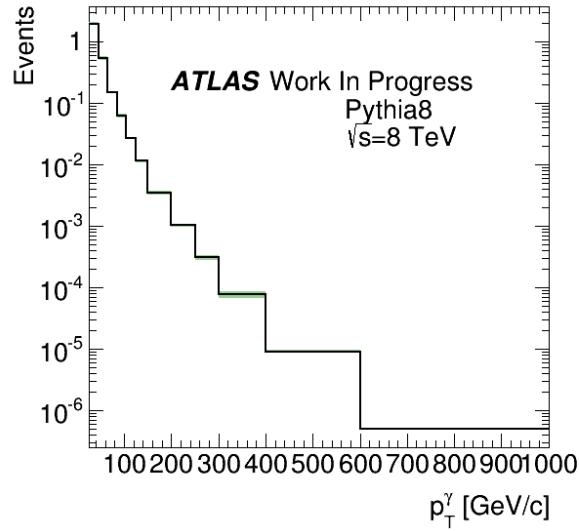


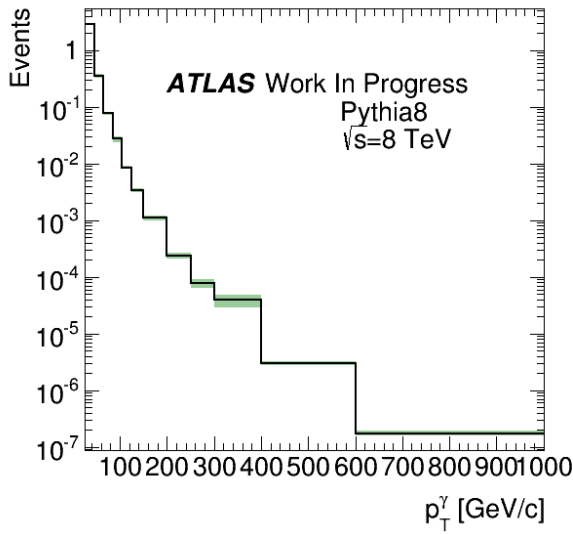
Figure 43: Distribution of p_T^γ of reconstructed photons in regions A, B, C, and D in Monte Carlo. Errors are statistical only.

Now, if the second assumption does not hold, i.e. there is correlation between the variables used to define the x and y axes of Figure 41. Equation 10 will turn into

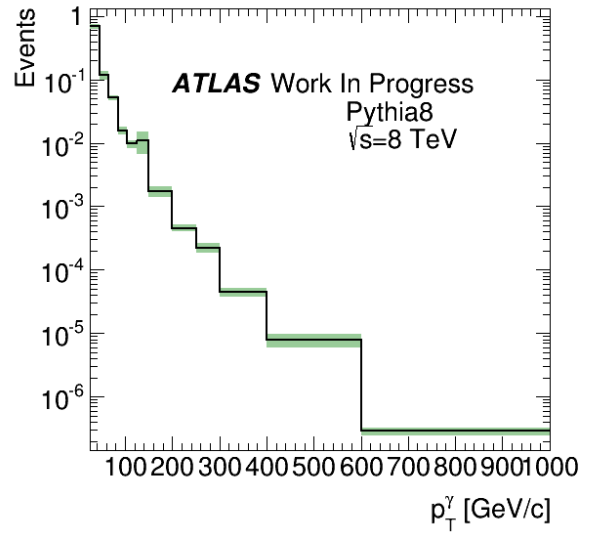
$$R_{MC} \equiv \frac{N_A^{BG} N_D^{BG}}{N_B^{BG} N_C^{BG}} \neq 1 \quad (17)$$



(a) B



(b) C



(c) D

Figure 44: Distribution of p_T^γ of truth photons in regions B, C, and D in Monte Carlo. Errors are statistical only.

and using the same derivation as before, the number of signal photons is

$$N_A^{\text{sig}} = N_A - R_{MC} \frac{(N_B - c_B N_A^{\text{sig}})(N_C - c_C N_A^{\text{sig}})}{(N_D - c_D N_A^{\text{sig}})}. \quad (18)$$

The equations for the number of signal photons are evaluated in each p_T^γ bin.

9.2.2 Results

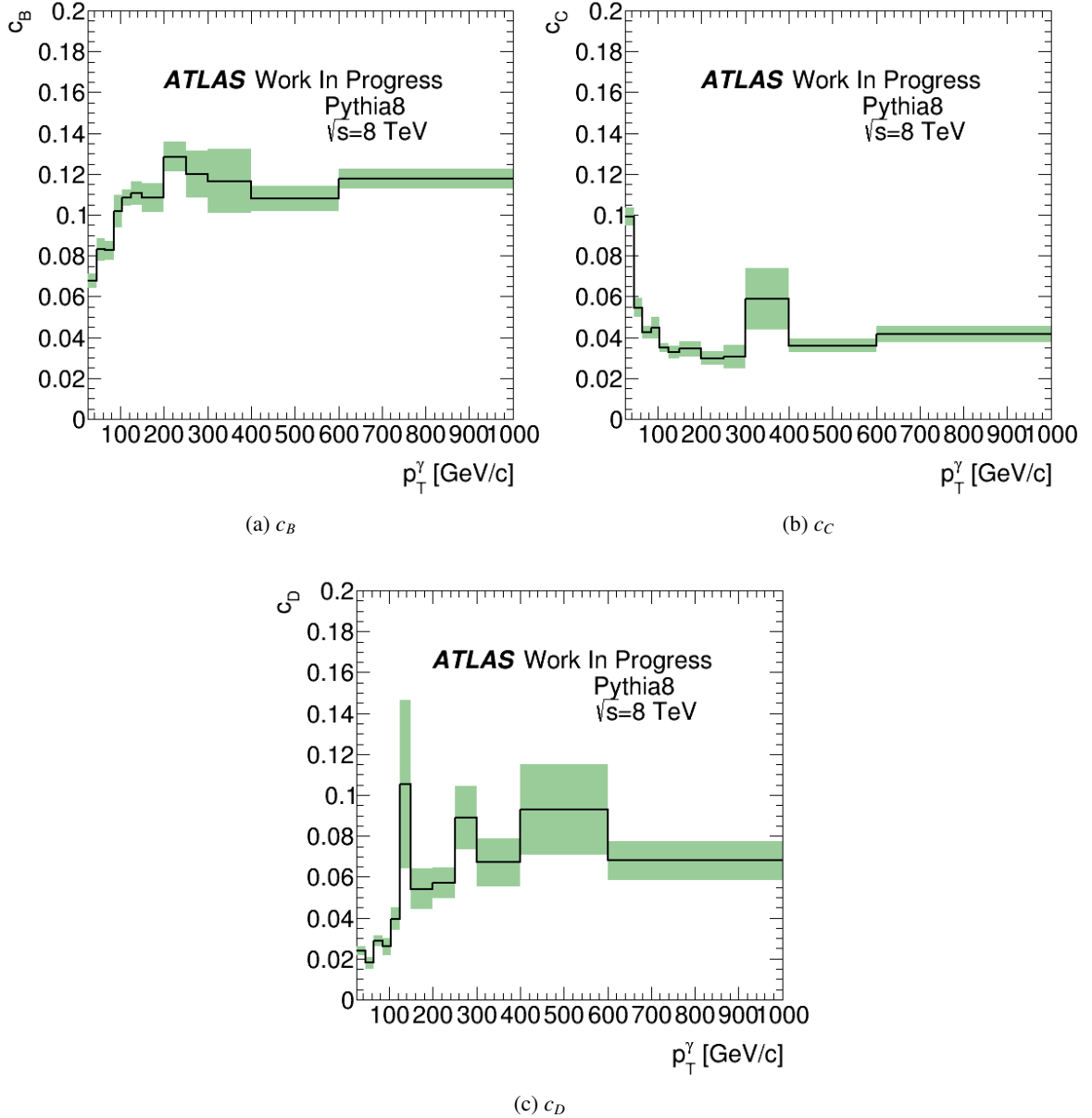


Figure 45: Distribution of 2D sideband method correction factors. Errors are statistical only.

For data, the signal comes from formula 11. Distributions of photons in regions A, B, C, and D will give per bin numbers N_A , N_B , N_C , and N_D . These distributions are on Figure 42.

For Monte Carlo events, the signal is corrected to leakage and comes from formula 13. Distributions of reconstructed and truth photons and in regions A, B, C, and D will give per bin numbers N_A , N_B , N_C , and N_D and N_B^{sig} , N_C^{sig} , and N_D^{sig} . These distributions are on Figure 43 and 44.

These distributions can also be used to calculate corrections factors (defined by equation 14). They are depicted on Figure 45.

Then the signal, tight isolated photon corrected to hadronic jet background, in data and Monte Carlo is shown on Figure 46.

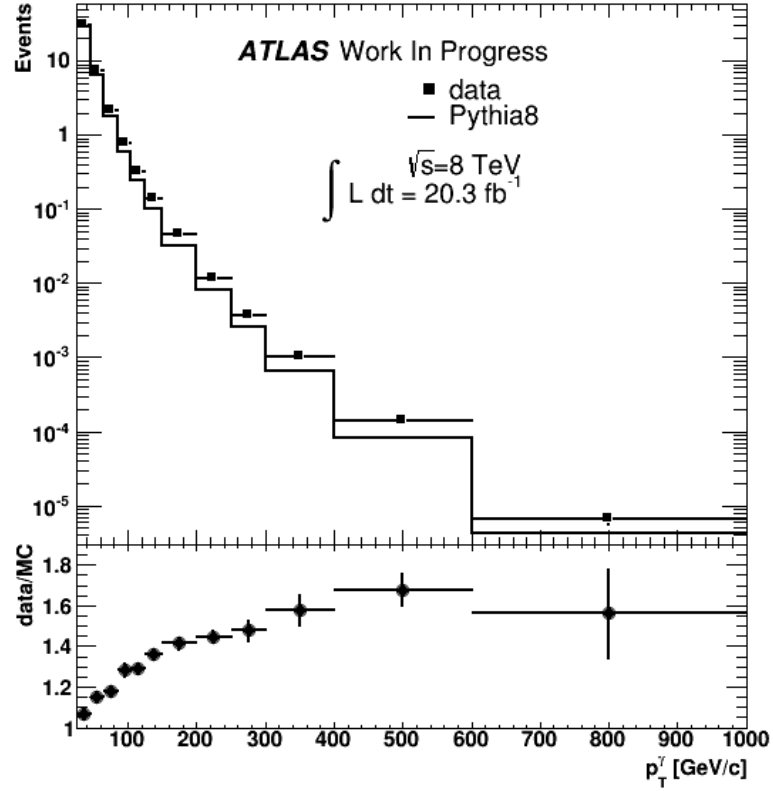


Figure 46: Distribution of p_T^γ in data and Monte Carlo after 2D sideband method. Errors are statistical only.

9.3 Template fitting

As the major background to photon was removed, now it is time to remove the major background to b jet which are processes producing $\gamma+c$ jet and γ +light jet. It is done by template fitting of variable sensitive to quark content. The templates of several variables in Monte Carlo were created to see which one has the most different distributions for b jet and for other jets. Some examples are on Figure 47.

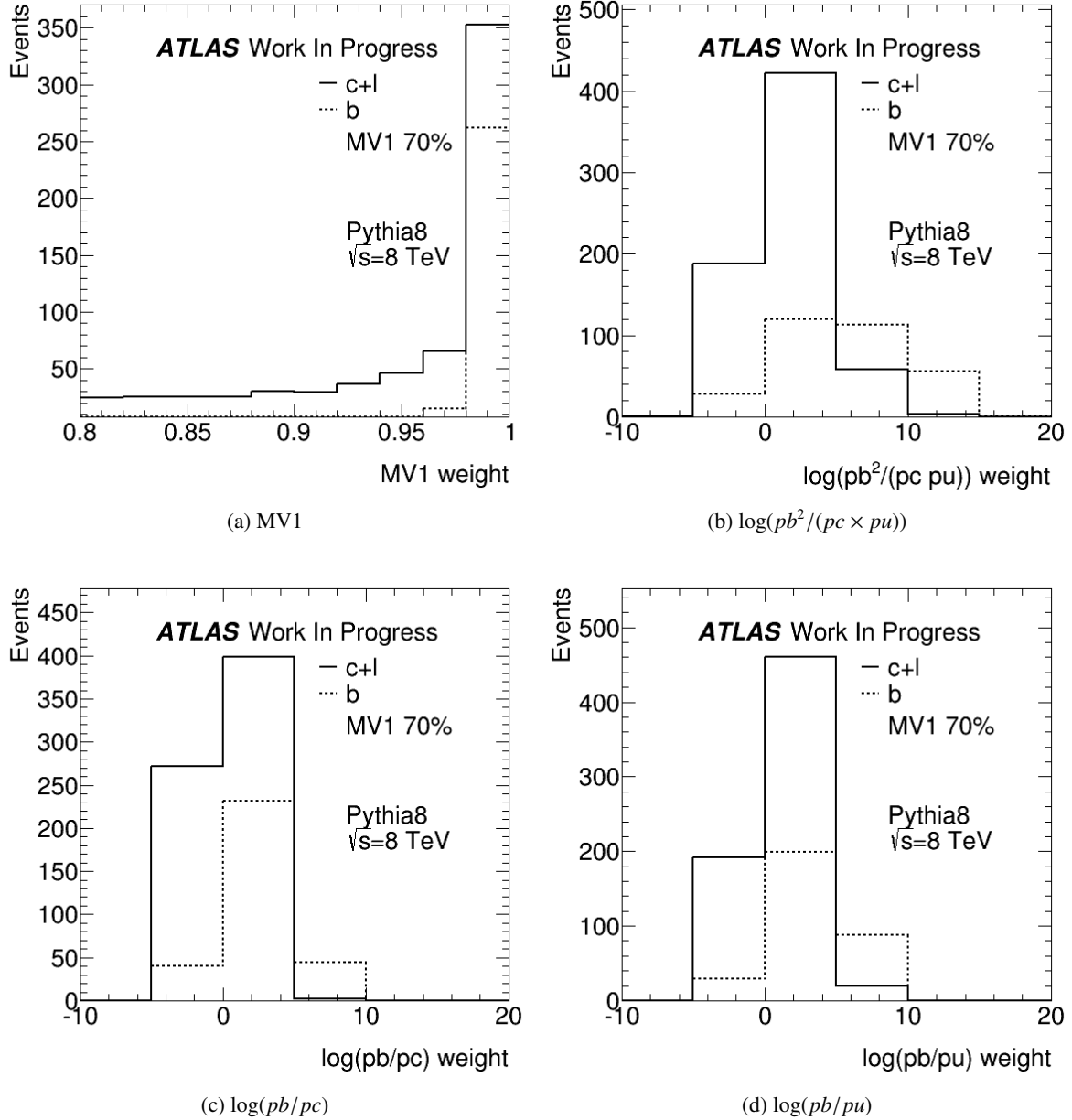


Figure 47: Search for useful variables for template fitting in MV1 and JetFitterCombNN

Figure 47a shows that MV1 weight, used for tagging of the jet, is not suitable for to create the template. Other variables which were checked are from JetFitterCombNN tagger (JetFitter combined with IP3D - SV+IP based, Neural Network based). The likelihoods pb , pc , and pu for b quark, c quark, and light quarks, respectively, are then combined in search for the best discriminating variables. It seems that variable $\log(pb^2/(pc \times pu))$ (see Figure 47b) has the greatest discriminating potential.

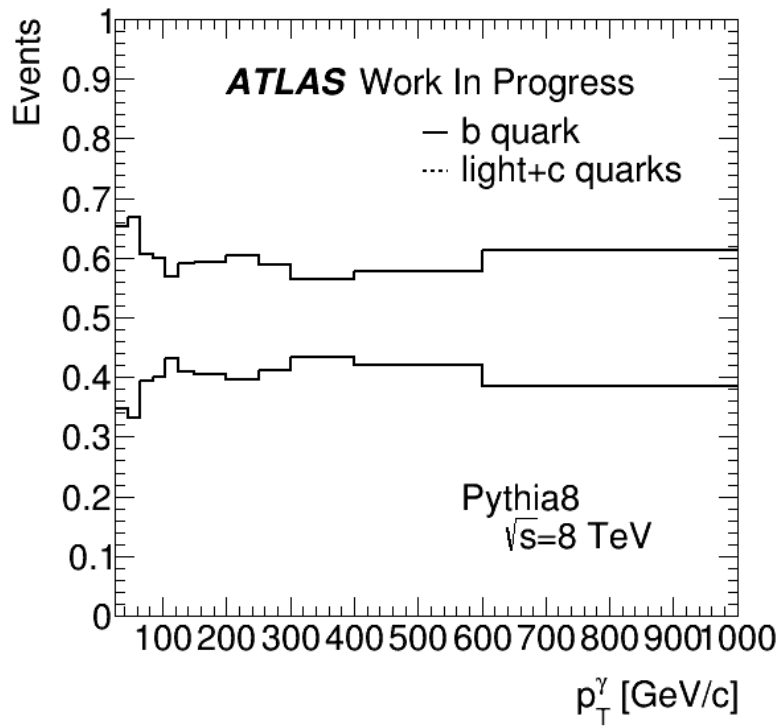


Figure 48: Fraction of b jets and c+light jets obtained by template fitting

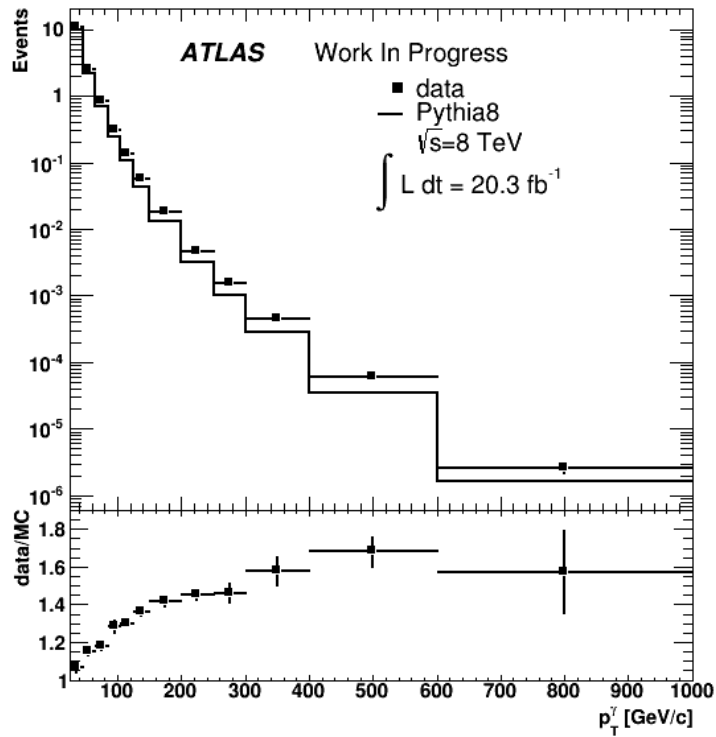
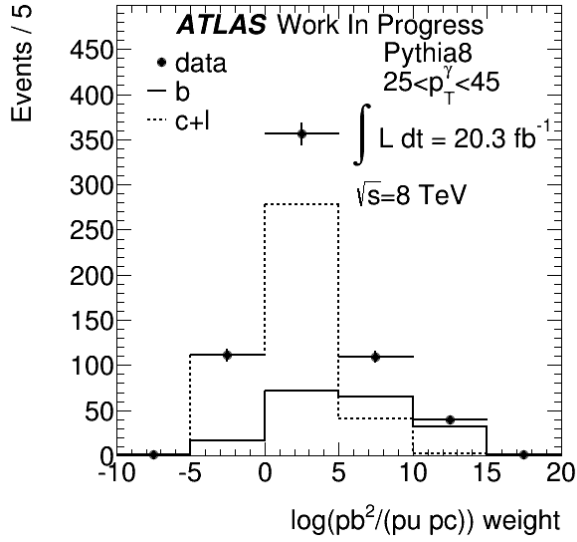


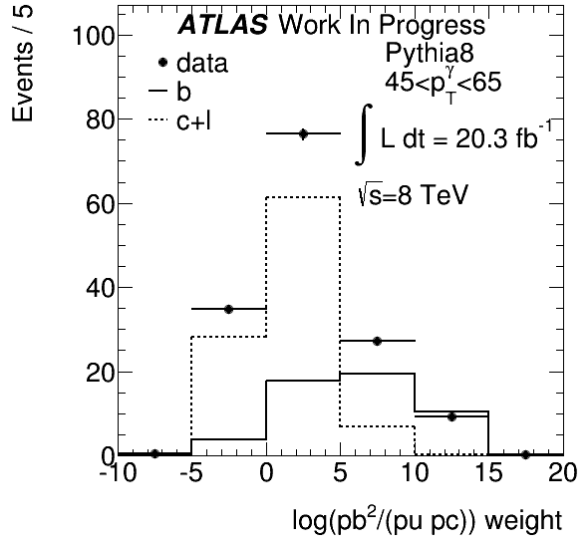
Figure 49: The p_T^γ distribution after background subtraction. Errors are statistical only.

The method to perform the template fitting is following: The events are separated into four regions as in 2D sideband method (see Figure 41). Then distribution of $\log(pb^2/(pc \times pu))$ is created in each p_T^γ bin in each region. As ATLAS detector performance cannot be reproduced perfectly in the simulation, a difference between data and Monte Carlo is observed. To correct this, data-to-MC scale factors [67] were applied to the distributions. After that, the 2D sideband method is performed, i.e. data and Monte Carlo distributions are recalculated using equations 11 and 13, respectively, in each $\log(pb^2/(pc \times pu))$ bin. The result is a series of $\log(pb^2/(pc \times pu))$ distribution (templates) for signal photons in each p_T^γ bin. They are on Figures 50 and 51. These templates are then fitted using TFractionFitter [68] which fits Monte Carlo fractions to data histogram. The fit therefore gives fractions of b jets and c+light jets which reproduces data shape best. The fractions are on Figure 48.

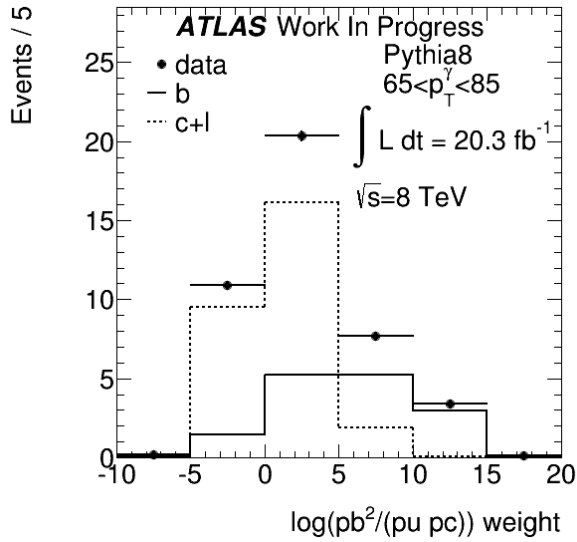
The distributions coming from the 2D sideband method (on Figure 46) were then multiplied by b fraction from template fitting. It gives distributions of γ +b jet in data and Monte Carlo after background subtraction (depicted on Figure 49).



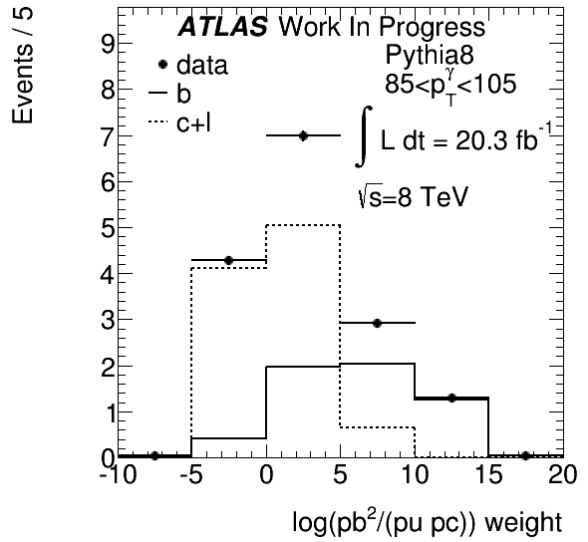
(a)



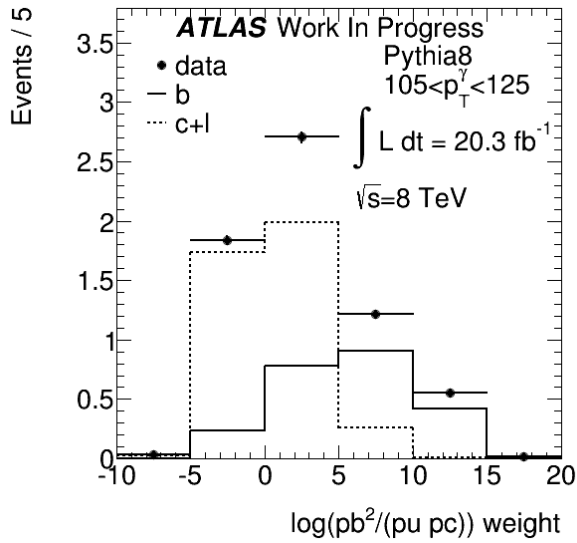
(b)



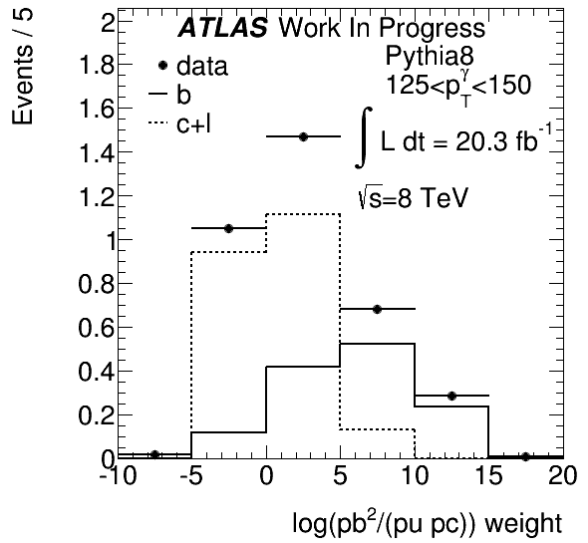
(c)



(d)

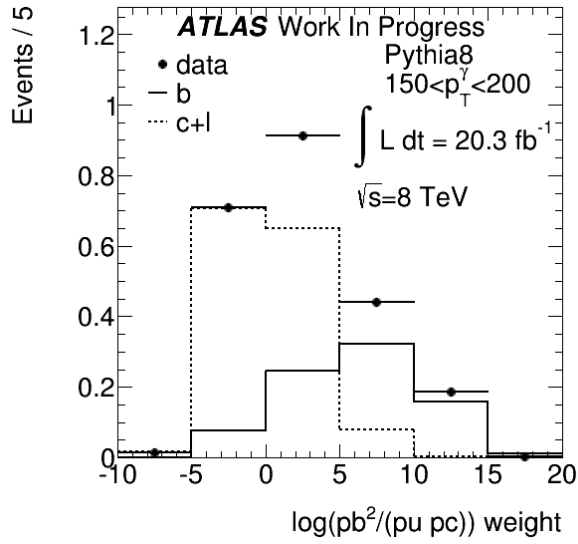


(e)

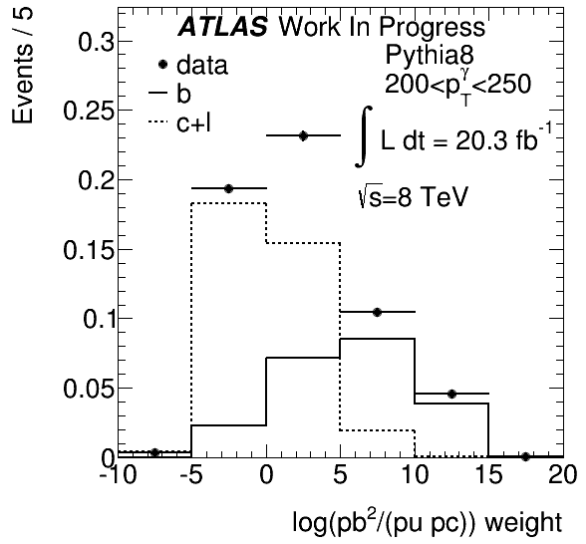


(f)

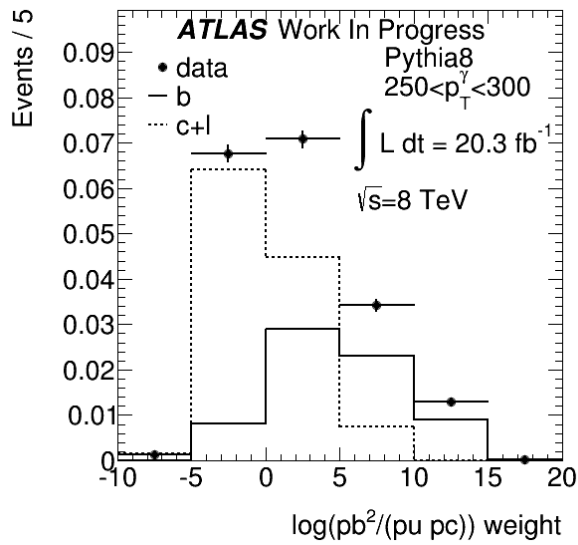
Figure 50: Distributions of $\log(pb^2/(pc \times pu))$ in data and in Monte Carlo (for b jets and for c and light jets) for p_T^γ bins 25-150 GeV. Monte Carlo events are scaled to data. Errors are statistical only.



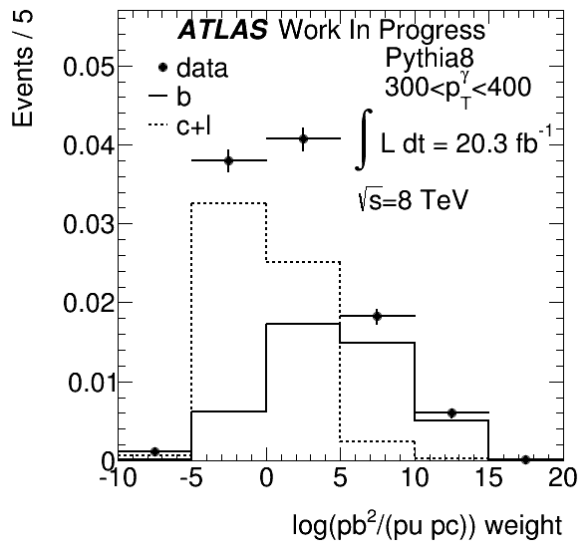
(a)



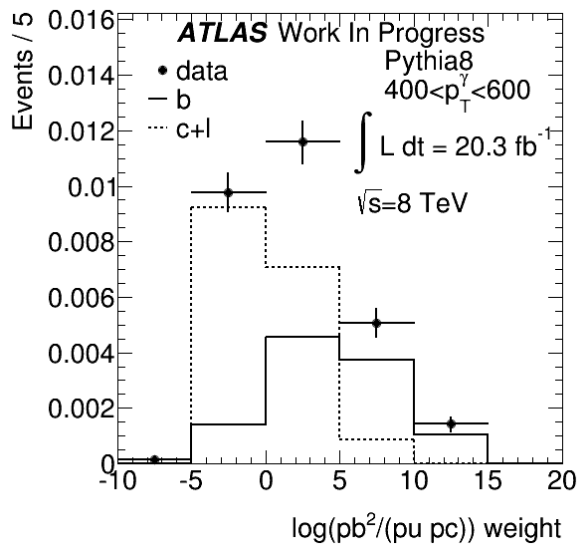
(b)



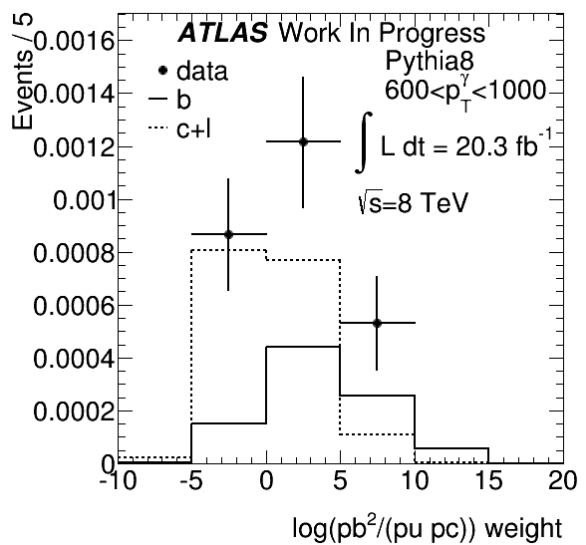
(c)



(d)



(e)



(f)

Figure 51: Distributions of $\log(pb^2/(pc \times pu))$ in data and in Monte Carlo (for b jets and for c and light jets) for p_T^γ bins 150-1000 GeV. Monte Carlo events are scaled to data. Errors are statistical only.

10 Results of the measurement

The events from data and Monte Carlo were filtered and corrected for different effects (detector, physical, etc.). In the next step, major backgrounds were subtracted from them. To obtain an estimate of truth level cross-section, the following formula was used:

$$\frac{d\sigma}{dp_T^\gamma}(i) = \frac{N(p_T^\gamma)(i) \times C(i)}{\Gamma_{bin}(i) \times \int L dt}$$

where $N(p_T^\gamma)(i)$ is number of events in i -th p_T^γ bin after event selection and background subtraction, $\Gamma_{bin}(i)$ is a width of i -th p_T^γ bin,

$$\int L dt$$

is integrated luminosity, and factor

$$C(i) = \frac{N^{MC,truth}(i)}{N^{MC,reco}(i)}$$

with $N^{MC,truth}$ being number of events at the generation level in each p_T^γ bin with $p_T^{jet} > 20$ GeV, $|\eta^{jet}| < 2.4$, $p_T^\gamma > 25$ GeV, $|\eta^\gamma| < 1.37$ or $1.56 < |\eta^\gamma| < 2.37$, and $\Delta R(\gamma - jet) > 1$ and $N^{MC,reco}$ being number of events at reconstruction level in each p_T^γ bin after event selection and background subtraction. The factor $C(i)$ as a function of p_T^γ is displayed on Figure 52. The generation level events were extracted using variables from reconstruction level samples (see Section 5.3).

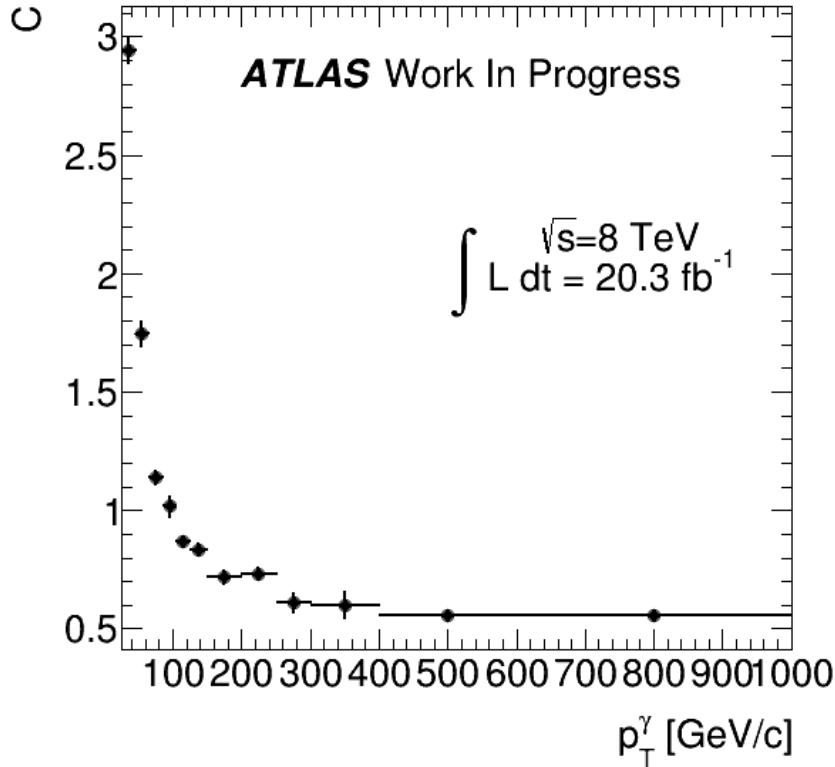


Figure 52: Correction factor used to obtain truth cross-section estimate. Errors are statistical only.

The comparison of final cross-section in data and cross-section extracted from generation level samples (see Section 5.2) is on Figure 53. The integral cross-sections created from these distributions are 750 ± 24 pb for data and 668 ± 10 pb for Monte Carlo. The errors are statistical only.

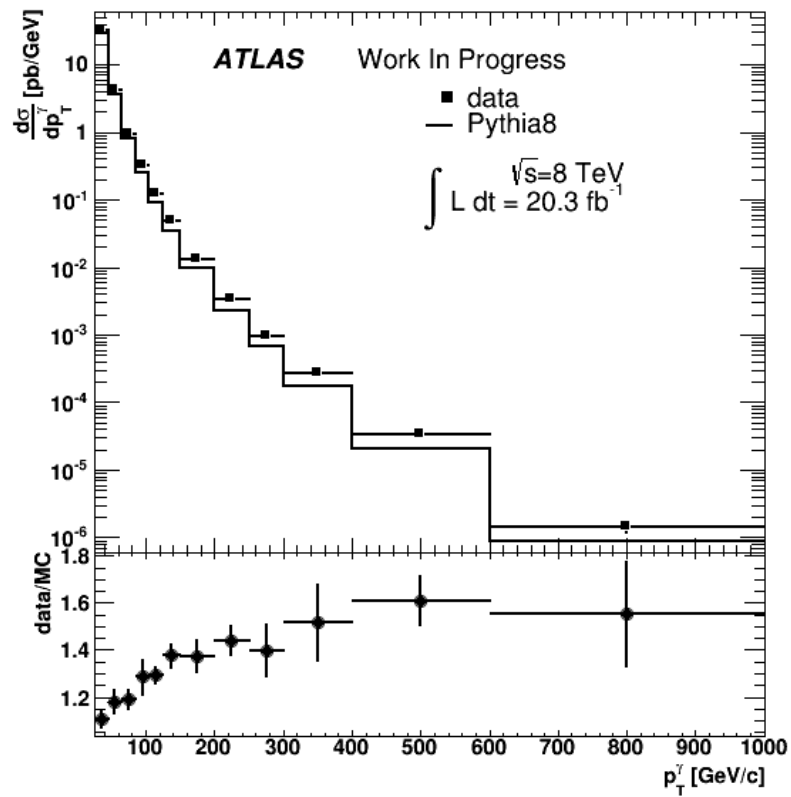


Figure 53: Comparison of final cross-section in data and cross-section extracted from generation level samples. The errors are statistical only.

11 Summary and Conclusions

The measurement of cross-section of prompt photon associated with a b jet ($pp \rightarrow \gamma + b + X$) at $\sqrt{s} = 8$ TeV with the ATLAS detector is presented. Full 8 TeV dataset collected by ATLAS during the year 2012 was used in this analysis. Corresponding integrated luminosity is 20.3 fb^{-1} .

This thesis starts with Introduction providing physics motivation of the measurement, overview of physics models used, description of signal process and overview of results of previous experiments measuring the same or similar processes. In the following sections, Large Hadron Collider and the ATLAS detector are depicted. Definition of basic objects from reconstructed quantities used by this analysis follows. These objects are photon and b jet.

Next part describes data and Monte Carlo samples used for this study. Leading order event generator PYTHIA 8 was used. Prompt photon is defined as any photon created in proton proton collision up to the hadronisation. There are four basic subprocesses contributing to prompt photon + b jet production at leading order(pQCD). These can be divided into subprocesses with direct photons and fragmentation photons. In direct photon subprocesses, photon is directly participating in the hard process. Fragmentation photon arises from the fragmentation of parton directly participating in the hard process. Direct photon subprocesses contributing to the investigated process are Compton QCD and quark-antiquark annihilation with the subsequent gluon splitting into $b\bar{b}$ pair. Fragmentation photon can be created either with single b quark, or with $b\bar{b}$ quark pair. All four subprocesses are present in the Monte Carlo samples used for this analysis. Description of event structure at generator level and corresponding differential cross sections for all four subprocesses are provided in Section 7.

Event selection at the detector reconstruction level is described in Section 8. Background subtraction is described in Section 9. There are two major background processes. The main background for prompt photons are hadronic jets containing photons from π^0 decay. The main background for b jets are jets from c and light quarks. The prompt photon background was subtracted by the 2D sideband method. The b jet background was removed by fitting the template of variable sensitive to the flavour of jet.

Differential cross-section of prompt photon as a function of photon transverse momentum was converted from detector to the particle level using conversion coefficient obtained from Monte Carlo. Cross-sections for data and Monte Carlo are normalised independently. Differential cross-section at particle level obtained from data is compared to the one at event generator level. Values of data distribution lie above Monte Carlo values. The ratio data/Monte Carlo is in the region 1.1 - 1.6, it increases with the transverse momentum of the photon. The difference can be explained by presence of additional effects, e.g. effects of higher orders.

The resulting integrated fiducial cross section is $(750 \pm 24(\text{stat})) \text{ pb}$ for data and $(668 \pm 10(\text{stat})) \text{ pb}$ for Monte Carlo, respectively. Fiducial region of the measurement is : $p_T^\gamma \in \langle 25, 1000 \rangle \text{ GeV}$, $|\eta^\gamma| < 1.37$ or $1.56 < |\eta^\gamma| < 2.37$, $p_T^{\text{jet}} > 20 \text{ GeV}$, $|\eta^{\text{jet}}| < 2.4$, and $\Delta R(\gamma - \text{jet}) > 1$. Up to now, no measurement of this process was published by the LHC experiments. The same process was measured in proton-antiproton collisions at Tevatron at $\sqrt{s} = 1.96 \text{ TeV}$ using integrated luminosity 4.6 fb^{-1} . The cross section measured by the CDF experiment [15] is $\sigma(p\bar{p} \rightarrow \gamma + \geq 1b - \text{jet}) = 54.22 \pm 3.26(\text{stat})_{-5.09}^{+5.04}(\text{syst}) \text{ pb}$. Fiducial region of the measurement is $E_T^\gamma \in \langle 20, 70 \rangle \text{ GeV}$, $|\eta^\gamma| < 1.1$, $E_T^{\text{jet}} > 20 \text{ GeV}$, and $|\eta^{\text{jet}}| < 1.5$. Experiment ATLAS published measurement of similar process $pp \rightarrow \gamma + \text{jet} + X$ using 37 pb^{-1} of data collected during the year 2010 at $\sqrt{s} = 7 \text{ TeV}$. Cross section of the process is about 3890 pb , corresponding fiducial region is $E_T^\gamma \in \langle 45, 400 \rangle$, $|\eta^\gamma| < 1.37$ or $1.52 < |\eta^\gamma| < 2.37$, $p_T^{\text{jet}} > 40 \text{ GeV}$, and $|\eta^{\text{jet}}| < 2.37$.

Finally, the first measurement of the cross section of the process ($pp \rightarrow \gamma + b + X$) at LHC is presented. Statistical uncertainties only are taken into account yet. Work on the extraction of all systematic uncertainties and more detailed analysis is ongoing.

Appendices

A Data and MC samples details

A.1 Data samples

The following data containers in format NTUP_COMMON [69] were used

- user.pajchel.data12_8TeV.periodA.physics_Egamma.PhysCont.NTUP_COMMON.pro14_v02_u1_p1562/
- user.pajchel.data12_8TeV.periodB.physics_Egamma.PhysCont.NTUP_COMMON.pro14_v02_u1_p1562/
- user.pajchel.data12_8TeV.periodC.physics_Egamma.PhysCont.NTUP_COMMON.pro14_v02_u1_p1562/
- user.pajchel.data12_8TeV.periodD.physics_Egamma.PhysCont.NTUP_COMMON.pro14_v02_u1_p1562/
- user.pajchel.data12_8TeV.periodE.physics_Egamma.PhysCont.NTUP_COMMON.pro14_v02_u1_p1562/
- user.pajchel.data12_8TeV.periodG.physics_Egamma.PhysCont.NTUP_COMMON.pro14_v02_u1_p1562/
- user.pajchel.data12_8TeV.periodH.physics_Egamma.PhysCont.NTUP_COMMON.pro14_v02_u1_p1562/
- user.pajchel.data12_8TeV.periodI.physics_Egamma.PhysCont.NTUP_COMMON.pro14_v02_u1_p1562/
- user.pajchel.data12_8TeV.periodJ.physics_Egamma.PhysCont.NTUP_COMMON.pro14_v02_u1_p1562/
- user.pajchel.data12_8TeV.periodL.physics_Egamma.PhysCont.NTUP_COMMON.pro14_v02_u1_p1562/

A.2 Monte Carlo generator level samples

Available samples at the generator level for energy $\sqrt{s} = 8$ TeV created by PYTHIA 8. Here is the list of datasets with number of events, cross section, and filtering efficiency:

- 3M events, crossSection_mean=1.2354E+06 nb, GenFiltEff_mean=2.3477E-04
mc12_8TeV.129170.Pythia8_AU2CTEQ6L1_gammajet_DP17.evgen.EVNT.e1146/
- 3M events, crossSection_mean=5.8768E+04 nb, GenFiltEff_mean=4.0218E-04
mc12_8TeV.129171.Pythia8_AU2CTEQ6L1_gammajet_DP35.evgen.EVNT.e1146/
- 6M events, crossSection_mean=3.4250E+03 nb, GenFiltEff_mean=5.7050E-04
mc12_8TeV.129172.Pythia8_AU2CTEQ6L1_gammajet_DP70.evgen.EVNT.e1146/
- 3M events, crossSection_mean=1.2217E+02 nb, GenFiltEff_mean=9.6932E-04
mc12_8TeV.129173.Pythia8_AU2CTEQ6L1_gammajet_DP140.evgen.EVNT.e1146/
- 2M events, crossSection_mean= 3.3487E+00 nb, GenFiltEff_mean=1.4457E-03
mc12_8TeV.129174.Pythia8_AU2CTEQ6L1_gammajet_DP280.evgen.EVNT.e1146/
- 2M events, crossSection_mean=1.1563E-01 nb, GenFiltEff_mean=1.8056E-03
mc12_8TeV.129175.Pythia8_AU2CTEQ6L1_gammajet_DP500.evgen.EVNT.e1146/
- 100k events, crossSection_mean=4.9226E-03 nb, GenFiltEff_mean=1.9036E-03
mc12_8TeV.129176.Pythia8_AU2CTEQ6L1_gammajet_DP800.evgen.EVNT.e1144/

A.3 Monte Carlo reconstruction level samples

As these datasets were created from generator level samples, they also contain jet+jet and gamma+jet events with at least one hard process or parton shower photon with $p_T > 17, 35, 70, 140, 280, 500$ and 800 GeV.

List of PYTHIA 8 datasets:

- 2999999 events, crossSection_mean=1.2354+06 nb, GenFiltEff_mean=2.3477E-04
mc12_8TeV.129170.Pythia8_AU2CTEQ6L1_gammajet_DP17.merge.NTUP_COMMON
.e1146_s1737_s1741_r4829_r4540_p1575_tid04820703_00
- 2999694 events, crossSection_mean=5.8768E+04 nb, GenFiltEff_mean=4.0218E-04
mc12_8TeV.129171.Pythia8_AU2CTEQ6L1_gammajet_DP35.merge.NTUP_COMMON
.e1146_s1737_s1741_r4829_r4540_p1575_tid01557926_00
- 2999987 events, crossSection_mean=3.4250E+03 nb, GenFiltEff_mean=5.7050E-04
mc12_8TeV.129172.Pythia8_AU2CTEQ6L1_gammajet_DP70.merge.NTUP_COMMON
.e1146_s1737_s1741_r4829_r4540_p1575_tid01557925_00
- 999996 events, crossSection_mean=1.2217E+02 nb, GenFiltEff_mean=9.6932E-04
mc12_8TeV.129173.Pythia8_AU2CTEQ6L1_gammajet_DP140.merge.NTUP_COMMON
.e1146_s1737_s1741_r4829_r4540_p1575_tid01557924_00
- 999989 events, crossSection_mean= 3.3487E+00 nb, GenFiltEff_mean=1.4457E-03
mc12_8TeV.129174.Pythia8_AU2CTEQ6L1_gammajet_DP280.merge.NTUP_COMMON
.e1146_s1737_s1741_r4829_r4540_p1575_tid01557923_00
- 999877 events, crossSection_mean=1.1563E-01 nb, GenFiltEff_mean=1.8056E-03
mc12_8TeV.129175.Pythia8_AU2CTEQ6L1_gammajet_DP500.merge.NTUP_COMMON
.e1146_s1737_s1741_r4829_r4540_p1575_tid01557922_00
- 99997 events, crossSection_mean=4.9226E-03 nb, GenFiltEff_mean=1.9036E-03
mc12_8TeV.129176.Pythia8_AU2CTEQ6L1_gammajet_DP800.merge.NTUP_COMMON
.e1444_s1737_s1741_r4829_r4540_p1575_tid01557921_00

B $\gamma + c$ events at $\sqrt{s}=8$ TeV at generator level

While it is not a trivial problem to identify c quarks/jets with algorithms designed to identify b quarks/jet, it is very simple at the generator level where particles can be identified using PDG ID in the event record. The same analysis which was performed for b flavour in Section 7, can be done at the same time for c flavour. So, the method is described in the section about b flavour. Here are the results for c flavour.

B.1 PYTHIA 8 processes

B.1.1 $Qg \rightarrow \gamma Q$

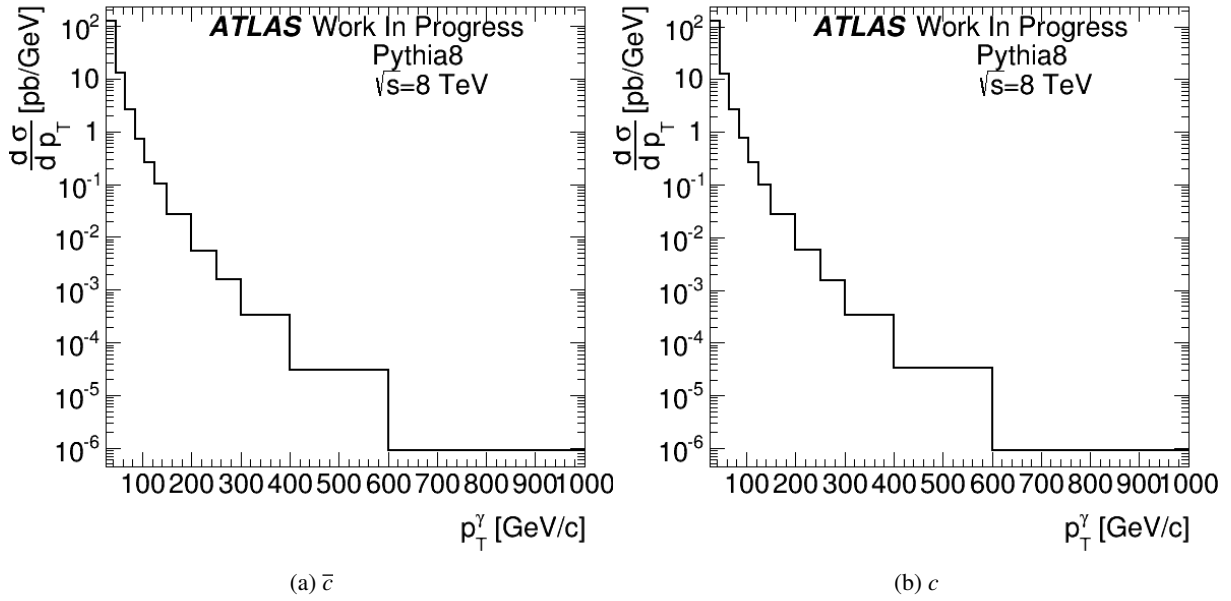


Figure 54: Cross-section of Compton-QCD for c flavoured quarks

Structure of the PYTHIA 8 event on Figure 59 represents Feynman diagrams depicted on Figure 2. The event starts with two incoming protons. Hard scattering happens in vertex 3. Quarks and gluons with barcodes 3 and 4 are coming in the vertex. Photon and c (or \bar{c}) quark with barcode 5 and 6 are going out of the vertex.

Figure 54 shows differential cross-section of processes $\bar{c}g \rightarrow \gamma\bar{c}$ and $cg \rightarrow \gamma c$.

B.1.2 $q\bar{q} \rightarrow \gamma g, g \rightarrow Q\bar{Q}$

Structure of the PYTHIA 8 event on Figure 60 represents Feynman diagrams depicted on Figure 3. The event starts with two incoming protons. Quarks and gluons with barcodes 3 and 4 are scattered in vertex 3. Photon and gluon with barcode 5 and 6 are going out of the vertex. Photon after that just changes its status. Gluon decays into $c\bar{c}$ pair.

Figure 55 shows differential cross-section of process $q\bar{q} \rightarrow \gamma g, g \rightarrow c\bar{c}$.

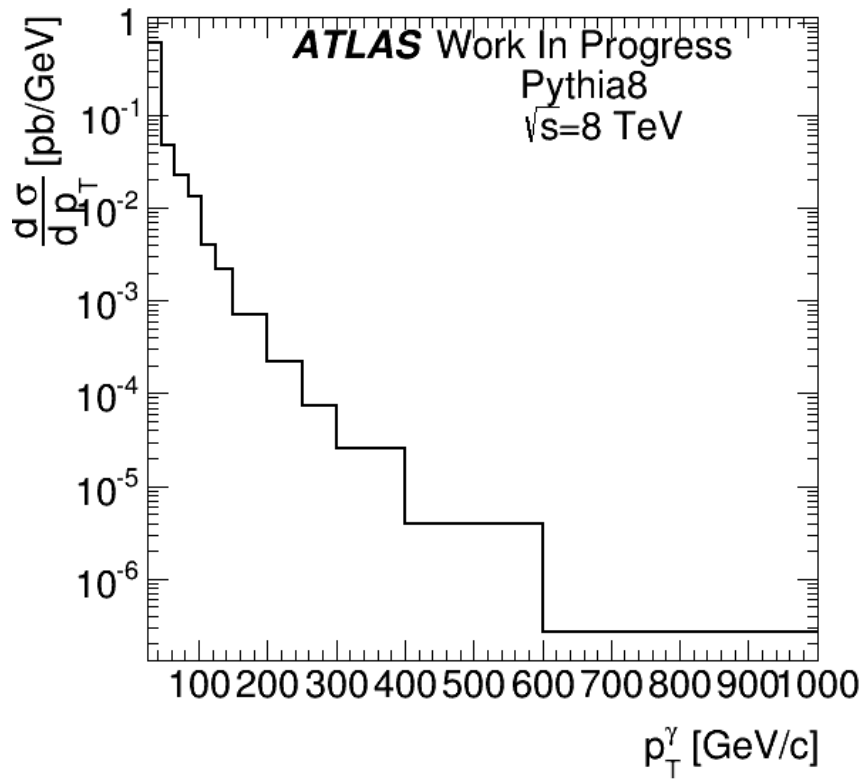


Figure 55: Cross-section of quark-antiquark annihilation for c flavoured quarks

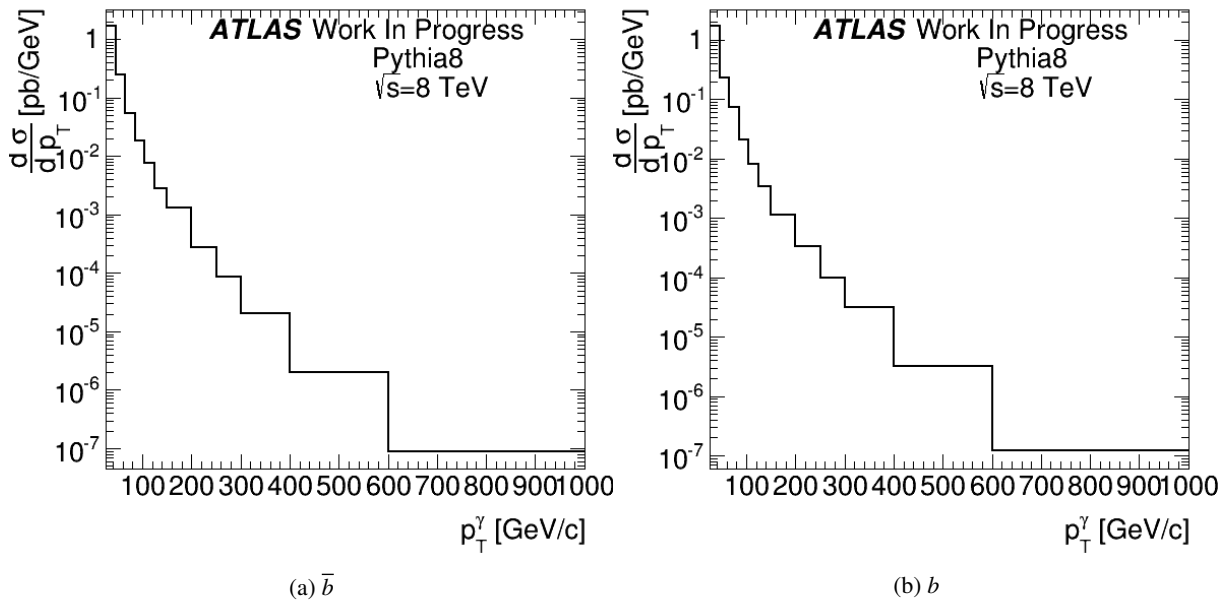


Figure 56: Cross-section of event where fragmentation photon is created with c flavoured quark

B.1.3 $qq, gg \rightarrow Qq, q \rightarrow \gamma + X$

Structure of the PYTHIA 8 event on Figure 61 represents Feynman diagrams depicted on Figure 6. The event starts with two incoming protons. Quarks with barcodes 3 and 4 enter the vertex 3. One c (or \bar{c}) quark goes out. The other particle is quark of any flavour which decays into several particles including photon.

Figure 56 shows differential cross-section of processes $qq, gg \rightarrow \bar{c}q, q \rightarrow \gamma + X$ and $qq, gg \rightarrow cq, q \rightarrow \gamma + X$.

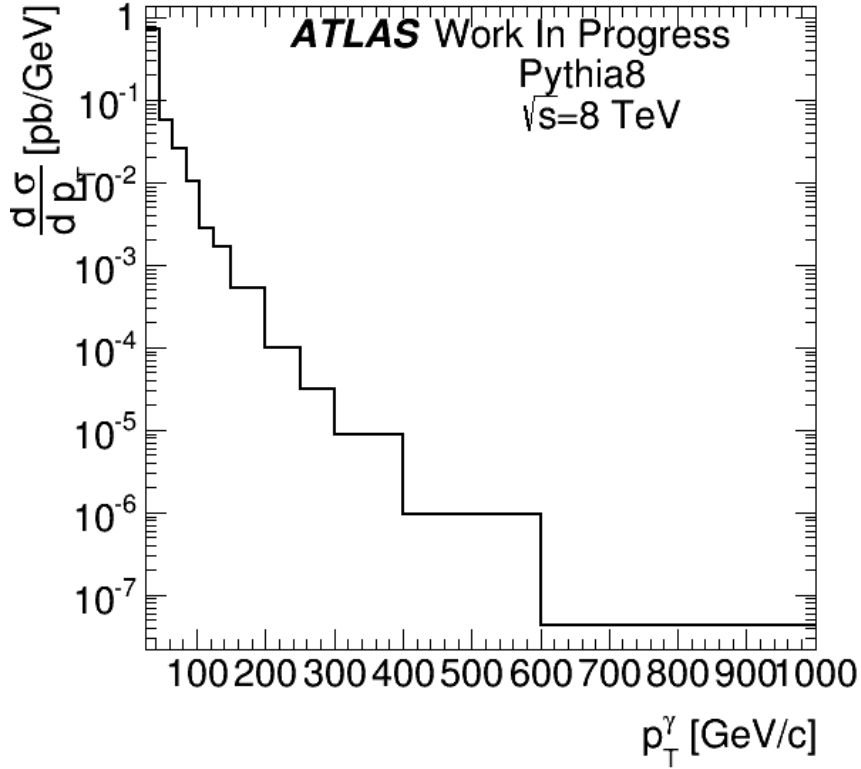


Figure 57: Cross-section of event where fragmentation photon is created with $c\bar{c}$ pair

B.1.4 $qg \rightarrow qq, q \rightarrow \gamma + X, g \rightarrow Q\bar{Q}$

Structure of the PYTHIA 8 event on Figure 62 represents Feynman diagrams depicted on Figure 5. The event starts with two incoming protons. Quarks and gluons with barcodes 3 and 4 interact in the vertex 3. One particle going out of the vertex is gluon which is decaying into $c\bar{c}$ pair. The other particle going out of the vertex is quark of any flavour which decays into several particles including photon.

Figure 57 shows differential cross-section of process $qg \rightarrow qq, q \rightarrow \gamma + X, g \rightarrow c\bar{c}$

The resulting cross-section of all these processes combined is on Figure 58.

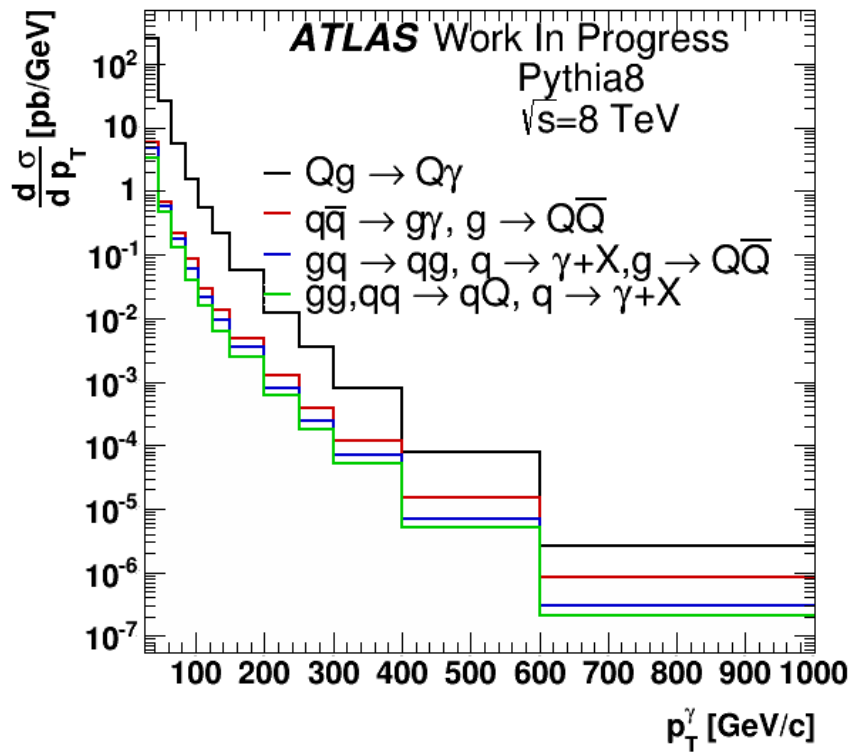


Figure 58: Combined cross-section of direct and fragmentation processes

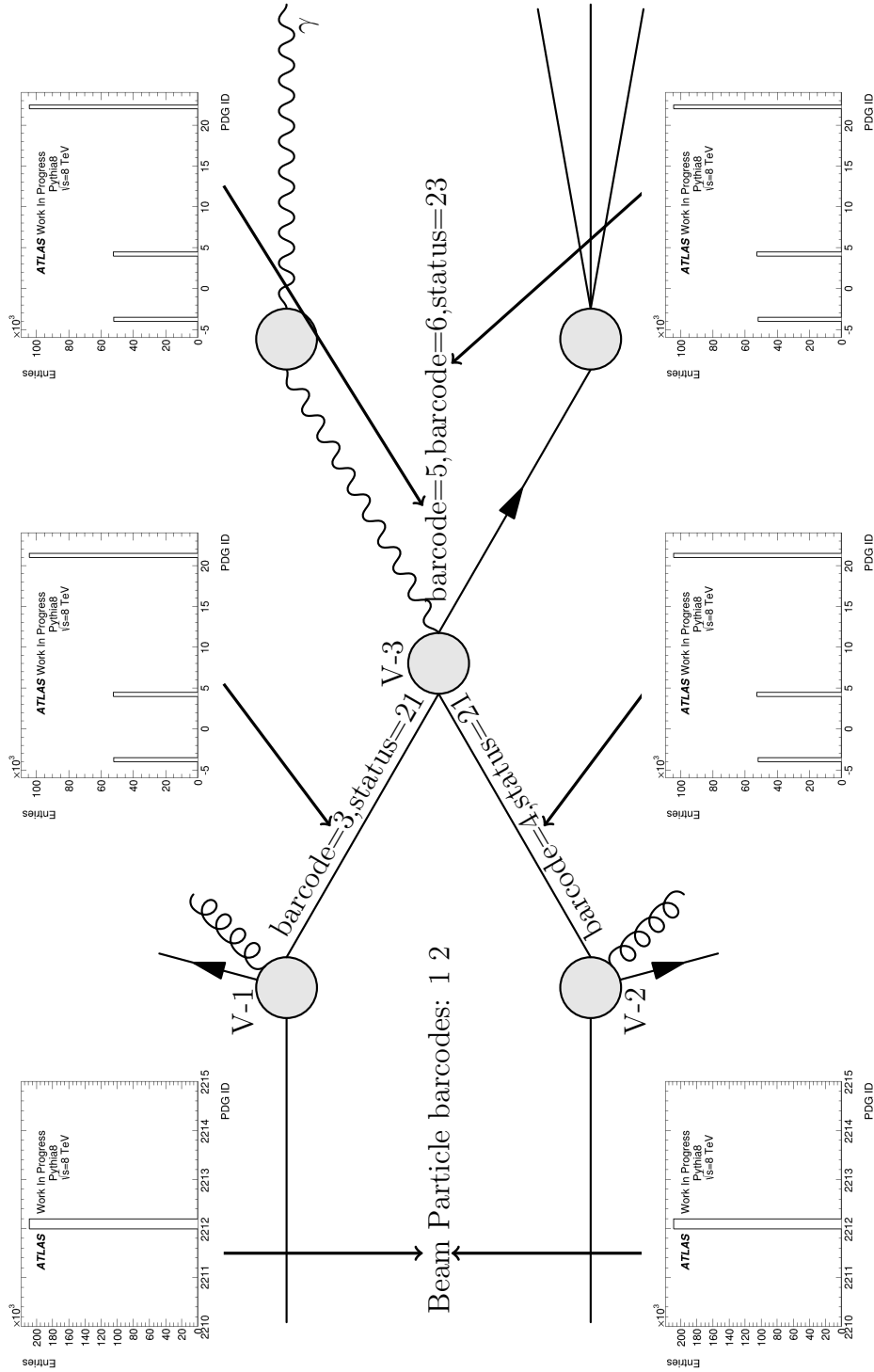


Figure 59: Event structure of the Compton-QCD. The figure in the middle represents event structure, the histograms on the edges show PDG ID of particles in the event. The incoming particles are protons (PDGID=2212). Vertex 3 is the interaction vertex. Particles coming in the vertex are c quark (PDGID=4) or \bar{c} quark (PDGID=-4) and gluon (PDGID=-4) with status 21. Particles going out of the vertex are c quark (PDGID=4) or \bar{c} quark (PDGID=-4) a photon (PDGID=22) with status 23. After that, photon changes status to stable particle and c flavoured quark decays.

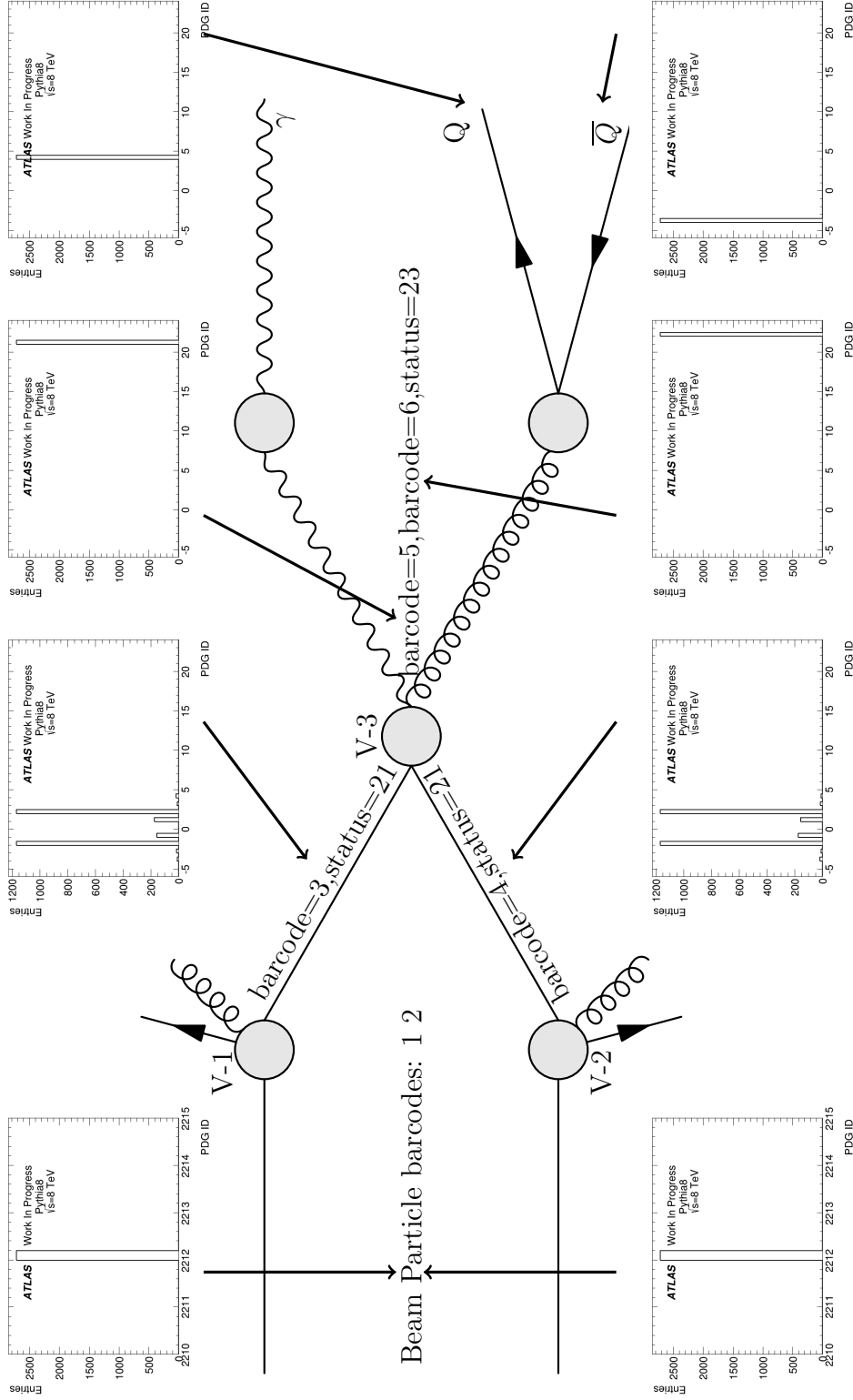


Figure 60: Event structure of the quark-antiquark annihilation. The figure in the middle represents event structure, the histograms on the edges show PDG ID of particles in the event. The incoming particles are protons (PDGID=2212). Vertex 3 is the interaction vertex. Particles coming in the vertex are quarks (PDGID $\in \{-5, 5\}$) with status 21. Particles going out of the vertex are gluon (PDGID=21) and photon (PDGID=22) with status 23. After that, photon changes status to stable particle and gluon decays into $c\bar{c}$ pair.

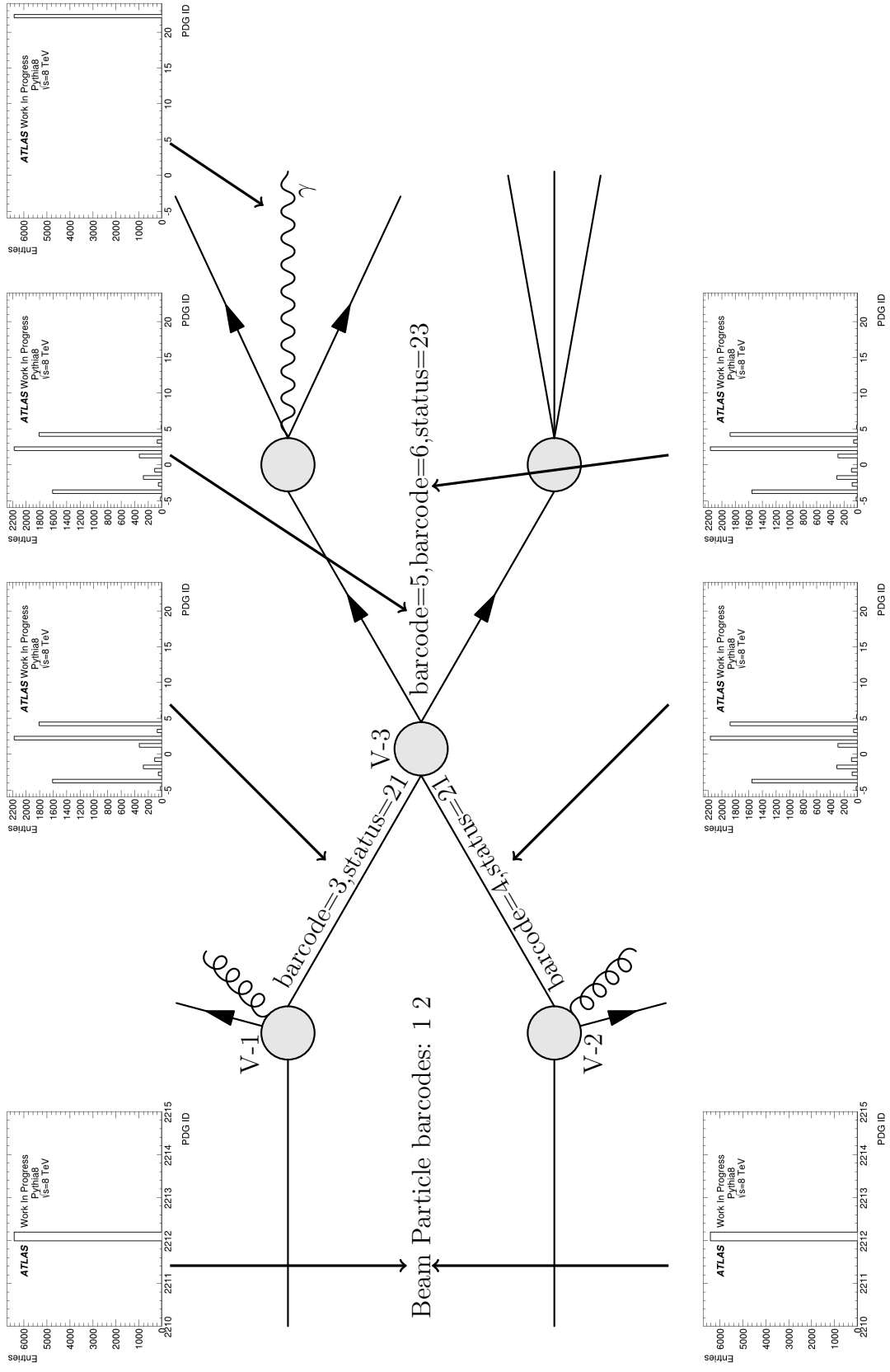


Figure 61: Event structure of event where fragmentation photon is created with c flavoured quark. The figure in the middle represents event structure, the histograms on the edges show PDG ID of particles in the event. The incoming particles are protons (PDGID=2212). Vertex 3 is the interaction vertex. Particles coming in the vertex are quarks (PDGID= -5, 5) with status 21. Particles going out of the vertex c quark (PDGID=4) (or \bar{c} quark (PDGID=-4)) and another quark (PDGID= -5, 5) with status 23. After that, quark decays into several particles including photon.

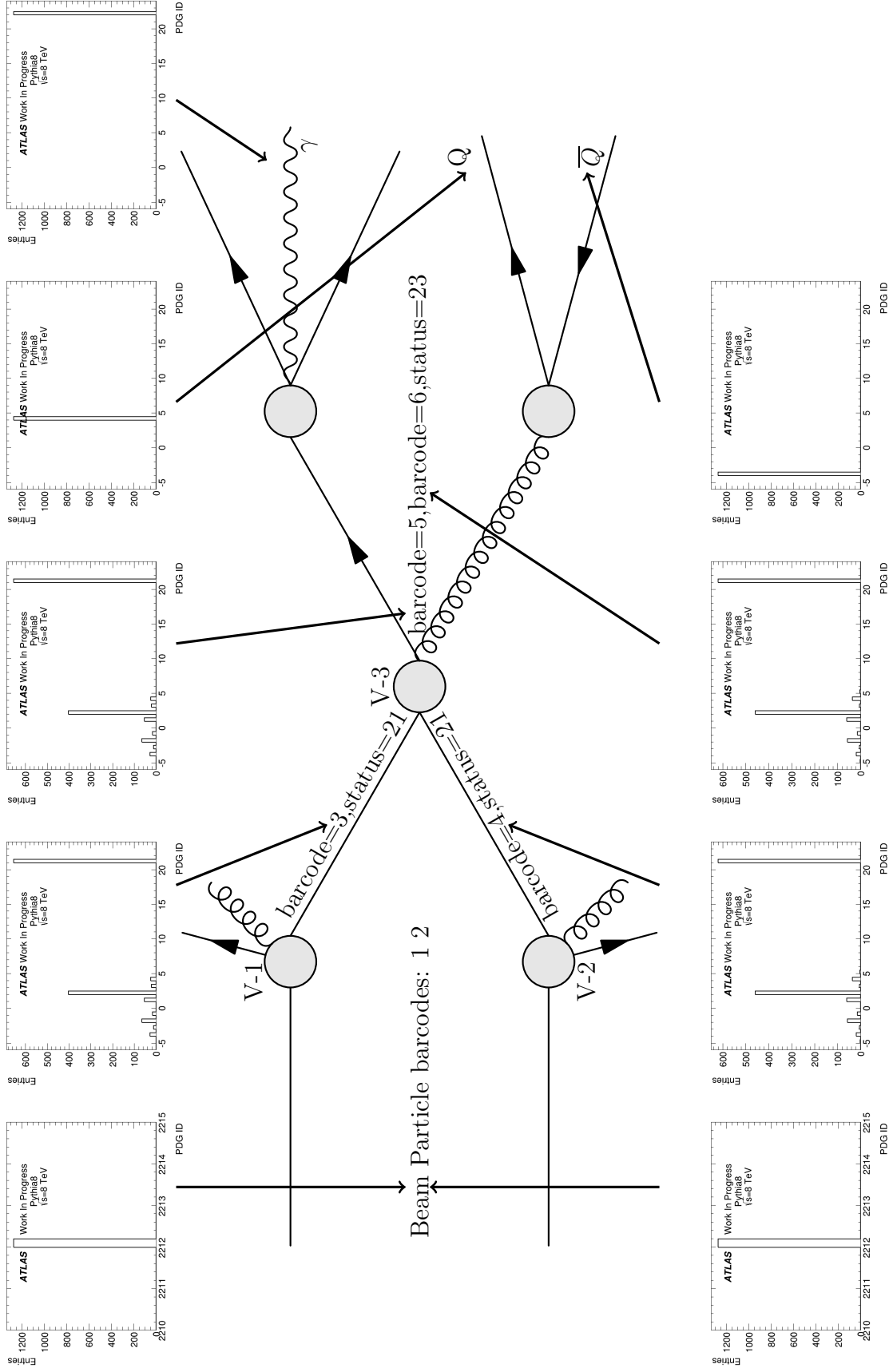


Figure 62: Event structure of event where fragmentation photon is created with $c\bar{c}$ pair. The figure in the middle represents event structure, the histograms on the edges show PDG ID of particles in the event. The incoming particles are protons (PDGID=2212). Vertex 3 is the interaction vertex. Particles coming in the vertex are quark (PDGID=-5, 5) and gluons (PDGID=21) with status 21. Particles going out of the vertex are gluon (PDGID=21) quark (PDGID=-5, 5) with status 23. After that, gluon decays into several particles including photon.

C Previous reports

C.1 About the analysis

C.1.1 Talks

M. Svatos, Processes with direct photon and heavy quarks; Workshop of Experimental Nuclear and Particle Physics 2014; Edited by T. Jakoubek, V. Pacik, M. Sedlackova and M. Vlasak; http://wejcf2014.ejcf.cz/wejcf2014_proceedings.pdf; ISBN 978-80-01-05657-8

C.1.2 Working groups meetings

- Photon + HF (2012) <https://indico.cern.ch/event/217079/>
- photon+b cross section measurement <https://indico.cern.ch/event/287608/>
- Photon+HF <https://indico.cern.ch/event/293338/>
- photon+HF <https://indico.cern.ch/event/309225/>
- photon+b <https://indico.cern.ch/event/343024/>
- photon+b <https://indico.cern.ch/event/359312/>
- Status of photon+b <https://indico.cern.ch/event/382765/>

C.2 General

M. Svatos, Photon, diphoton and photon+jet production measured with the ATLAS detector, Proceedings of Science, XXI International Workshop on Deep-Inelastic Scattering and Related Subject -DIS2013, PoS(DIS 2013)149, ATL-PHYS-PROC-2013-147

References

- [1] P. M. Nadolsky, H.-L. Lai, Q.-H. Cao, J. Huston, J. Pumplin, et al., *Implications of CTEQ global analysis for collider observables*, Phys.Rev. **D78** (2008) 013004, arXiv:0802.0007 [hep-ph].
- [2] Higgs Working Group Collaboration, K. A. Assamagan et al., *The Higgs working group: Summary report 2003*, arXiv:hep-ph/0406152.
- [3] S. J. Brodsky, B. Kopeliovich, I. Schmidt, and J. Soffer, *Diffractive Higgs production from intrinsic heavy flavors in the proton*, Phys. Rev. **D73** (2006) 113005, arXiv:hep-ph/0603238.
- [4] J. Pumplin, *Light-cone models for intrinsic charm and bottom*, Phys.Rev. **D73** (2006) 114015, arXiv:hep-ph/0508184 [hep-ph].
- [5] B. Z. Kopeliovich, I. K. Potashnikova, and I. Schmidt, *Penetrating intrinsic charm: evidence in data*, arXiv:1003.3673 [hep-ph].
- [6] R. Brun and F. Rademakers, *ROOT: An object oriented data analysis framework*, Nucl.Instrum.Meth. **A389** (1997) 81–86.
- [7] <http://root.cern.ch/>.
- [8] D. H. Perkins, *Introduction to high-energy physics; 4th ed.* Cambridge Univ. Press, Cambridge, 2000.
- [9] Particle Data Group Collaboration, K. Olive et al., *Review of Particle Physics*, Chin.Phys. **C38** (2014) 090001.
- [10] ATLAS Collaboration, G. Aad et al., *Observation of a new particle in the search for the Standard Model Higgs boson with the ATLAS detector at the LHC*, Phys.Lett. **B716** (2012) 1–29, arXiv:1207.7214 [hep-ex].
- [11] J. M. Campbell, J. Huston, and W. Stirling, *Hard Interactions of Quarks and Gluons: A Primer for LHC Physics*, Rept.Prog.Phys. **70** (2007) 89, arXiv:hep-ph/0611148 [hep-ph].
- [12] <http://www.hep.ucl.ac.uk/pdf4lhc/>.
- [13] M. Botje et al., *The PDF4LHC Working Group Interim Recommendations*, arXiv:1101.0538 [hep-ph].
- [14] L. Carminati, G. Costa, D. D’Enterria, I. Koletsou, G. Marchiori, et al., *Sensitivity of the LHC isolated-gamma+jet data to the parton distribution functions of the proton*, EPL **101** (2013) 61002, arXiv:1212.5511.
- [15] CDF Collaboration Collaboration, T. Aaltonen et al., *A Study of the associated production of photons and b-quark jets in p p-bar collisions at $s^{*(1/2)} = 1.96\text{-TeV}$* , Phys.Rev. **D81** (2010) 052006, arXiv:0912.3453 [hep-ex].
- [16] D0 Collaboration Collaboration, V. Abazov et al., *Measurement of gamma + b + X and gamma + c + X production cross sections in p anti-p collisions at $s^{*(1/2)} = 1.96\text{-TeV}$* , Phys.Rev.Lett. **102** (2009) 192002, arXiv:0901.0739 [hep-ex].
- [17] ATLAS Collaboration Collaboration, G. Aad et al., *Measurement of the inclusive isolated prompt photons cross section in pp collisions at $\sqrt{s} = 7\text{ TeV}$ with the ATLAS detector using 4.6 fb^{-1}* , Phys.Rev. **D89** (2014) no. 5, 052004, arXiv:1311.1440 [hep-ex].

- [18] ATLAS Collaboration Collaboration, *Measurement of the b-jet production cross section using muons in jets with ATLAS in pp Collisions at $\sqrt{s} = 7$ TeV*, .
- [19] ATLAS Collaboration, G. Aad et al., *Measurement of the inclusive and dijet cross-sections of b^- jets in pp collisions at $\sqrt{s} = 7$ TeV with the ATLAS detector*, Eur.Phys.J. **C71** (2011) 1846, arXiv:1109.6833 [hep-ex].
- [20] ATLAS Collaboration, G. Aad et al., *Dynamics of isolated-photon plus jet production in pp collisions at $\sqrt{s} = 7$ TeV with the ATLAS detector*, Nucl.Phys. **B875** (2013) 483–535, arXiv:1307.6795 [hep-ex].
- [21] M. Svatos, *Processes with direct photon and heavy quarks; Workshop of Experimental Nuclear and Particle Physics 2014; Edited by T. Jakoubek, V. Pacik, Sedlackova and M. Vlasak*; http://wejcf2014.ejcf.cz/wejcf2014_proceedings.pdf; ISBN 978-80-01-05657-8, .
- [22] <http://cdsweb.cern.ch/record/842399/files/lhc-pho-1997-169.jpg>, [2012-01-24].
- [23] <https://mediastream.cern.ch/MediaArchive/Photo/Public/2006/0609031/0609031/0609031-A4-at-144-dpi.jpg>, [2012-01-24].
- [24] J. Mnich, *Status of the LHC*, Nucl.Phys.Proc.Suppl. **205-206** (2010) 2–9.
- [25] E. Bruning, Oliver S., E. Collier, P., E. Lebrun, P., E. Myers, S., E. Ostojic, R., et al., *LHC Design Report. 1. The LHC Main Ring*, .
- [26] ATLAS Collaboration Collaboration, G. Aad et al., *The ATLAS Experiment at the CERN Large Hadron Collider*, JINST **3** (2008) S08003.
- [27] <https://twiki.cern.ch/twiki/bin/viewauth/AtlasProtected/CrackDefinition>, [2015-01-04].
- [28] ATLAS Collaboration, J. Schovancova et al., *ATLAS Distributed Computing Monitoring tools during the LHC Run I*, J.Phys.Conf.Ser. **513** (2014) 032084.
- [29] ATLAS Collaboration, S. Campana, *Evolution of the ATLAS distributed computing system during the LHC long shutdown*, J.Phys.Conf.Ser. **513** (2014) 032016.
- [30] A. Collaboration, *Expected photon performance in the ATLAS experiment*, Tech. Rep. ATL-PHYS-PUB-2011-007, CERN, Geneva, Apr, 2011.
- [31] ATLAS Collaboration Collaboration, G. Aad et al., *Electron and photon energy calibration with the ATLAS detector using LHC Run 1 data*, Eur.Phys.J. **C74** (2014) no. 10, 3071, arXiv:1407.5063 [hep-ex].
- [32] <https://twiki.cern.ch/twiki/bin/view/AtlasProtected/EnergyRescaler>, [2015-01-28].
- [33] <https://twiki.cern.ch/twiki/bin/viewauth/AtlasProtected/PhotonFudgeFactors>, [2015-01-28].
- [34] S. Laplace and J. de Vivie, *Calorimeter isolation and pile-up*, Tech. Rep. ATL-COM-PHYS-2012-467, CERN, Geneva, May, 2012.

- [35] M. Cacciari, G. P. Salam, and G. Soyez, *The Anti- $k(t)$ jet clustering algorithm*, JHEP **0804** (2008) 063, arXiv:0802.1189 [hep-ph].
- [36] ATLAS Collaboration Collaboration, G. Aad et al., *Jet energy measurement with the ATLAS detector in proton-proton collisions at $\sqrt{s} = 7$ TeV*, Eur.Phys.J. **C73** (2013) no. 3, 2304, arXiv:1112.6426 [hep-ex].
- [37] ATLAS Collaboration Collaboration, *Selection of jets produced in proton-proton collisions with the ATLAS detector using 2011 data*, Tech. Rep. ATLAS-CONF-2012-020, CERN, Geneva, Mar, 2012.
- [38] T. A. Collaboration, *Expected Performance of the ATLAS Experiment - Detector, Trigger and Physics*, CERN-OPEN-2008-020 (2008) .
- [39] <http://alxr.usatlas.bnl.gov/lxr-stb3/source/atlas/Tracking/TrkEvent/TrkParameters/doc/images/Perigee.png?raw=1>, [2009-11-10].
- [40] ATLAS Collaboration, L. Vacavant, *b-tagging algorithms and performance in ATLAS*, . ATL-PHYS-PROC-2009-023.
- [41] *Calibration of the performance of b-tagging for c and light-flavour jets in the 2012 ATLAS data*, Tech. Rep. ATLAS-CONF-2014-046, CERN, Geneva, Jul, 2014.
- [42] ATLAS Collaboration Collaboration, *Measurement of the b-tag Efficiency in a Sample of Jets Containing Muons with 5 fb-1 of Data from the ATLAS Detector*, Tech. Rep. ATLAS-CONF-2012-043, CERN, Geneva, Mar, 2012.
- [43] <https://twiki.cern.ch/twiki/bin/view/AtlasPublic/LuminosityPublicResults>, [2014-01-13].
- [44] T. Sjostrand, S. Mrenna, and P. Z. Skands, *A Brief Introduction to PYTHIA 8.1*, Comput.Phys.Commun. **178** (2008) 852–867, arXiv:0710.3820 [hep-ph].
- [45] T. Sjostrand, S. Mrenna, and P. Z. Skands, *PYTHIA 6.4 Physics and Manual*, JHEP **05** (2006) 026, arXiv:hep-ph/0603175.
- [46] ATLAS Collaboration Collaboration, G. Aad et al., *The ATLAS Simulation Infrastructure*, Eur.Phys.J. **C70** (2010) 823–874, arXiv:1005.4568 [physics.ins-det].
- [47] GEANT4 Collaboration, S. Agostinelli et al., *GEANT4: A Simulation toolkit*, Nucl.Instrum.Meth. **A506** (2003) 250–303.
- [48] J. Allison, K. Amako, J. Apostolakis, H. Araujo, P. Dubois, et al., *Geant4 developments and applications*, IEEE Trans.Nucl.Sci. **53** (2006) 270.
- [49] <http://home.thep.lu.se/~torbjorn/pythia81html/ParticleProperties.html>, [2015-01-04].
- [50] <https://twiki.cern.ch/twiki/bin/viewauth/AtlasProtected/SMDirectPhoton2012Common>, [2014-01-11].
- [51] M. Baak, C. Guyot, M. Hauschild, R. Hawkins, B. Heinemann, A. Höcker, M. Martínez-Pérez, D. Malon, P. Onyisi, and E. Torrence, *Data Quality Status Flags and Good Run Lists for Physics Analysis in ATLAS*, Tech. Rep. ATL-COM-GEN-2009-015, CERN, Geneva, Mar, 2009.

- [52] https://twiki.cern.ch/twiki/bin/viewauth/Atlas/DataPreparationCheckListForPhysicsAnalysis#Rejection_of_bad_corrupted_event, [2015-01-23].
- [53] <https://twiki.cern.ch/twiki/bin/view/AtlasProtected/LArCleaningAndObjectQuality>, [2015-01-23].
- [54] <https://twiki.cern.ch/twiki/bin/view/Atlas/TileTripReader>, [2015-01-23].
- [55] <https://twiki.cern.ch/twiki/bin/view/AtlasProtected/HowToCleanJets2012>, [2015-01-25].
- [56] https://twiki.cern.ch/twiki/bin/viewauth/AtlasProtected/Egamma2012Analyses#Photon_Trigger, [2015-02-02].
- [57] <https://twiki.cern.ch/twiki/bin/viewauth/AtlasProtected/EgammaTriggerMatching>, [2015-02-02].
- [58] <https://twiki.cern.ch/twiki/bin/view/Sandbox/ReadingPrescales>, [2015-02-02].
- [59] <https://twiki.cern.ch/twiki/bin/viewauth/AtlasProtected/LArCleaningAndObjectQuality>, [2014-01-11].
- [60] https://twiki.cern.ch/twiki/bin/viewauth/AtlasProtected/BTagCalib2014#Latest_and_greatest_2nd_Septembe, [2015-02-04].
- [61] https://twiki.cern.ch/twiki/bin/viewauth/Atlas/DataPreparationCheckListForPhysicsAnalysis#Duplicate_events, [2015-01-23].
- [62] T. A. collaboration, *Pile-up subtraction and suppression for jets in ATLAS*, .
- [63] <https://twiki.cern.ch/twiki/bin/view/AtlasProtected/PATUserAnalysisTools#PileupRewighting>, [2015-02-26].
- [64] J. Chapman, W. Ehrenfeld, J. G. Navarro, C. Gwenlan, S. Mehlhase, et al., *Challenges of the ATLAS Monte Carlo production during Run 1 and beyond*, J.Phys.Conf.Ser. **513** (2014) 032029.
- [65] ATLAS Collaboration Collaboration, G. Aad et al., *Measurement of the inclusive isolated prompt photon cross section in pp collisions at $\sqrt{s} = 7$ TeV with the ATLAS detector*, Phys.Rev. **D83** (2011) 052005, arXiv:1012.4389 [hep-ex].
- [66] M. Hance, *Measurement of Inclusive Isolated Prompt Photon Production in Proton-Proton Collisions at $\sqrt{s} = 7$ TeV with the ATLAS Detector*, .
- [67] <https://twiki.cern.ch/twiki/bin/view/AtlasProtected/BTaggingCalibrationDataInterface>, [2015-02-05].
- [68] <https://root.cern.ch/root/html/TFractionFitter.html>, [2015-03-11].
- [69] https://twiki.cern.ch/twiki/bin/viewauth/AtlasProtected/StandardModelD3PDProd#Can_I_use_NTUP_COMMON, [2015-01-04].